Design and Development of Multifunctional Electrochromic Devices

Ph.D. Thesis

by

Bhumika Sahu

DEPARTMENT OF PHYSICS

INDIAN INSTITUTE OF TECHNOLOGY INDORE

January 2026

Design and Development of Multifunctional Electrochromic Devices

A THESIS

Submitted in partial fulfillment of the
requirements for the award of the degree
of
DOCTOR OF PHILOSOPHY

by

Bhumika Sahu

DEPARTMENT OF PHYSICS
INDIAN INSTITUTE OF TECHNOLOGY INDORE
January 2026

Indian Institute of Technology Indore

CANDIDATE'S DECLARATION

I hereby certify that the work which is being presented in the thesis entitled **"Design and Development of Multifunctional Electrochromic Devices"** in the partial fulfillment of the requirements for the award of the degree of **Doctor of Philosophy** and submitted in the **Department of Physics, Indian Institute of Technology Indore**, is an authentic record of my own work carried out during the time period from July 2022 to January 2026 under the supervision of Prof. Rajesh Kumar, Professor, Indian Institute of Technology Indore.

The matter presented in this thesis has not been submitted by me for the award of any other degree of this or any other institute.

Bhumika 02/01/2026

Signature of the student with date
(Bhumika Sahu)

This is to certify that the above statement made by the candidate is correct to the best of my/our knowledge.

Signature of Thesis Supervisor with date

(Prof. Rajesh Kumar)

Bhumika Sahu has successfully given her Ph.D. Oral Examination held on.....10 April 2026

Signature(s) of Thesis Supervisor(s)

Date:10/04/2026

Dedicated to my parents and teachers…

ACKNOWLEDGEMENTS

Pursuing this Ph.D. has been much like studying electrochromism itself- a journey of switching states, experiencing colors of every intensity, and discovering how transformation under the right stimulus can lead to something meaningful. There were moments when I felt fully "colored"- energized with passion and confidence, and there were times when I slowly "bleached," losing clarity under pressure. Yet, just like a reversible electrochromic process, every setback recharged me with new learning and renewed motivation. This journey would not have been possible without the constant "electrolytes" in my life—the people whose support acted as the medium that kept me connected and balanced.

Firstly, I express my sincere gratitude to God for His boundless grace and blessings. It is solely through His divine favor that I have reached this stage of my life and successfully completed this thesis. I express my sincere gratitude to my supervisor Prof. Rajesh Kumar, whose guidance acted as the voltage required to initiate every change, pushing me to evolve, challenge myself, and remain focused on the larger picture. His ideologies have been a constant source of inspiration, helping me push through my limitations and achieve this feat. Without his constant support and inspiration, this goal would not have been possible to achieve. Additionally, this endeavor wouldn't have been possible without the valuable feedback I received from my PSPC members, Professor Sanjay K. Singh (IIT Indore), and Professor Naresh Kumawat (IIT Indore) who patiently refined my work year and again.

Besides, I am highly thankful Professor Suhas Joshi, Director IIT Indore. All the faculty members of Department of Physics (IITI) for continuous discussions and their valuable insights about my work. I express my

heartfelt gratitude to Dr. Hem C. Jha for his invaluable support in numerous ways. I also extend my gratitude to all my collaborators for providing me with an opportunity to work with them. I would like to thank our interdisciplinary collaborators Dr. Prakash Mondal (Chemistry, IIT Kanpur), Dr. Arvind Yogi (UGC Consortium, Indore), Dr. Sandeep Chhokker (JIIT), Dr. Sameera (Guru Jambheshwar University, Hisar), Prof. Abhinav Raghuvanshi (Chemistry, IIT Indore), Dr. Maxim Yu. Maximov (Peter the Great Saint Petersburg Polytechnic University, Russia) for their fruitful discussion and working together.

I would like to extend my heartfelt gratitude to the academic staff, especially Tapesh Parihar, Rahul Shrivas, Suresh Thakur, and Neeraj Pandey. I would also like to acknowledge Raman facilities by DST-FIST at IIT Indore. The technical staff of Physics Department, IIT Indore, Mr. Rahul, Mr. Prashant, Dr. Nitin and Mr. Ved Prakash are thanked for their contributions and all staff members of IIT Indore. I am very grateful to all the hospitality staff, sports staff, Dr. Shilpa Raut, and medical staff of IIT Indore for providing me with all essentials during need. A special thanks to the badminton club for keeping me physically active, motivated, and energized throughout this journey.

I extend heartfelt thanks to my research group, colleagues, and lab mates, who shaped my academic environment with laughter and genuine support. I wish to say a big thank you to my seniors, including Dr. Suchita Kandpal, Dr. Chanchal Rani, Dr. Love Bansal, Dr. Subin K. Chondath. I would like to express my special thanks to Dr. Tanushree Ghosh for her valuable guidance and support during the initial phase of my Ph.D. journey. I feel truly fortunate to have spent time with my lab mates Deb Kumar Rath, Nikita Ahlawat, Partha Sarathi Rout, Shivam Kumar, Saumya Srivastava, Sharmistha, MD Sahid, Shivansh Pandey,

Divyansh Mishra, Jatin Boyat, Arpita, Bharat for their support, help, and contribution to the fantastic research environment. I would like to extend my thanks to my friends Ayushi Di, Amarendra, Satya, Garvit, Ramavatar, Banadeep, Dilip, Rakhi, Manju, Harish, Sushmita and all my Ph.D. 2022 batchmates outside of the lab for their support. A very special thanks to Abhishek S. Shekhawat for always staying by my side and believing in me, even during the most challenging times.

Finally, and with all my heart, I would like to thank my mother, Mrs. Veena Sahu, for her immeasurable sacrifices and unconditional love that have shaped me into who I am today. I am deeply grateful to my father, Mr. Parmanand, whose wisdom, guidance, and unwavering support made this journey possible. I also extend my heartfelt thanks to my sisters, Ms. Nidhee Sahu and Ms. Surabhi Sahu, for their constant belief in me, encouragement, and the endless love they have always given me. I end here by thanking every person who directly or indirectly contributed to my research. If this thesis reflects any clarity, impact, or beauty, it is because of all of you who contributed to my journey of growth and transformation.

Just as an electrochromic device becomes functional only when every layer works in harmony, this Ph.D. is not just my accomplishment, but a collective achievement colored by your presence and support.

Bhumika Sahu

Abstract

In the era of smart and adaptive technologies, materials that can sense and respond to their environment are reshaping modern electronics. Among them, electrochromism stands out as a key concept for flexible smart windows, energy-efficient systems, and multifunctional devices. Electrochromic materials can dynamically modulate color and transparency under an applied bias while storing energy, bridging the gap between materials and intelligent electronics. Covering inorganic, organic, and hybrid systems, they exhibit tunable band gaps that lead to visible color changes. Typically, electrochromic devices (ECDs) employ a five-layered configuration, with performance evaluated through parameters defining efficiency, stability, and reversibility.

The growing demand for flexible, multifunctional, and energy-efficient smart devices has accelerated research in electrochromic (EC) technologies. This thesis focuses on the design, synthesis, and development of advanced electrochromic and electrochromic-supercapacitor (ESCD) devices by integrating all-organic and organic-inorganic hybrid materials to achieve superior optical modulation, rapid switching, and enhanced mechanical stability.

This thesis presents the development of flexible electrochromic devices (ECDs) by combining the fast electrochromic response of organic polymers with the stability of metal oxides. Hybrid structures based on P3HT-EV and oxide nanomaterials enabled devices with rapid switching, high color contrast, and excellent mechanical flexibility. To expand their functionality for wearable and heat-shielding applications, a flexible NIR-cutting ECD was further engineered using a WS_2/WO_3-doped polymer system. The device showed efficient optical modulation

and notable NIR-blocking ability, demonstrating strong potential for next-generation smart windows and heat-filtering smart eyewear.

Besides their use in smart windows and displays, electrochromic devices (ECDs) also offer multifunctional applications in energy storage systems such as supercapacitors and batteries, as well as in heat and NIR shielding technologies. Their tunable optical response, flexibility, and compatibility with advanced nanomaterials make them ideal for next-generation adaptive and energy-efficient devices. Therefore, in this work, multifunctional electrochromic-energy-storage systems were developed by integrating organic polymers with engineered nanomaterials. An all-organic solid-state electrochromic supercapacitor was fabricated using MXene-viologen and P3HT electrodes, delivering strong optical modulation, fast switching, and efficient pseudocapacitive behavior for integrated energy-optical applications. Additionally, an organic–inorganic asymmetric electrochromic supercapacitor based on $CoTiO_3$-P3HT and WO_3 electrodes was developed, showing stable coloration, robust electrochemical performance, and effective NIR attenuation for thermally adaptive systems. Overall, this thesis demonstrates nanomaterial-engineered strategies for creating flexible, durable, and multifunctional electrochromic platforms suitable for smart displays, wearable electronics, and advanced thermal-management applications.

LIST OF PUBLICATIONS

a) Peer reviewed journals (Thesis):

1. **Sahu, B.**; Bansal, L.; Rath, D. K.; Kandpal, S.; Ghosh, T.; Ahlawat, N.; Rani, C.; Maximov, M. Y.; Kumar, R. Bendable & Twistable Oxide-Polymer Based Hybrid Electrochromic Device: Flexible and Multi-Wavelength Color Modulation. *Mater. Today Electron.* **2024**, *7*, 100082.
2. **Sahu, B.**; Bansal, L.; Ahlawat, N.; Ghanghass, A.; Rath, D. K.; Kaladi Chondath, S.; Kandpal, S.; Bhatia, R.; Sameera, I.; Kumar, R. Mixed Chalcogenides Nanoflakes' Infrared Cutting Effect: Utilization in Thermal Soothing Electrochromic Goggles. *ACS Appl. Opt. Mater.* **2024**, 2, 10, 2128–2136.
3. **Sahu, B.**; Singh, M. K.; Bansal, L.; Rath, D. K.; Rai, D. K.; Kumar, R. $Ti_3C_2T_x$-MXene-Based Color-Indicative All-Organic Electrochromic Supercapacitors. *Adv. Eng. Mater.* **2024**, *26* (23), 2401295.
4. **Sahu, B.**; Bansal, L.; Ghosh, T.; Kandpal, S.; Rath, D. K.; Rani, C.; Wesemann, C.; Bigall, N. C.; Kumar, R. Metal Oxide-Mixed Polymer-Based Hybrid Electrochromic Supercapacitor: Improved Efficiency and Dual Band Switching. *J. Phys. D. Appl. Phys.* **2024**, *57* (24), 245110.
5. **Sahu, B.**; Bansal, L.; Ahlawat, N.; Rath, D. K.; Shekhawat, A. S.; Chondath, S. K.; Saxena, S. K.; Kumar, R. Developing a solid state electrochromic-supercapacitor prototype through DFT-guided charge transfer engineering in 2D carbon doped NiO. J. Mater. Chem. C, **2026**, 14, 5284 - 5297.

b) Peer reviewed journals (Outside thesis):

1. **Sahu, B.**; Ghosh, T.; Kandpal, S.; Bansal, L.; Rani, C.; Jha, H. C.; Kumar, R. Green and Red Luminescent Curcuma and Lawsone Herbal Amalgam as Yellow Emission Source. *ChemistrySelect* **2023**, *8* (14), e202204265.
2. **Sahu, B.**; Kharabe, L. S.; Mishra, S.; Kumar, R.; Raghuvanshi, A. Redox Dependent Color Modulating Copper (I) Complex for Flexible Electrochromic Device. *ChemPhotoChem* **2025**, *9* (4), e202400354.

c) Peer reviewed journals (contributory work):

1. Bansal, L.; **Sahu, B.**; Rath, D. K.; Ahlawat, N.; Ghosh, T.; Kandpal, S.; Kumar, R. Stoichiometrically Optimized Electrochromic Complex [$V_2O_{2+\xi}$ $(OH)_{3-\xi}$] Based Electrode: Prototype Supercapacitor with Multicolor Indicator. *Small* **2024**, *20* (32), 2312215.
2. Ahmed, M. S.; **Sahu, B.**; Bansal, L.; Ahlawat, N.; Rath, D. K.; Pandey, S. R.; Chondath, S. K.; Kumawat, N. K.; Kumar, R. Device Parameter Optimization of All-Organic Electrochromic Smart Windows: Role of Performance Enhancer Metal-Oxides. *Sol. Energy Mater. Sol. Cells* **2025**, *288*, 113626.
3. Srivastava, S.; **Sahu, B.**; Mishra, D.; Bansal, L.; Ahlawat, N.; Rath, D. K.; Rout, P. S.; Kumar, S.; Singh, S.; Pandey, P.; others. Polymer--MXene--Viologen-Based Suprahybrid Electrochromic Device: Flexible Smart Window with Visible and Near-Infrared Switchability. *ACS Appl. Opt. Mater.* **2025**, *3* (4), 889–897.
4. Ahlawat, N.; **Sahu, B.**; Bansal, L.; Rath, D. K.; Chondath, S. K.; Kumar, R. Performance Specific Recipe for Nano-Co3O4 Based Electrochromic Electrodes: Optimizing Color Modulation

Parameters. *Optik.* **2025**, *321*, 172174.

5. Bansal, L.; Ahlawat, N.; **Sahu, B.**; Rath, D. K.; Chondath, S. K.; Ghosh, T.; Kumar, R. Nano-Nest Type Porous $NiCo_2S_4$@polyindole Core-Shell Array: Efficient Energy Storage Supercapacitor Device. *ACS Mater. Lett.* **2024**, *6*, 3736–3744.

6. Shekhawat, A. S.; **Sahu, B.**; Diwan, A.; Chaudhary, A.; Shrivastav, A. M.; Srivastava, T.; Kumar, R.; Saxena, S. K. Insight of Employing Molecular Junctions for Sensor Applications. ACS sensors 2024, 9 (10), 5025–5051.

7. Bansal, L.; Lübkemann-Warwas, F.; **Sahu, B.**; Ghosh, T.; Kandpal, S.; Rani, C.; Rath, D. K.; Prawitt, L.; Wesemann, C.; Bigall, N. C.; others. Nano Aerogel-Based VIS-NIR Switchable Electrochromic Supercapacitor: Energy Storage and Heat-Shielding Device. ACS Appl. Mater. & Interfaces 2025, 17 (21), 31201–31211.

Table of contents

Acknowledgements ..... **i**

Abstract ..... **v**

List of publications ..... **vii**

List of tables ..... **xix**

List of figures ..... **xx**

List of abbreviations ..... **xxix**

1. Introduction **1-16**

1.1 Background of Electrochromism: The Flexible & Multifunctional Electronics 1

1.2 Electrochromism – The Art of Reversible Color Change 2

1.3 Redox-Active Materials: Electrochromic Active Materials 3

1.3.1 Nanomaterials 6

1.3.2 Synthesis Methods 7

1.4 Generic Structure of ECDs. 7

1.5 The Multifunctional ECDs and Its Applications 8

1.6 Electrochromic Supercapacitor Device Performance Metrics 11

1.6.1 Coloration Efficiency 11

1.6.2 Switching/Response Time 12

1.6.3 Switching/Response Time 12

1.6.4 Cyclic Life 12

1.6.5 Specific Capacitance 13

1.6.6 Columbic efficiency 13

1.6.7 Capacitive Retention 13

1.6.8 Ragone Plot 14

1.7 Main Objective of the Work 14

1.8 Organization of Thesis 15

2. Experimental Techniques 17-42

2.1 Sample Preparation Techniques 18

2.1.1 Sol-Gel Method 18

2.1.2 Co-Precipitation 18

2.1.3 Hydrothermal 19

2.1.4 Electrodeposition 20

2.1.5 Selective Etching Method. 21

2.1.6 Hummer's Method 21

2.1.7 Spin-Coating 22

2.1.8 Drop Casting 23

2.2 Synthesis of Materials 24

2.2.1 Cobalt Oxide (Co_3O_4) 24

2.2.2 Tungsten Oxide (WO_3) 24

2.2.3 Tungsten Oxide/ Tungsten Sulfide (WO_3/WS_2) Mixture 24

2.2.4 MXene Titanium Carbide ($Ti_3C_2T_x$) 25

2.2.5 Cobalt Titanate ($CoTiO_3$) 25

2.2.6 Graphene (Gr) and Graphene Oxide (GO) 26

2.3 Electrode Preparation 26

2.3.1 Poly (3-Hexylthiophene), P3HT Electrode (Flexible/ Solid State) 27

2.3.2 The Co_3O_4 – Doped P3HT Electrode 27

2.3.3 The WO_3 – Doped Ethyl Viologen (EV) Electrode 27

2.3.4 The WS_2/WO_3-Doped EV Electrode 27

2.3.5 MXene $Ti_3C_2T_x$ -Doped EV Electrode 28

2.3.6 Perovskite $CoTiO_3$-Doped P3HT Electrode 28

2.3.7 The WO_3 Electrode 28

2.3.8 The NiO Electrode 29

2.3.9 The Gr/GO-Doped NiO Electrode 30

2.4 Characterization Techniques 30

2.4.1 Scanning Electron Microscopy 31

2.4.2 Transmission Electron Microscopy 32

2.4.3 X-ray Diffraction 32

2.4.4 Raman Spectroscopy 33

2.4.5 UV-Vis Spectroscopy 34

2.4.6 X-ray Photoelectron Spectroscopy 35

2.4.7 Electrochemical Measurement. 36

2.4.7.1 Cyclic Voltammetry 36

2.4.7.2 Galvanostatic Charging Discharging 37

2.4.7.3 Electrochemical Impedance Spectroscopy 37

2.4.7.4 Chronoamperometry 38

2.4.7.5 Chronopotentiometry 38

2.4.7.6 In-situ Absorbance Spectroscopy 38

2.5 Methodologies for Device Fabrication 38

2.5.1 ECD Assembly Using Flip-Chip Method 39

2.5.1.1 Flexible ECD (Flex-ECD) 39

2.5.1.2 Flexible NIR-cutting ECD (flex-NIR cutting-ECD) 39

2.5.1.3 MXene Doped Electrochromic Supercapacitor Device (M-Doped ESD) 40

2.1.5.4 Perovskite CoTiO3-Doped Electrochromic Supercapacitor Device (ESCD) 40

2.5.2 Supercapacitor Device (SCD) Assembly 40

2.6 About Software: Osram Sylvania 41

2.7 Computational Details 41

3. Highly Flexible Asymmetric All-Organic Multifunctional ECDs **43-80**

3.1 Complementary nature of P3HT and Viologen 44

3.2 Highly Bendable and twistable property of metal oxide doped all-organic ECDs 45

3.2.1 Structural Characterization of Metal Oxides 46

3.2.2 Flexible ECD Fabrication. 48

3.2.3 Optical Measurement of the Initial Flex-ECD. 50

3.2.4 Optical Measurement of the b-Flex-ECD After 20 Bending. 54

3.2.5 Optical Measurement of the tb-Flex-ECD After 20 Twisting. 58

3.3 Flexible NIR-Cutting Electrochromic Goggles Using Metal Chalcogenides Oxide Mixture. 64

3.3.1 Structural Characterization of WS2/WO3 Nanoflakes. 65

3.3.2 Flexible NIR-Cutting ECD Fabrication. 67

3.3.3 Flex-NIR Cutting ECD As Smart Eye-Soothing Goggle Prototype 68

3.3.4 Optical Study of the Flex-NIR Cutting ECD in NIR Region. 69

3.3.5 Practical Evaluation of NIR-Cutting Performance of Flex-NIR-Cutting ECD. 73

3.3.6 Optical Study of the Flex-NIR Cutting ECD in the Visible Region. 75

3.4 Summary and Conclusion 79

4. MXene-based Asymmetric All-Organic Multifunctional Electrochromic Supercapacitor. **81-101**

4.1 Multifunctional All-Organic Electrochromic Supercapacitor Doped with 2D MXene 82

4.2 Structural Characterization Of 2-D MXene $Ti_3C_2T_x$ 82

4.3 Structural Characterization of EC Active Electrode 84

4.3.1 MXene Doped Ethyl Viologen (EV) Electrode 84

4.3.2 The Poly (3-Hexyl thiophene-2,5 diyl) (P3HT) Electrode 85

4.4 Electrochemical Measurement of MXene and Electrodes. 85

4.5 Optical Study of MXene Doped EV Electrode. 89

4.6 The Fabrication of MXene-Doped EC Supercapacitor Device. 91

4.7 Optical Study of the M-doped ESD. 92

4.8 Charge Storage Study of the M-doped ESD 97

4.9 Summary and Conclusion 100

5. Perovskite-based Asymmetric Organic-Inorganic Electrochromic Supercapacitor Device. **103-129**

5.1 Nano-$CoTiO_3$/P3HT and WO_3-Based ESCDs 104

5.2 Structural Characterization of $CoTiO_3$ Perovskite. 104

5.3 Electrochemical Measurement of the Electrodes. 108

5.4 Electrochemical Measurement of CTO-P3HT Electrode 110

5.5 Electrochemical Measurement of WO_3 Electrode 113

5.6 Optical Study of the CTO-P3HT Electrodes 116

5.7 The Fabrication of Asymmetric EC Supercapacitor Device (ESCD) by Doping $CoTiO_3$ 118

5.8 Optical Study of the Fabricated EC Supercapacitor Device (ESCD) 119

5.9 Charge Storage Property of the ESCD. 123

5.10 Summary and Conclusion 129

6. Carbon Materials Based Asymmetric Electrochromic Supercapacitor Devices **131-154**

6.1 The Family of Carbon: Graphene (Gr) and Graphene Oxide (GO) 132

6.2 Theoretical Optimization of Gr and GO 132

6.3 Structural Characterization of Gr and GO Nanoflakes. 134

6.4 Electrochemical Measurement of the Electrodes 138

6.5 Theoretical Study of Gr-NiO and GO-NiO Interaction 143

6.6 The Fabrication of Asymmetric Supercapacitor Device. 144

6.7 Charge Storage Property of the GO-NiO-SCD and Gr-NiO-SCD 145

6.8 Optical Study of the Gr-NiO and GO-NiO Electrodes. 150

6.9 Summary and Conclusion 154

7. Conclusions and Future scope **155-160**

7.1 Conclusion & Summary 155

7.1.1 Highly Flexible Asymmetric All-Organic ECDs 155

7.1.2 MXene-Based Asymmetric All-Organic Multifunctional Electrochromic Supercapacitor 156

7.1.3 Perovskite-based Asymmetric Organic-Inorganic Electrochromic Supercapacitor Device 157

7.1.4 Carbon Materials Based Asymmetric Electrochromic Supercapacitor Devices 158

7.2 New Findings Reported in the Thesis 159

7.3 Future Scope of the Work. 159

Appendix **161**

References **162-177**

Annexures **178**

LIST OF TABLES

Table No. Description	Page No.
Table 1.1 Various EC active materials.	4
Table 3.1 Comparison of different flexible devices on basis of different performance parameters.	62
Table 3.2 Comparison table between the flex-ECD, b-flex-ECD and tb-flex-ECD on basis of their performances	63
Table 3.3 Comparison of performance parameters for the flex-NIR cutting-ECD.	78
Table 4.1 Collective solution and charge transfer resistance of MXene on carbon cloth, EV and MXene-doped EV electrodes	89
Table 4.2 Comparison table for comparing the electrochromic performance of the M-doped ESD.	96
Table 4.3 Comparison table for comparing the energy storage application of the M-doped ESD.	99
Table 5.1 Comparison of various already reported electrochromic supercapacitor device	127
Table 6.1 Collective values of solution resistance (Rs) and charge transfer resistance (Rct) for all three electrodes.	142
Table 6.2 Comparison table of NiO based supercapacitor devices	148

LIST OF FIGURES

Figure No. Captions	Page No.
Figure 1.1: Schematic illustration of types of nanomaterials.	7
Figure 1.2: Generic structure of an electrochromic device	8
Figure 1.3: Schematic showing various applications of ECDs.	9
Figure 1.4: EDLC (non-faradic) and pseudocapacitive (Faradic) charge storage mechanisms.	10
Figure 2.1: Co-precipitation synthesis method step by step.	19
Figure 2.2: Schematic illustration of a hydrothermal setup	20
Figure 2.3: Schematic of electrodeposition setup with three electrodes.	21
Figure 2.4: The schematic illustration of spin-coating technique.	23
Figure 2.5: The schematic representation of drop casting method.	23
Figure 2.6: Schematic representation of WO3 electrode preparation.	29
Figure 2.7: Generic synthesis route for the fabrication of NiO.	29
Figure 2.8: Schematic illustration of major components of scanning electron microscopy.	31
Figure 2.9: Schematic illustration of major components of X-ray diffractometer.	33
Figure 2.10: Schematic illustration of major components of Raman spectrometer.	34

Figure 2.11: Schematic of an UV-Vis spectrometer 35

Figure 2.12: The schematic of the electrochemical workstation having three electrodes. 36

Figure 2.13: Schematic showing In-situ absorbance spectroscopy. 38

Figure 2.14: Schematic of step-by-step process for the fabrication of device 39

Figure 2.15: Schematic for the fabrication of electrode and device. 40

Figure 2.16: A typical CIE chart wherein various colors has been assigned to certain specific co-ordinates. 41

Scheme 3.1: (a) The P3HT and (b) Ethyl viologen diperchlorate molecules. 44

Figure 3.1: The surface morphology of the metal oxides nanomaterials (a) WO3 and Co3O4 (b) 46

Figure 3.2: The Raman spectrum and XRD plots of the metal oxides nanomaterials (a,c) WO3 and Co3O4 (b,d). 47

Figure 3.3: The schematic of the fabricated flex-ECD with original device color in ON and OFF state. 49

Figure 3.4: Performance of the initially fabricated flex-ECD (a) in-situ bias dependent absorbance, (b) in-situ bias dependent transmittance spectra, (c) Single switching cycle at 515 nm, (d) at 665 nm and (e) the cyclic stability at 515 nm and (f) 665 nm. 51

Figure 3.5: (a,b)The ΔOD vs charge density graph for calculating coloration efficiency at 515 nm and 665 nm of the initially fabricated flex-ECD with corresponding current vs time vs voltage graph for 515nm and 665 nm (c,d). 53

Figure 3.6: (a) The bending angle and bending frequency of the b-flex-ECD under ambient condition and (b) Photograph showing the bending of the device along with in-situ bias dependent transmittance spectra (inset) of the b-flex-ECD after bending 20 times. 55

Figure 3.7: (a,b) Single switching cycle at 515 nm and 665 nm and the cyclic stability at 515 nm and 665 nm of the b-flex-ECD (c,d). 56

Figure 3.8: (a,b) The ΔOD vs charge density graph for calculating coloration efficiency at 515 nm and 665 nm of the b-flex-ECD with corresponding current vs time vs voltage graph for 515nm and 665 nm (c,d). 57

Figure 3.9: (a) The twisting angle and twisting frequency of the tb-flex-ECD under ambient condition and (b) Photograph showing the bending of the device along with in-situ bias dependent transmittance spectra (inset) of the tb-flex-ECD after twisting 20 times. 59

Figure 3.10: (a,b) Single switching cycle at 515 nm and 665 nm and the cyclic stability at 515 nm and 665 nm of the tb-flex-ECD (c,d). 60

Figure 3.11: (a,b) The ΔOD vs charge density graph for calculating coloration efficiency at 515 nm and 665 nm of the b-flex-ECD with corresponding current vs time vs voltage graph for 515nm and 665 nm (c,d). 61

Figure 3.12: (a) The FESEM image and (b) the XRD plot of the WS2/WO3 nanoflakes mixture 65

Figure 3.13: (a) XRD pattern and FESEM micrographs of (a) WO3 nanorods (1h), (c) WS2/WO3 nanoflakes (3h) and (d) WS2 nanoflakes (24h). 66

Figure 3.14: Schematic of the flex-NIR cutting-ECD in ON and OFF states. 67

Figure 3.15: Flex-NIR cutting-ECD in goggle form showing two different shades in ON and OFF states 69

Figure 3.16: (a) In-situ transmittance spectra in NIR region for (a) flex-NIR-Cutting ECD and (b) pristine EV-P3HT-based ECD. 70

Figure 3.17: The switching stability of the flex-NIR-Cutting ECD at (a, b) 1100 nm and 800 nm with single switching cycle at (c,d) 1100 nm and 800 nm. 71

Figure 3.18: (a,b) Variation of change in optical density as a function of charge density for coloration and bleaching process (inset) at 1100 nm and 800 nm and (c,d) Current v/s voltage response of the flex-NIR cutting-ECD at 1100 nm and 800 nm respectively. 72

Figure 3.19: Photograph captured using a thermal (IR) camera of a hot plate covered with flex-NIR cutting-ECD in (a,b) OFF and (c,d) ON states. 74

Figure 3.20: (a) In-situ transmittance spectra in visible region for (a) flex-NIR-Cutting ECD and (b) pristine EV-P3HT-based ECD. 75

Figure 3.21: (a) Switching cyclic stability. (b) Single switching cycle. (c) Variation of change in optical density as a function of charge density for coloration and bleaching process (inset). (d) Current v/s voltage response of the flex-NIR cutting-ECD at 515 nm. 77

Figure 3.22: In-situ transmittance spectra of the flex-NIR cutting ECD in bent state with a bending angle of 60° (inset) in initial, ON and OFF states. 77

Figure 4.1: (a) FESEM micrograph along with a magnified portion (inset), (b) Elemental mapping of the synthesized MXene from MAX phase, (c) The Raman spectrum and (b) XRD pattern of MXene. 83

Figure 4.2: (a) The FESEM micrograph and (b) Raman spectra of MXene doped EV electrode. 84

Figure 4.3: (a) The FESEM micrograph and (b) Raman spectra of P3HT electrode. 85

Figure 4.4: (a) The CV curves of MXene on carbon cloths at various scan rate and (b) Nyquist plot of MXene on CC with equivalent electrical circuit. 86

Figure 4.5: (a) Comparative CV curves of alone EV and EV+MXene on GC electrode at 100 mV/s scan rate (b) CV curves of EV+MXene with varying scan rate (c) CV curve of EV on bare GC with varying scan rate (d) Nyquist plot of alone EV and EV+MXene along with equivalent electrical circuit (inset). 87

Figure 4.6: (a) In-situ transmittance spectra, (b) Single switching cycle, (c) Current response with varying voltage pulse of ± 0.7 V, and (d) Coloration Efficiency of the MXene-doped EV in two-electrode setup. 90

Figure 4.7: Schematic of fabricated device and corresponding photograph of actual device in two different states. 91

Figure 4.8: in-situ transmittance spectra of device at 0V and ± 1.4V (inset CIE plot along with actual image of the device) 93

Figure 4.9: (a, b) Single switching cycle of the device at 515nm and 700nm (c, d) coloration efficiency at 515 nm and 700 nm along with stability diagram (inset). 94

Figure 4.10: Applied square pulse of ± 1.4V and corresponding current flowing through the device. 95

Figure 4.11: (a) Scan rate dependent CV curves from the device along with GCD plots (b). 97

Figure 4.12: (a) Specific capacitance vs current density curve, (b) Retention graph of M-doped-ESD with capacitive stability (inset) 98

Figure 4.13: Nyquist plot of device at 1.1V with equivalent circuit (inset) 99

Figure 5.1: (a) The FESEM image, (b) TEM image, (c) The Raman spectrums and (b) the XRD plot of CoTiO3. 105

Figure 5.2: SEM micrograph of WO3 evenly spread all over the ITO substrate along with nano flower (Inset), (b) The Raman spectrum and (b) XRD plot of WO3 film. 106

Figure 5.3: (a) The XRD plot and (b) optical image of CTO-P3HT film. 107

Figure 5.4: The Cyclic Voltammetry curve of CoTiO3 with bare glassy carbon electrode and CoTiO3 drop casted over glassy carbon electrode and (b) Nyquist plot of CoTiO3. 108

Figure 5.5: (a) Cyclic voltammetry at different scan rates (Inset: actual images) and (b) Nyquist plot at 0V of CTO-P3HT electrode 110

Figure 5.6: Logarithmic peak current distribution as a function of logarithmic scan rate for CoTiO3 doped P3HT 112

Figure 5.7: (a) Charging/discharging curves with increasing current densities and (b) corresponding Specific Capacitance vs Current density graph of CTO-P3HT electrode. 112

Figure 5.8: (a) Cyclic voltammetry at different scan rates (Inset: actual images) and (b) Nyquist plot at 0V of the WO3 electrode. 113

Figure 5.9: Logarithmic peak current distribution as a function of logarithmic scan rate for WO3 electrode. 114

Figure 5.10: (a) Charging/discharging curves with increasing current densities and (b) corresponding Specific Capacitance vs Current density graph of WO3 electrode. 115

Figure 5.11: (a) In-situ transmittance spectra of CoTiO3 doped P3HT electrode under an external bias of ± 1.4 V (b) single switching cycle of CoTiO3 doped P3HT electrode and (c) cyclic stability at 515 nm. 117

Figure 5.12: Schematic of the fabricated ESCD 119

Figure 5.13: In-situ biased dependent transmittance spectra of the device at initial, on and off state with actual photographs (a) in visible range (b) in NIR range. 119

Figure 5.14: Single switching cycle of colored and bleached state of the device at (a) 515 nm, (b) 700 nm and (c) 850 nm. 121

Figure 5.15: Coloration Efficiency of ESCD at (a) 515 nm, (b) 700 nm and (c) 850 nm and (d) Current vs time vs potential plot. 122

Figure 5.16: Cycle life of ESCD at (a) 515 nm, (b) 700 nm and (c) 850 nm 123

Figure 5.17: Cyclic voltammetry of the device at different scan rates (20mV/s to 200mV/s). 124

Figure 5.18: Logarithmic peak current distribution as a function of logarithmic scan rate @ 1.4 V (anodic current) (b) 0.8 V (anodic current) and (c) 0.8V (cathodic current), and ip/sqrt (scan rate) as a function of sqrt (scan rate). 125

Figure 5.19: Capacitance percentage distribution as a function of scan rate. 125

Figure 5.20: (a) charging/discharging curve of ESCD and (b) varying specific capacitance value with energy density vs power density graph. 126

Figure 6.1: Optimized molecular geometry (a,b) and corresponding molecular electrostatic potential (MEP) plot (c,d) of graphene (Gr) and graphene oxide (GO). Cross sectional view of MEP is shown in corresponding insets. 133

Figure 6.2: The FESEM micrographs of (a) Gr, (b) GO and Raman spectra of Gr and GO. 134

Figure 6.3: The FESEM micrographs along with Raman spectra in insets (a) NiO electrode, (b) Gr-NiO electrode, (c) GO-NiO electrode, elemental mapping images of NiO electrode (d, e), Gr-NiO electrode (f-h), GO-NiO electrode(i-k). The HRTEM microscopic images of (l) NiO, (m) Gr-NiO, and (n) GO-NiO electrodes. 135

Figure 6.4: (a) XPS survey scan spectrum of NiO, Gr-NiO, GO-NiO electrodes confirming the characteristic elements, High resolution XPS spectra from (b, c) NiO, (d-f) Gr-NiO and (g-i) GO-NiO electrodes. 137

Figure 6.5: (a) Schematic of the electrochemical arrangement, (b) comparative CVs of all the electrodes, scan rate dependent CV curves of (c) NiO, (d) Gr-NiO and (e) GO-NiO electrodes. 139

Figure 6.6:(a) logarithmic plot of the current density v/s scan rate for all the electrodes (b) capacitive contribution plot of GO-NiO electrode, (c) NiO and Gr-NiO (d) 141

Figure 6.7: (a) EIS plot of all the electrodes, (b) comparative GCD plot of all the electrodes, GCD plot of (c) NiO, (d) Gr-NiO, (e) GO-NiO and (f) comparative specific capacitance vs current density plot of all the electrodes. 143

Figure 6.8: Computed ESP plots of (a) Gr- NiO, (b) GO- NiO and NiO (c). 144

Figure 6.9: Schematic representation of asymmetric supercapacitor 145

Figure 6.10: (a) CV curve of GO-NiO-SCD, (b) specific capacitance value of GO-NiO-SCD , (c) scan rate dependent CV curve of GO-NiO-SCD, (d) Comparative CV curve of Gr-NiO-SCD and GO-NiO-SCD, (e) The scan rate dependent CV curve of the Gr-NiO-SCD and (f) Comparative Nyquist plot of Gr-NiO-SCD and GO-NiO-SCD recorded at 0.2V 146

Figure 6.11: (a) GCD plot along with actual photograph of the device in corresponding charged state (inset), (b) Comparative GCD profile of Gr-NiO-SCD and GO-NiO-SCD recorded at 3.5 mA/cm2, (c) Specific capacitance value with varying current density from GO-NiO-SCD and (d) Retention of the GO-NiO-SCD with stability up to 500 cycles (inset). 148

Figure 6.12: (a) The CV curve of the GO-NiO-SCD before and after stability measurements, (b) large area GO-SCD while charging, (c) while discharging through LED, (d) when 50% discharged through LED. 150

Figure 6.13: (a) Photograph of the optical measurement setup used to perform the in-situ bias dependent optical measurements of the electrodes, (b) transmittance spectra of the NiO electrode with varying applied bias, (c) transmittance spectra of Gr-NiO in unbiased, On and Off states and (d) transmittance spectra of GO-NiO in unbiased, On and Off state. 151

Figure 6.14: (a) single switching cycle of the Gr-NiO electrode showing fast switching, the single switching cycle of the (b) NiO and GO-NiO electrodes (c), (d) electrochromic stability of the GO-NiO electrode, The switching stability of the (e) NiO and Gr-NiO electrodes (f). 153

LIST OF ABBREVIATIONS

Abbreviations	Full forms
ACN	Acetonitrile
CC	Color Contrast
CE	Counter Electrode
CIE	Commission Internationale de l'Eclairge
CV	Cyclic Voltammetry
DI water	De-ionized Water
EC	Electrochromic
ECD	Electrochromic Device
EIS	Electrochemical Impedance Spectroscopy
ESCD	Electrochromic supercapacitor device
EV	Ethyl Viologen
FESEM	Field Emission Scanning Electron Microscope
FTO	Fluorine tin Oxide
GCD	Galvanostatic Charge Discharge
GO	Graphene Oxide
Gr	Graphene

ITO	Indium Tin Oxide
IR	Infrared
NIR	Near Infrared
OC	Optical Contrast
PEO	Polyethylene Oxide
PET	Polyethylene Terephthalate
P3HT	Poly(3-hexyl) thiophene
RE	Reference Electrode
SEM	Scanning Electron Microscope
UV	Ultra-violet
WE	Working Electrode
XRD	X-ray Diffraction
$\boldsymbol{\eta_{be}}$	Bleaching Efficiency
$\boldsymbol{\eta_{ce}}$	Coloration Efficiency

Chapter 1

Introduction

Nanoscience and nanotechnology originated from pioneering ideas about controlling matter at the atomic and molecular levels, notably introduced by Richard Feynman in his 1959 lecture *"There's Plenty of Room at the Bottom,"* which envisioned the direct manipulation of atoms to construct novel materials[1]. Later, in 1974, Norio Taniguchi formally defined nanotechnology as atom-by-atom precision engineering[2]. The advent of advanced microscopy techniques during the 1980s enabled the visualization and manipulation of individual atoms, establishing nanoscience as a distinct and rapidly expanding research field.

1.1 Background of Electrochromism: The Flexible & Multifunctional Electronics.

The continuous evolution of nanotechnology has revolutionized material design, enabling precise control over structural, compositional, and functional characteristics at the nanoscale. This advancement has paved the way for next-generation materials and devices with exceptional optical, electrical, and mechanical properties. As the demand for smart, energy-efficient, and adaptive systems grows, the integration of nanomaterials into functional devices has become central to modern research. Among the various smart material technologies, electrochromism[3,4] has emerged as a promising field owing to its ability to reversibly modulate color and optical transmittance under an applied electric potential. The need for electrochromic materials arises from the pursuit of technologies capable of dynamic energy

management, privacy control, and multifunctional operation. The discovery of electrochromism in tungsten oxide (WO_3) by S. K. Deb in 1969 marked a turning point[5], revealing the potential of materials that could change color in response to electrical stimuli. Since then, research has expanded from inorganic oxides to organic polymers, nanocomposites, and hybrid materials, driven by the goal of achieving flexibility, durability, and multifunctionality. With the advent of flexible and wearable electronics, electrochromic systems have been engineered to combine optical modulation with energy storage, sensing, and thermal regulation, positioning them as key enablers of next-generation smart and sustainable technologies.

1.2 Electrochromism – The Art of Reversible Color Change

Electrochromism, often described as the art of reversible color change, is the phenomenon wherein certain materials undergo a visible and reversible alteration in color, transmittance, or reflectance upon the application of a suitable external electrical stimulus[3,6,7]. This unique property is primarily driven by faradaic or redox reactions occurring at the electrode–electrolyte interface, which induce changes in the oxidation states and electronic structure of the electrochromic materials. The associated movement of electrons through the electrodes and ions within the electrolyte facilitates a coupled ion-electron transfer process that produces optical modulation, which can extend from the ultraviolet (UV) through the visible spectrum to the near-infrared (NIR) region. The reversibility and energy efficiency of this process make electrochromic materials particularly attractive for smart, adaptive, and low-power technologies.

Since its first observation in the early 1960s, electrochromism has evolved into a diverse and multidisciplinary field, propelled by advances in nanoscience, materials engineering, and device fabrication. The

mechanisms of color change vary depending on the material type: in inorganic metal oxides such as WO_3 and NiO, the process involves intervalence charge transfer between metal ions of different oxidation states[8], whereas in organic polymers like polyaniline and PEDOT, the modulation arises from dynamic doping and de-doping processes, which alter the π–π* electronic transitions within the HOMO–LUMO bandgap, generating polaronic and bipolaronic states that produce distinct color changes[9].

The performance of electrochromic devices (ECDs) relies on parameters such as color contrast, switching speed, reversibility, coloration efficiency, and stability, which are crucial for practical applications[10]. Conventional solid-state ECDs consist of an electrochromic layer, ion-storage layer, electrolyte, and two transparent electrodes, forming a compact architecture for efficient optical modulation. Recent research has advanced flexible, wearable, and multifunctional designs that integrate nanocomposites, hybrid electrodes, and energy-storage layers, enabling simultaneous optical switching, energy storage, sensing, or thermal management. By careful material selection, the entire optical spectrum can be tuned, allowing devices for smart windows, displays, mirrors, adaptive camouflage, and electrochromic supercapacitors. Electrochromism thus exemplifies the synergy between materials science, electrochemistry, and nanotechnology, providing a versatile, energy-efficient, and multifunctional platform for next-generation smart electronics.

1.3 Redox-Active Materials: Electrochromic Active Materials

The phenomenon in which the certain materials' changes optical properties (color, transparency or reflectance) on the application of suitable external bias, is called as electrochromism[4] and the materials are called electrochromic (EC) active materials. This optical change of

the EC active materials is typically reversible switches back and forth between two or more colors and main cause of the changes is the ingoing electrochemical redox reaction or the flow of electrons. The two colors or the multicolor switching of the materials depends upon its various redox states. The EC active materials are categorized into two basis (1) material types[11,12] (organic, inorganic and organometallics), (2) based on the bias induced color change[13] that is anodic (changes color on positive bias, p-type) or cathodic (changes color on negative bias, n-type). Additionally, certain materials are both cathodic and anodic; these materials are referred to as ambipolar EC materials. The various EC active materials based on material type and bias induced color change are shown in Table 1.1.

Table 1.1 Various EC active materials.

Material	**Name**	**P-type**	**N-type**	**Ambipolar**
Organic	Poly 3-hexyl Thiophene	✓		
	Poly pyrrole	✓		
	Viologens		✓	
	Polyaniline			✓
	PEDOT: PSS		✓	
Inorganic	WO_3		✓	
	TiO_2		✓	
	NiO	✓		

	Co_3O_4	✓		
	V_2O_5			✓
	MnO_2	✓		
	Nb_2O_5		✓	
	MoO_3		✓	
	Fe_3O_4		✓	
	SnO_2		✓	
	Ta_2O_5		✓	
	ZnO		✓	
Organometallic	Prussian blue			✓

In the latest advances, researchers have expanded the library of EC materials beyond conventional organic and inorganic systems. Emerging candidates such as microporous metal–organic frameworks[14] (MOFs) and covalent organic frameworks[15,16] (COFs) offer tunable porosity and high surface areas, enabling efficient ion transport and enhanced color-switching behavior. Similarly, organic–halide hybrid perovskites[17,18], well known for their exceptional optoelectronic properties, are being explored for their reversible color modulation under applied voltage. In addition, two-dimensional MXenes[19,20], with their outstanding electrical conductivity, layered structures, and rich surface chemistry, have demonstrated promising electrochromic activity. These new material platforms open exciting possibilities for next-generation flexible, multicolor, and high-performance electrochromic devices.

1.3.1 Nanomaterials

Nanomaterials are a promising class of materials with unique structural, electronic, and optical properties, making them useful for a wide range of applications. They are defined as materials in which 50% or more of the particles have one or more dimensions in the 1–100 nm range[21]. Based on the number of nanoscale dimensions, nanomaterials can be classified as follows (**Figure 1.1**):

(1) **Zero Dimensional**: Zero-Dimensional (0-D) nanomaterials have all three dimensions in the 1–100 nm range, typically forming spherical or quasi-spherical nanoparticles, nanoclusters, or nanocrystals. Electrons are confined in all directions, giving rise to unique quantum and optical properties

(2) **One-Dimensional Nanomaterials:** One-Dimensional (1-D) nanomaterials have two dimensions in the nanoscale (1–100 nm) and include nanowires, nanorods, and nanotubes. Electrons are confined in two directions, allowing enhanced electrical, optical, and mechanical properties along the unconfined axis

(3) **Two-Dimensional Nanomaterials:** Two-Dimensional (2-D) nanomaterials have one dimension in the nanoscale (1–100 nm), typically forming sheets or flakes. Electrons are confined in one direction, resulting in unique electronic, optical, and mechanical properties across the extended plane.

(4) **Three-Dimensional Nanomaterials:** Three-Dimensional (3-D) nanomaterials have no dimensions in the nanoscale themselves but are formed by closely packed clusters of 0-D, 1-D, or 2-D nanomaterials. Electrons are not confined in any direction.

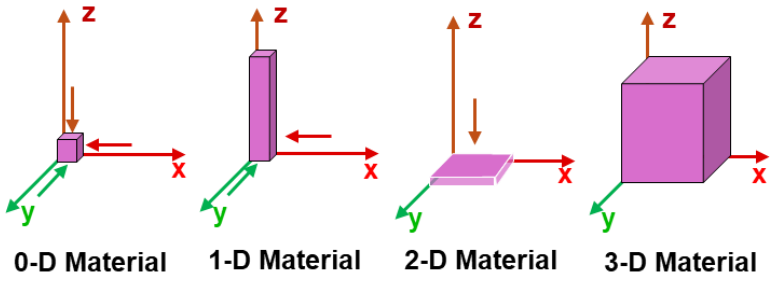

Figure 1.1: Schematic illustration of types of nanomaterials.

1.3.2 Synthesis Methods

With the advancement of nanotechnology, the synthesis of nanomaterials has become highly sophisticated and is generally classified into two main approaches:

- **Top-Down Approach**: The top-down approach involves breaking down bulk materials into nanosized structures through techniques such as physical treatment (includes grinding and milling)[22], chemical treatment (includes etching, hydrolysis, and ablation)[23,24], and laser ablation[25].
- **Bottom-Up Approach:** The bottom-up approach builds nanostructures atom-by-atom or molecule-by-molecule using chemical, physical, or biological processes, such as chemical vapor deposition[26], sol-gel synthesis[27], hydrothermal[28], electrodeposition[29], etc.

1.4 Generic Structure of ECDs.

Electrochromic devices (ECDs) integrate EC active materials for applications such as smart windows, e-curtains, energy storage, and camouflage. A typical ECD consists of two transparent conducting substrates (ITO- or FTO-coated), with one coated with an EC layer and the other with either an ion-storage layer for monolayer devices or another EC layer for bilayer devices. A gel electrolyte is incorporated to prevent leakage and enable ion transport[19].

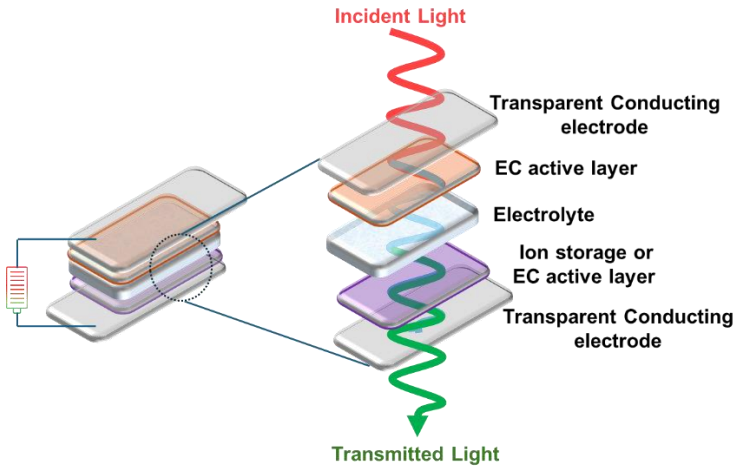

Figure 1.2: Generic structure of an electrochromic device

The growing demand for flexible ECDs has led to the use of ITO-coated PET or other flexible substrates, producing lightweight, thin, and portable devices suitable for wearable electronics and adaptive systems[30]. Flexible devices can also be monolayer or bilayer, depending on the application, while material and device design ensure high performance, mechanical flexibility, and long-term stability.

1.5 The Multifunctional ECDs and Its Applications

In recent years, research in the area of ECDs has risen due to its multifunctional application which can be summarised in the schematic in **Figure 1.3.**

1. Heat Filters / Thermal Control: EC materials like WO_3 and polythiophene block or filter infrared (IR) radiation. Thus, it reduces heat entering buildings, lowering energy consumption for cooling systems[31,32].

2. Solar Cells: The ECDs can store electrical energy generated by sunlight. Device color changes reflect the charge storage state, returning to the original color when energy is used [33].

3. Sensors: Certain EC materials, e.g., MoO_3, can detect specific chemicals such as HF. Useful for environmental monitoring and chemical detection [34].

4. Camouflage / Adaptive Coatings: The ECDs dynamically adapt to surroundings (deserts, forests, snow, seas) under applied bias. Advantages include lightweight, flexible, low-bias operation, suitable for wearable applications, vehicles, or tents for security and stealth purposes[35].

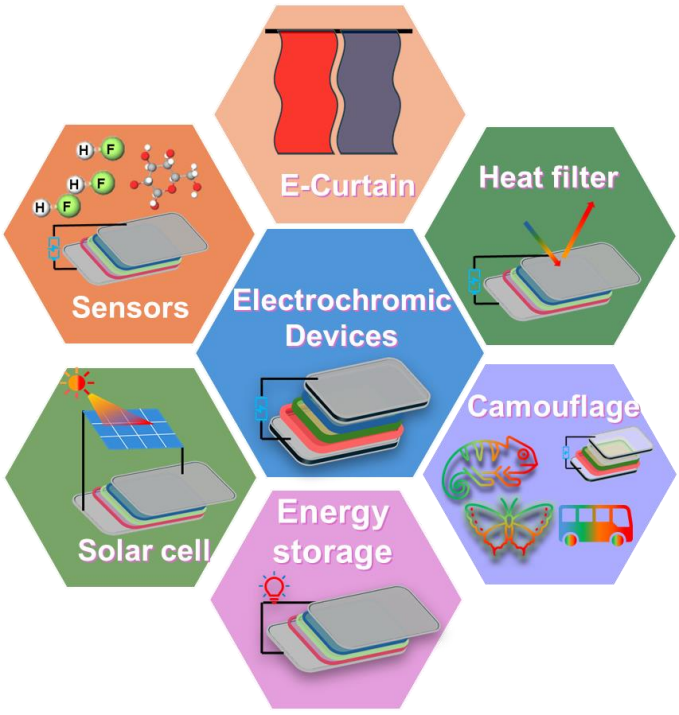

Figure 1.3: Schematic showing various application of ECDs.

5. E-Curtains and Smart Windows: Flexible windows or curtains that adjust light transmission by changing color. Helps control indoor lighting and improves comfort while reducing glare[36].

6. The EC Supercapacitor Device: Energy storage devices store energy and release it when needed to perform useful work[37]. Batteries provide high energy density, capacitors offer high power density, and supercapacitors bridge the two, delivering both high energy and power

density while offering fast charging, long cycle life, and high stability. Since ECDs and pseudocapacitors share a similar mechanism, ECDs can also store charge via ion diffusion[38]. Their color modulation property allows them to function as color-indicating supercapacitors, visually showing charging and discharging states. Depending on the charge storage mechanism, supercapacitors are classified as (**Figure 1.4**):

i. **Electric Double Layer Capacitors (EDLC):** EDLCs store charge physically at the electrode–electrolyte interface through electrostatic ion adsorption, known as non-faradaic reaction, offering high power density and excellent cyclic stability but relatively lower energy density, with common electrode materials including activated carbon, graphene, and carbon nanotubes.

ii. **Pseudocapacitors:** The pseudocapacitors store charge chemically via fast and reversible surface redox reactions also called as faradic reaction, providing higher energy density while maintaining good power density, though with slightly lower cyclic stability, and typically employ metal oxides (e.g., TiO_2, MnO_2) or conducting polymers as electrode materials.

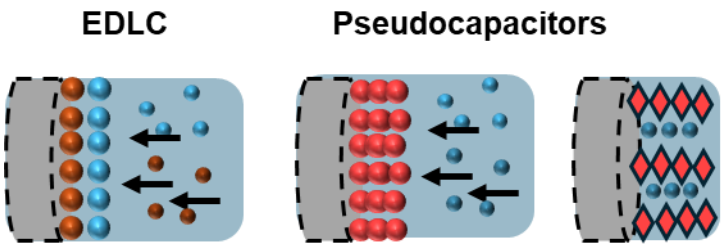

Figure 1.4: EDLC (non-faradic) and pseudocapacitive (Faradic) charge storage mechanisms.

Based on device fabrication, EC supercapacitors are classified into:

1. **Symmetric**: A symmetric EC supercapacitor is an electrochemical capacitor with two identical electrodes[38], having the same material, design, and mass, and sharing a similar charge storage mechanism. These devices typically offer intermediate power density along with high cyclic stability, making them reliable for long-term energy storage applications.
2. **Asymmetric:** An asymmetric EC supercapacitor has two different electrodes, typically combining an EDLC-type with a pseudocapacitive electrode[39]. This design provides a wider operating voltage and enhanced performance. It delivers both high energy density and high-power density compared to symmetric devices.

1.6 Electrochromic Supercapacitor Device Performance Metrics

Before being used as a final application, the performance of a ECD and EC supercapacitor device fabricated according to the device schematic (**Figure 1.2**) must be thoroughly evaluated using several key parameters to assess its functionality and efficiency:

1.6.1 Color or Optical Contrast

The color contrast (CC) or optical contrast (OC) is a quantitative measure of the visible optical changes that occur during the modulation of an ECD. It is determined by performing in-situ optical spectroscopy on the device or electrode at a specific wavelength during the color-changing process. The CC ratio calculates the net change in transmittance value between two colored states or one bleached state of the device, and is expressed in percent using the following equation (Eq. 1.1:

$$Color\ Contrast\ (\%) = \frac{(T_f - T_i)}{T_i} \times 100\ or\ \frac{(T_f - T_i)}{T_f} \times 100, \quad (1.1)$$

where T_f , T_i are the initial and final transmittance values displayed by the device or electrode. Alternatively, this equation is also applicable to the initial and final absorbance values of the device.

1.6.2 Coloration Efficiency

Coloration efficiency (η_{ce}) is a key parameter for evaluating the performance of an ECD. At a given wavelength, η_{ce} represents the ratio of the change in optical density (OD) between the colored and bleached states to the charge injected or extracted per unit area of the working electrode, as expressed in Eq. (1.2)

$$\eta_{ce} = \frac{\Delta OD\ (\lambda)}{Q} \quad \text{or} \quad \frac{\log_{10}(\frac{1}{T})}{Q} \tag{1.2}$$

here the $\Delta OD(\lambda)$, T and Q represents the change in optical density, Transmittance and charge density respectively at particular wavelength where the CC value is high. The value of η_{ce} can be obtained from the slope of the graph between the $\Delta OD(\lambda)$ and Q .

1.6.3 Switching/Response Time

When an adequate bias is applied to the ECD, its color changes from one state to another (colored state), and when reversive bias is applied, it returns to its original color (bleached state). The time necessary to switch from the original state to the colored state and from the colored state to the bleached state is known as switching time (usually estimated at 67%, 77%, or 90% of total coloration or bleaching).

1.6.4 Cyclic Life

To study the multiple switching between coloration and bleaching or the cyclic stability of the ECD, it is toggled multiple times between the colored and bleached state by applying continuous square pulse of voltages for particular time period and the corresponding transmittance/reflectance value is measured for a certain period of time.

1.6.5 Specific Capacitance

Specific capacitance is a key parameter for estimating the charge storage capacity of an electrode or device. It can be calculated from the GCD (galvanostatic charge–discharge) profile using Eq. 1.3:

$$C_s = \frac{i\Delta t}{m\Delta V} \text{ or } \frac{i\Delta t}{A\Delta V}, \tag{1.3}$$

here, i/m or i/A is the current density, Δt is the discharging time, and ΔV is the potential window. Another way to determine the specific capacitance is using CV using Eq. 1.4:

$$C_s = \frac{\int IdV}{2vm\Delta V}, \tag{1.4}$$

here, $\int IdV$ is the area under the CV, m is the mass deposited over the substrate, v is the scan rate, and ΔV is the potential window.

The mass 'm' can be replaced by active area 'A' of the electrode if the mass deposited over the substrate is unknown.

1.6.6 Columbic Efficiency

The Coulombic efficiency is the ratio of the charge extracted from the device or electrode to the amount of charge stored. The Coulombic efficiency of the device can be calculated using Eq. 1.5.

$$Coulombic\ Efficiency = \frac{\Delta t_d}{\Delta t_c}, \tag{1.5}$$

here, Δt_d and Δt_c is the discharging and charging time of the device.

1.6.7 Capacitive Retention

The capacitive retention of the device is a parameter used to determine the cyclic life or stability of the device with a number of cycles. The percentage of capacitance retention can be calculated using Eq. 1.6.

$$Retention\ \% = \frac{Capacitance\ at\ n^{th} cycle}{Capacitance\ at\ 1^{st} cycle} \times 100, \tag{1.6}$$

The device with high capacitance retention gives high stability and is desirable for real-life applications.

1.6.8 Ragone Plot

The Ragone plot is the plot of energy density vs power density. The energy density of the device can be calculated using Eq. 1.4.

$$Energy\ density = \frac{C_s(\Delta V)^2}{2\times3.6}, \quad (1.7)$$

The power density of the device can be calculated using Eq. 1.5.

$$Power\ density = \frac{Energy\ density}{\Delta t_d}, \quad (1.8)$$

The Ragone plot of the device is a comparative parameter that usually compares the energy and power density of the device with those already reported in the literature.

1.7 Main Objective of the Work

- To develop an understanding of electrochemical-based electrodes for EC applications and their device fabrication.
- To utilize metal oxides, metal chalcogenides, MXene, perovskites and carbonaceous materials for the fabrication of EC solid and flexible devices and investigate their role in enhancing the device's performance in EC and other diverse fields.
- To understand the mechanism of color change during the device's operation using in-situ techniques vis-à-vis, UV-vis spectroscopy.
- To understand the parameters involved in the fabrication of ECD by the doping of various inorganic and organic complexes.
- To synthesise organic and inorganic EC active electrodes using various methods and to investigate EC performance and charge storage applications of it.

♦ Explore the possibility beyond the EC for the application of prepared nano and microstructures in other areas like supercapacitors and heat shielding.

♦ Designing improved all-organic and inorganic ECD with supercapacitor application by incorporating novel synthesized EC material and investigating its performance in both solid, flexible, and large-area electrodes.

1.8 Organization of Thesis

The above-mentioned studies (detailed results and discussion with experimental methodologies) have been complied in the thesis by adopting the following chapter-wise plan:

❖ **Chapter 1:** The current chapter provides an overview of the pertinent topics related to the thesis work and establishes the objectives that the thesis aims to achieve.

❖ **Chapter 2:** Deals with the details of the experimental methodology used for the experimental work carried out along with details of various experimental parameters and procedures followed for the fabrication of EC materials. It also summarizes details of various equipment used for characterization.

❖ **Chapter 3:** It deals with the doping effect of complementary metal oxides (WO_3 and Co_3O_4) and metal oxides-metal chalcogenides mixture (WS_2/WO_3) in all-organic flexible ECDs with heat shielding application.

❖ **Chapter 4:** It deals with the effect of 2-D layered materials of MXene for enhancing the performance of all-organic solid-state ECD with charge storage applications.

❖ **Chapter 5:** It describes the role of high dielectric perovskites ($CoTiO_3$) for supercapacitor application in all-organic solid state ECD.

❖ **Chapter 6:** The doping role of various carbonaceous material (Graphene and Graphene Oxide) in metal oxide (NiO) in all-inorganic asymmetric EC supercapacitor devices has been explored.

❖ **Chapter 7:** It summarizes all the conclusions drawn based on the research work reported above. This also includes future scope of works that may be carried out to enhance the understanding in the field.

Chapter 2

Experimental Techniques

This chapter provides a comprehensive overview of the methodology employed to fabricate various samples, including metal oxides, metal oxide-chalcogenides mixture, perovskite $CoTiO_3$, 2-D MXene, Graphene Oxide, electrodes, and devices. Additionally, it discusses the range of experiments techniques used to characterize these materials and evaluate their applications parts. Details of the instruments including X-ray diffraction (XRD), Scanning electron microscopy (SEM), Ultraviolet-Visible spectroscopy (UV-Vis), Atomic force microscopy (AFM), X-ray photoelectron spectroscopy (XPS), Electrochemistry and Raman spectroscopy have been provided. The chapter covers the fundamentals of electrochemistry, including cyclic voltammetry (CV), electrochemical impedance spectroscopy (EIS), and galvanostatic charge/discharge. These aspects are organized into two main sections: sample preparation and instrumentation, as discussed below.

2.1 Sample Preparation Techniques

Various synthesis techniques such as the sol-gel method, Co-precipitation, hydrothermal, electrodeposition, and selective etching technique have been used to synthesize various nanomaterials such as cobalt oxide (Co_3O_4), tungsten oxide powder (WO_3), tungsten sulphide/oxide mixture (WS_2/WO_3), WO_3 film, 2-MXene, Perovskite $CoTiO_3$, Graphene and graphene Oxide.

2.1.1 Sol-Gel Method

The sol-gel method is a bottom-up approach that utilizes small molecular precursors to synthesize nanomaterials, particularly metal oxides[40]. This technique involves a series of carefully controlled steps, which are outlined as follows:

1. Sol formation: Hydrolysis of metal precursors such as metal nitrates and metal sulfates in water, resulting in a homogeneous solution.
2. Gel-formation: Condensation and polycondensation of solution by adding surfactants and gelators such as citric acid and ethylene glycol. The addition results in a solution in the formation of a gel.
3. Calcination: During calcination, the pores of the gel network collapse, and the remaining organic species are volatilized, resulting in the formation of metal oxides.
4. Heat treatment: During heat treatment, the material is transformed into desired forms, such as films, fibers, and nanosized powders.

The sol-gel method allows precise control over nanostructure size, shape, and morphology through gelation and heat treatment. Its versatility with various precursors enables the synthesis of oxides, sulfides, and metal nanoparticles.

2.1.2 Co-Precipitation

The co-precipitation method is a widely used chemical technique for synthesizing nanomaterials by simultaneously precipitating multiple

precursors from a homogeneous solution[41] (**Figure 2.1**). This approach allows precise control over particle size, composition, and morphology by adjusting key parameters such as pH, temperature, and reactant concentration. It is simple, cost-effective, and scalable, making it suitable for large-scale production of nanomaterials.

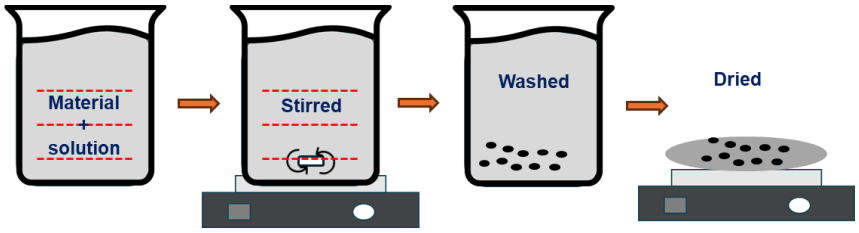

Figure 2.1: Co-precipitation synthesis method step by step.

This method is particularly versatile, enabling the synthesis of a wide range of inorganic materials, including metal oxides, sulfides, and mixed-phase compounds. Its ability to produce uniform and highly pure materials makes it highly valuable in research areas such as catalysis, energy storage, and electronic applications. Overall, co-precipitation provides a robust platform for designing functional nanomaterials with tailored properties for advanced technological applications.

2.1.3 Hydrothermal

The term “hydrothermal” combines “hydro” and “thermal,” referring to a method for synthesizing nanocrystals through chemical reactions at high temperature and pressure in a sealed aqueous environment[42]. In this method, the precursor solution is stirred to achieve homogeneity and then transferred to a Teflon-lined stainless-steel autoclave (**Figure 2.2**), which is heated in an oven.

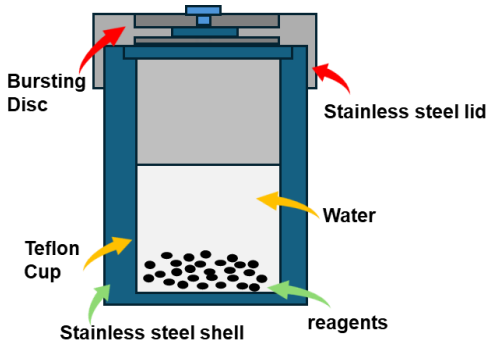

Figure 2.2: Schematic illustration of a hydrothermal setup

The temperature generates pressure, which is crucial for controlled nanostructure growth. External parameters such as reaction time and heating/cooling rates influence the size, shape, and morphology of the nanomaterials. A limitation of this method is that the requirement of sealed vessels restricts scalability and increases the complexity and cost of large-scale production.

2.1.4 Electrodeposition

The term "electrodeposition" refers to the formation of thin films at the electrode–electrolyte interface, driven by the passage of electric current[43]. Typically, a three-electrode configuration-comprising a working electrode (WE), reference electrode (RE), and counter electrode (CE)-is employed to regulate charge transfer using an external power source (**Figure 2.3**).

In this setup, Pt wire and Ag/AgCl serve as the CE and RE, respectively, while conducting substrates such as ITO, FTO, or carbon cloth act as the WE. By controlling parameters such as applied potential or current, electrolyte concentration, and deposition time, different morphologies of thin films can be achieved. Electrodeposition offers several advantages, including uniform film formation, strong substrate adhesion, high stability, and precise thickness control, making it a versatile technique for fabricating functional devices across various applications

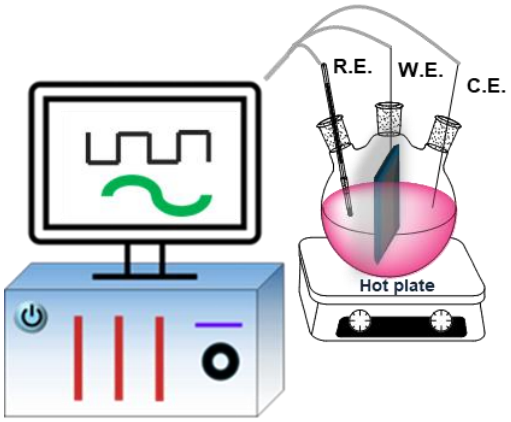

Figure 2.3: Schematic of electrodeposition setup with three electrodes.

2.1.5 Selective Etching Method

The chemical etching process is a top-down approach employed for nanomaterial synthesis, involving the selective removal of material from a substrate using chemical solutions containing oxidizing or reducing agents[44]. This method enables the controlled fabrication of nanostructures by tuning parameters such as reagent concentration, temperature, and reaction time. The wet chemical etching process typically involves three key steps:

i. Addition of an acid to remove the selective layer like A layer from the MAX phase to form the MXene,

ii. The washing step to remove the dirt particles and maintain the pH.

iii. The heat treatment process to get desired materials.

This versatile and cost-effective method allows precise control over particle size and morphology, facilitating the synthesis of various metal oxide nanomaterials with tailored structural and functional properties for advanced applications.

2.1.6 Hummer's Method

Hummer's method[45,46] is a widely used wet chemical technique for synthesizing graphene oxide (GO) from graphite powder through strong oxidation. It is considered a top-down approach, as it involves breaking

down bulk graphite into individual graphene oxide layers via chemical exfoliation. In this process, graphite is treated with concentrated sulfuric acid (H_2SO_4) and phosphoric acid (H_3PO_4), which introduce oxygen-containing functional groups (such as hydroxyl, epoxy, and carboxyl) into the graphite layers. These functional groups weaken the van der Waals interactions between layers, enabling exfoliation into GO sheets. The resulting GO can then be chemically or thermally reduced to obtain reduced graphene oxide (rGO) or graphene. Hummer's method is advantageous due to its simplicity, scalability, and ability to produce highly oxidized, dispersible graphene derivatives suitable for various electronic and electrochemical applications.

2.1.7 Spin-Coating

Spin coating is a widely used technique for depositing thin films from a liquid precursor onto a substrate, and its effectiveness depends on the material's initial state and the substrate's properties[47]. In this process, a small amount of solution is dropped onto the substrate, which is then rapidly rotated to spread the material uniformly through centrifugal force (**Figure 2.4**). The substrate, fixed to a spinning rotator, accelerates at high speed, forming a uniform and smooth film.

The resulting film thickness is primarily governed by parameters such as solution viscosity, concentration, and spinning speed. After the spin coating the sample over the substrate it was dried by giving some heat. Spin coating offers advantages including simplicity, cost-effectiveness, and excellent control over film uniformity, making it ideal for fabricating thin films used in electronic, optical, and energy devices.

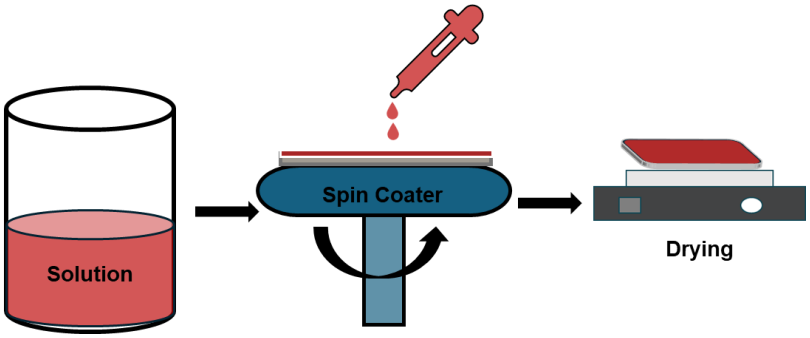

Figure 2.4: The schematic illustration of spin-coating technique.

2.1.8 Drop Casting

The drop-casting technique is a simple and versatile method for depositing thin films from a liquid precursor solution. In this process, a small droplet of the material is placed onto the substrate surface using a pipette, where it spreads and forms a thin film as the solvent evaporates[47] (**Figure 2.5**). The film thickness can be tuned by varying the solution concentration and droplet volume. This method requires minimal equipment and is suitable for rapid film preparation on various substrates. However, achieving uniform thickness across the entire surface remains challenging due to uneven solvent evaporation and droplet spreading. Despite this limitation, drop-casting is widely used for fabricating thin films in optoelectronic, sensing, and energy storage applications.

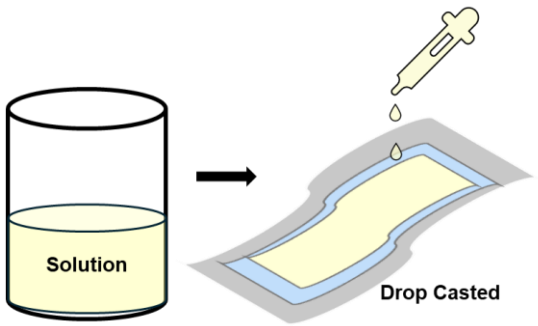

Figure 2.5: The schematic representation of drop casting method.

2.2 Synthesis of Materials

2.2.1 Cobalt Oxide (Co_3O_4)

The Co_3O_4 was synthesized using simple sol-gel method as described earlier[48]. Cobalt nitrate hexahydrate and urea were dissolved in 30ml deionized water in separate beakers in 1:1 molar ratio. Both the above prepared solutions were then mixed and stirred for 2 hours at room temperature. Then the homogeneously prepared solution was dried at 80°C under intense stirring to evaporate the excess water present. The powder obtained was then calcined at 400°C for 4 hours. The obtained powder was kept in desiccator for further characterization.

2.2.2 Tungsten Oxide (WO_3)

For the preparation of ultra fine powder of WO_3, a simple co-precipitation method has been adopted[49]. Initially, 0.33 g of Sodium tungstate was added to 20ml di water and was stirred continuously. 2 M HCl was added drop wise to the above prepared solution to maintain the pH of the solution at 1.5 and was stirred for next 13 hours. Then the prepared precursor solution was rinsed three times with deionized water and ethanol to remove all the impurities. The precipitate obtained was dried for 16 hours at 50°C, to get yellow color powder. The obtained powder was calcined at 450°C for 24 hours. After calcination the obtained powder was kept in desiccator for further characterization without any further purification.

2.2.3 Tungsten Oxide/ Tungsten Sulfide (WO_3/WS_2) Mixture

A single-step hydrothermal method was employed to synthesize WS_2/WO_3 nanoflakes. The process began with a 1:3 weight ratio of ammonium paratungstate $[(NH_4)_{10}(H_2W_{12}O_{42})\bullet 4H_2O]$ and thiourea $[(NH2)_2CS]$. These precursors were dissolved in 70 mL of de-ionized water with continuous stirring for 30 minutes, resulting in a homogeneous, colorless solution. This solution was then transferred to a 100 mL Teflon-lined stainless steel hydrothermal reactor, which was

heated to 240°C in a muffle furnace for 3 hours before being allowed to cool to room temperature. The resulting greyish black precipitates was collected by centrifugation and thoroughly washed with de-ionized water and ethanol. Finally, the reaction product was dried overnight in a vacuum oven at 60°C[50,51].

2.2.4 Cobalt Titanate ($CoTiO_3$)

$CoTiO_3$ nanoparticles were synthesized using a sol-gel method as described earlier [52]. Shortly, 3.4 ml of titanium (IV) n-butoxide were added to 30 ml anhydrous ethanol and stirred for 30 minutes. In the mixture solution 4.202 g citric acid and 2.362 g cobalt nitrate has been added and stirred continuously for another 90 minutes at 50 °C. Then the mixture was dried at 80 °C for 12 hours in the oven to obtain the gel. The obtained gel was calcined at 700 °C in muffle furnace. The powder obtained after calcination was used for further characterization and device application without any purification.

2.2.5 MXene Titanium Carbide ($Ti_3C_2T_x$)

The MXene ($Ti_3C_2T_x$) was prepared by selectively removing the aluminum layer from the MAX (Ti_3AlC_2) phase[53,54]. At first, 5 ml of deionized water was introduced into a teflon container, followed by the addition of 15 ml of HCl (12 M) and 1.6 g of LiF. Subsequently, 1.0 g of Ti_3AlC_2 was gradually added into the solution over a period of 5 minutes, with continuous stirring at a speed of 300 rpm for 22 h. Subsequently, the suspension underwent centrifugation at a speed of 5000 rpm for a duration of 10 minutes, with this process being repeated until the pH reaches a state of neutrality (above 6). Ultimately, $Ti_3C_2T_x$ that was acquired underwent filtration and was thereafter dried at a temperature of 60 ˚C for 8 h in a vacuum oven. After the successful synthesis of the MXene ($Ti_3C_2T_x$), solid state electrochromic device has been fabricated by incorporating MXene.

2.2.6 Graphene (Gr) and Graphene Oxide (GO)

The graphene nano-flakes were synthesized by simply ultrasonically dispersing the 10 g graphite powder in 50 ml DI water for 24 hours, followed by filtration using Whatman filter paper. The obtained material was then dried in an oven at 60°C for couple of hours and stored in a glass vial for later use.

The synthesis of graphene oxide was done using Hummers' method[55]. A 400 ml acidic solution was prepared by combining concentrated H_2SO_4 and H_3PO_4 in a 9:1 ratio. Subsequently, 3 g of graphite powder was added, and the mixture was stirred at room temperature for 30 minutes to ensure uniform dispersion. Afterward, 18g $KMnO_4$ was added slowly to the above solution and again stirred for 2 hours at 50°C, and then allowed to cool to room temperature, followed by the addition of 3 ml H_2O_2, and the solution was quenched by the addition of 400 ml of crushed ice. The solution was then centrifuged at 4000 rpm for 2 hours and filtered using Whatman filter paper. Following multiple washes with HCl and DI water, the residual solid material was dried overnight at 70°C in a vacuum oven. For later use, the produced graphene oxides were gathered and stored in a clean glass vial.

2.3 Electrode Preparation

The ITO/FTO coated glass substrates are used to get the solid-state ECD and for the fabrication of flexible ECD the ITO-coated PET (polyethylene terephthalate) substrate is used. Prior to the synthesis of all the electrodes the ITO/FTO coated glass substrate were cleaned ultrasonically in the solution containing acetone, isopropanol alcohol (IPA), and distilled water, then dried for further use. The flexible ITO coated PET substrates are cleaned using the DI water only.

2.3.1 Poly (3-Hexylthiophene), P3HT Electrode (Flexible/ solid state)

1. A 0.4 wt.% P3HT solution was prepared by dissolving P3HT in dichlorobenzene (DCB) to obtain a homogeneous mixture.
2. Approximately 50 μL of the prepared solution was spin-coated onto the ITO/FTO glass and PET substrate at 600 rpm for 120 seconds.
3. The resulting film was dried in an oven at 80 °C for 1 hour to ensure solvent removal and film stabilization.

2.3.2 The Co_3O_4 – Doped P3HT Electrode

1. The 0.1 wt.% Co_3O_4 has been doped in 4 wt.% P3HT solution prepared in the DCB to get the uniform solution.
2. Approximately 50 μL of the prepared solution was spin-coated onto the ITO/FTO PET substrate at 600 rpm for 120 seconds. The electrode was dried at 80°C for 30 minutes.

2.3.3 The WO_3 – Doped Ethyl Viologen (EV) Electrode

1. A 5wt.% PEO (polyethylene oxide) in ACN and 4wt.% EV in ACN (Acetonitrile) has been prepared in separate glass vial.
2. A 0.1 wt.% WO_3 has been doped in EV solution. The WO_3 doped EV is mixed with PEO mixture in equal proportion (1:1), it was drop casted on another PET substrate.

2.3.4 The WS_2/WO_3-Doped EV Electrode

1. In a separate glass vial 4 wt.% EV in ACN was prepared and 0.1 wt.% WS_2/WO_3 mixture was doped in the solution of EV.
2. In another vial 5 wt.% PEO in ACN was prepared to get the gel consistency, both the prepared solution (WS_2/WO_3 mixed EV and PEO gel) were mixed in equal amount to get the gel like consistency.
3. The produced gel was drop-casted over a second cleaned ITO coated PET substrate

2.3.5 MXene $Ti_3C_2T_x$ -Doped EV Electrode

1. A 0.1 wt.% MXene, 5 wt.% PEO, and 3 wt.% EV were prepared in acetonitrile. The prepared solution was mixed together in equal proportion.
2. Approximately 5 μL of the solution was drop casted over the cleaned ITO to get the final doped electrode.

2.3.6 Perovskite $CoTiO_3$-Doped P3HT Electrode

1. For the fabrication of $CoTiO_3$ doped P3HT (say CTO-P3HT) electrode, 0.2 wt.% $CoTiO_3$ was mixed with 0.5 wt.% P3HT in DCM and mixed properly using vortex mixing.
2. Thin film has been grown in ITO glass substrate using the spin coating method at 600 rpm for 120 seconds, has been dried at 70 °C for 30 minutes.

2.3.7 The WO_3 Electrode

1. For synthesis of WO_3 electrode, 0.015 M H_2O_2 (Hydrogen peroxide) was added to the 0.0125 M sodium tungstate solution under constant stirring.
2. Afterward, 0.48 M HNO_3 (Nitric acid) has been added to the previously prepared solution of WO_3 to maintain the pH of the solution and called as WO_3 precursor solution.
3. A constant voltage of -0.47 V has been applied to ITO glass substrate to grow WO_3[56] electrochemically using the above prepared WO_3 precursor solution in three electrode system, Ag/AgCl as reference electrode and platinum wire as counter electrode for 300s, after that it was dried at 70 °C for 1 hour in hot plate (**Figure 2.6**).

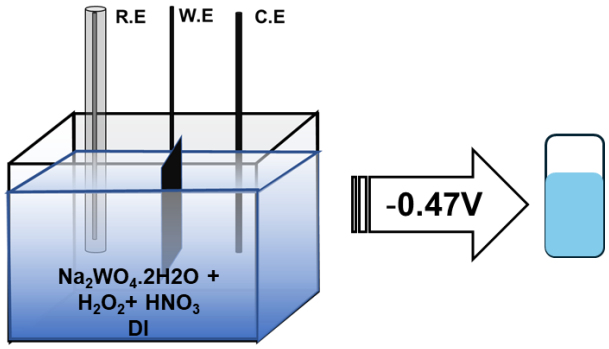

Figure 2.6: Schematic representation of WO_3 electrode preparation.

2.3.8 The NiO Electrode

1. The synthesis of nickel oxide (NiO) electrodes was done using the spin-coating method with slight modification[57,58] and as shown schematically in **Figure 2.7**.

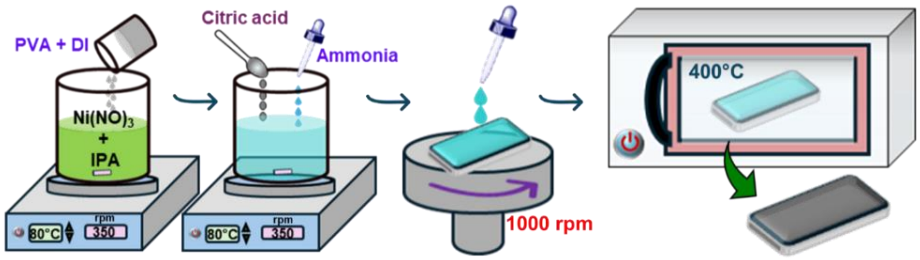

Figure 2.7: Generic synthesis route for the fabrication of NiO.

2. The NiO precursor solution was prepared by dissolving 0.872 g of $Ni(NO_3)_2 \cdot 6H_2O$ (nickel nitrate hexahydrate) in 15 ml of IPA under continuous stirring. Subsequently, a solution of 1 g polyvinyl alcohol (PVA) in 15 ml DI water was added dropwise to the above mixture, followed by continuous stirring at 80 °C until a homogeneous solution was obtained.

3. After proper mixing of the solutions, 2 ml ammonia solution was added dropwise, followed by the addition of 1g citric acid. The final NiO precursor solution was stirred at 350 rpm at 80°C overnight to get a uniform solution.

4. The NiO precursor solution (50 µl) was spin-coated over the cleaned FTO-coated glass substrate at 1000 rpm for 30s and was annealed at 400°C in a muffle furnace for 20 minutes. The NiO-coated electrode was used again, and the same procedure of spin coated was repeated for five cycles.

2.3.9 The Gr/GO-Doped NiO Electrode

1. For the synthesis of graphene-doped NiO (say Gr-NiO) and graphene oxide-doped NiO (say GO-NiO) electrodes, 5mg of the fabricated nano-flakes of each material, were added to 1 ml IPA and were mixed properly using the mortar and pestle, then, were collected in two different cleaned Eppendorf tubes, namely Gr solution and GO solution.

2. In two separate cleaned glass vials, 5 ml of the NiO precursor solution was taken and 50 µl of the above prepared solutions of Gr and GO were added and named as Gr-NiO precursor solution and GO-NiO precursor solution.

3. The prepared precursor solutions of Gr-NiO and GO-NiO were used for fabricating the Gr-NiO electrode and GO-NiO electrode using the procedure mentioned in **section 2.3.8**, by spin coating the precursor solutions. All the fabricated electrodes were carefully marked and kept in vacuum desiccators.

2.4 Characterization Techniques

Various characterization techniques were employed to analyze the prepared samples and understand their structural, optical, and electrochemical properties. Microscopic, spectroscopic, and electrochemical measurements were performed to evaluate the performance of the materials and devices. A brief description of the working principles of these techniques has been provided below:

2.4.1 Scanning Electron Microscopy

Scanning Electron Microscopy[59] (SEM) is a powerful analytical technique used to examine the surface morphology and microstructural features of materials. In this technique, a focused beam of high-energy electrons interacts with the specimen, generating various signals that provide information about the surface topography, morphology, chemical composition, and other material properties. An SEM system consists of several key components, including an electron gun for generating electrons, electromagnetic lenses for focusing the beam, scanning coils for beam deflection, a vacuum chamber to maintain stability, and detectors such as secondary and backscattered electron detectors for image formation (**Figure 2.8**). Together, these components enable high-resolution imaging and detailed surface characterization of the specimen.

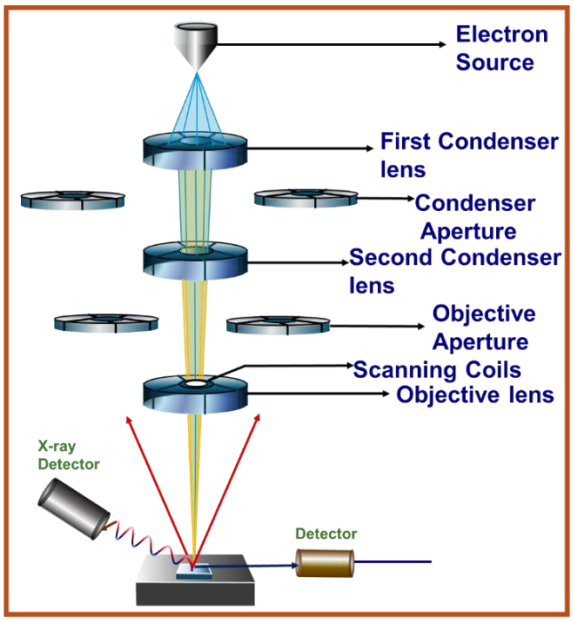

Figure 2.8: Schematic illustration of major components of scanning electron microscopy.

Model Used: A 7610F Plus/JEOL field emission scanning electron microscope (FESEM).

2.4.2 Transmission Electron Microscopy

Transmission Electron Microscopy[60] (TEM) is a powerful characterization technique used to investigate the internal structure, crystallography, and morphology of materials at atomic to nanometer scales. In TEM, a high-energy electron beam is transmitted through an ultrathin specimen. As the electrons interact with the sample, they undergo scattering, and the transmitted or diffracted electrons are used to form high-resolution images. TEM enables detailed analysis of lattice structures, grain boundaries, defects, and phase distributions, making it invaluable for materials science and nanotechnology studies.

A Transmission Electron Microscope (TEM) comprises several key components that work together to produce high-resolution images. The electron gun generates high-energy electrons, which are focused onto the ultrathin specimen by the condenser lenses. The objective, intermediate, and projector lenses magnify the transmitted image, while the specimen stage allows precise positioning and tilting. A vacuum system prevents electron scattering, and imaging detectors such as fluorescent screens or CCD cameras capture the transmitted electron patterns for structural and compositional analysis.

Model Used:

(1) The TEM was done using FEI Tecnai G2 F20 TMP running an emission field gun at 200 kV used for $CoTiO_3$.

(2) The HRTEM, JOEL Japan, JEM-2100 Plus

2.4.3 X-ray Diffraction

X-ray diffraction (XRD) is a versatile and non-destructive technique used to study the physical properties of powders, solids, and liquids, including their phase composition, crystal structure, and orientation[61,62]. The X-rays, which are electromagnetic radiation with wavelengths around 1 Å, diffract upon interacting with a crystalline

material, where the crystal lattice planes act as diffraction elements. The working principle of XRD is based on **Bragg's law**, which states that constructive interference occurs when X-rays incident on a crystal with interlayer spacing $\boldsymbol{d}$ at an angle θ satisfy the condition that the path difference equals an integer multiple n of the wavelength λ. Mathematically, this is expressed as Eq. 2.1.

$$2dsin\theta = n\lambda \ , \tag{2.1}$$

Each atom within the crystal lattice acts as a diffraction center and collectively creates a grating-like effect for diffracting X-rays.

The major components of the XRD are as below (**Figure 2.9**).

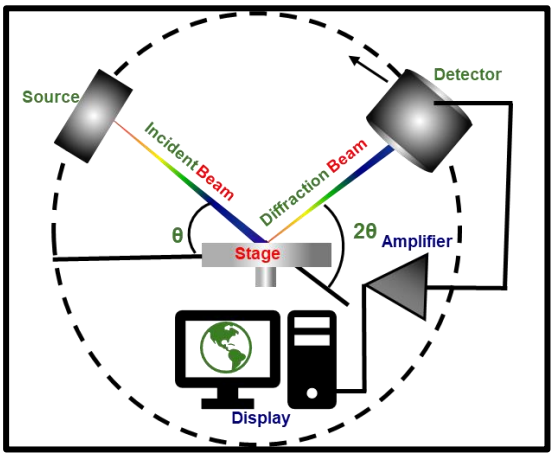

Figure 2.9: Schematic illustration of major components of X-ray diffractometer.

Model Used: Rigaku Smart lab Multipurpose Versatile XRD having Cu Kα radiation of wavelength 1.5 Å.

2.4.4 Raman Spectroscopy

Raman spectroscopy is used to study the chemical structure and molecular properties of materials[63]. When exposed to monochromatic light, the photons are absorbed, reflected, or transmitted, while a small fraction is scattered, resulting in different frequency of light when compared to incident light. Light scattered at the same frequency is the

Rayleigh component, and light with shifted frequencies forms the Raman component, including Stokes (energy loss) and Anti-Stokes (energy gain) lines. The frequency shifts correspond to the vibrational energy levels of the sample, providing detailed structural and chemical information. Various components used in Raman spectroscopy are described below (**Figure 2.10**).

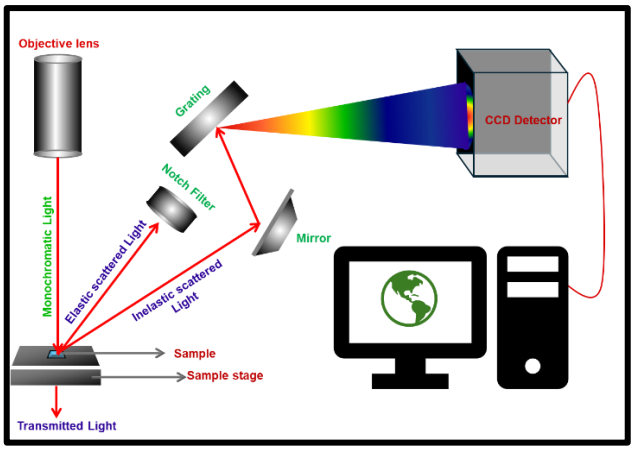

Figure 2.10: Schematic illustration of major components of Raman spectrometer.

Model Used: Horiba Jobin-Yvon spectrometer using wavelengths 532 and 633 nm.

2.4.5 UV-Vis Spectroscopy

UV-Vis spectroscopy is a powerful analytical technique used to study the electronic structure and properties of molecules[64]. It measures the light absorbed by the material in solution or solid state by exposing it to light in the 200–1100 nm wavelength range. Electrons in the material absorb specific wavelengths and are excited from the ground state to higher energy levels, while other wavelengths are either transmitted or reflected. The characteristic absorption peaks can identify specific compounds, and the absorbance can be used to quantify concentration using Beer-Lambert's law (Eq. 2.2 and 2.3):

$$A \propto c \times l, \tag{2.2}$$

$$A = \in \times c \times l, \tag{2.3}$$

here ∈ is the molar absorptivity coefficient constant, l is the path length of the cuvette or sample holder (usually 1 cm), and c is the concentration of the solution (M). Various components used in UV-Vis spectroscopy are shown in **Figure 2.11**.

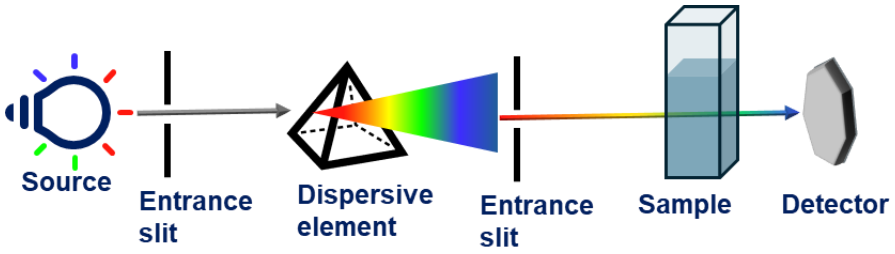

Figure 2.11: Schematic of an UV-Vis spectrometer

Model Used: PerkinElmer, lambda 365 spectrophotometer

2.4.6 X-ray Photoelectron Spectroscopy

X-ray Photoelectron Spectroscopy (XPS) is a surface-sensitive analytical technique used to determine the elemental composition, chemical states, and electronic structure of materials[65]. In XPS, the sample is irradiated with monochromatic X-rays, causing the emission of core-level electrons via the photoelectric effect. The kinetic energy of these emitted electrons is measured, and from this, the binding energy is calculated, providing detailed information about the elements and their chemical environments. Main Components of XPS are:

1. X-ray Source: Produces monochromatic X-rays to irradiate the sample, commonly Al Kα or Mg Kα.
2. Ultra-High Vacuum (UHV) Chamber: Maintains a vacuum to prevent scattering of emitted electrons.
3. Electron Energy Analyzer: Measures the kinetic energy of photoelectrons with high resolution.
4. Sample Stage: Holds and positions the sample, allowing rotation and tilt for optimal analysis.

5. Detector: Collects and counts the emitted electrons to generate spectra showing elemental composition and chemical states.

Instrument Used: Survey scans were recorded with an X-ray source power of 50 W and pass energy of 187.85 eV. High-resolution spectra of the major elements were recorded at 46.95 eV pass energy. All the XPS data were processed using PHI's Multipak software. The binding energy was referred to the C 1s peak at 284.8 eV.

2.4.7 Electrochemical Measurement.

Electrochemical measurements are widely used to investigate ion transport mechanisms in materials. Typically, a three-electrode setup is employed, consisting of a working electrode (WE), reference electrode (RE), and counter electrode (CE). The WE contain electro-active materials, the commonly used RE is Ag/AgCl wire saturated in 3 M KCl, and the used CE is a platinum wire (**Figure 2.12**). To study ion transport in a device, RE and CE are often connected together. Various electrochemical techniques used for analysis are discussed below.

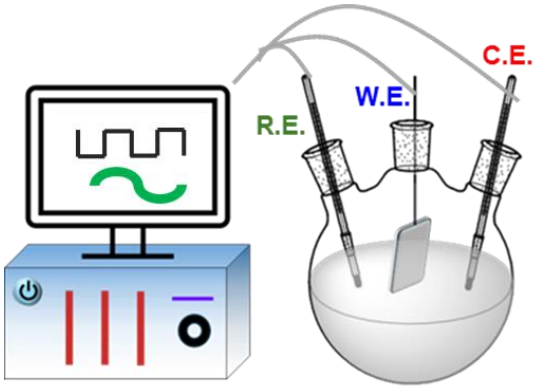

Figure 2.12: The schematic of the electrochemical workstation having three electrodes.

Model Used: Metrohm-Multi Autolab M204 potentiostats

2.4.7.1 Cyclic Voltammetry

Cyclic voltammetry (CV) applies the potential in a linear, cyclic manner using a three-electrode setup, sweeping first from V_1 to V_2 (cathodic path)

and then back from $V_2$to V_1(anodic path)[66]. This allows simultaneous evaluation of both oxidation and reduction behaviors within a single potential window. The shape and area of the CV curve provide insights into charge storage capacity and redox activity. Materials exhibiting reversible redox reactions show peaks in both scan directions, while those with only oxidation or reduction display peaks only in the respective direction.

2.4.7.2 Galvanostatic Charging Discharging

Galvanostatic charge-discharge (GCD) is used to study the charging and discharging behavior of a material under a constant current within a fixed potential window[67]. A constant current, either positive or negative, is applied, and the corresponding potential response is recorded over a set time interval. This technique provides information on the charge storage capability, energy density, and electrochemical stability of the material. The potential–time profile from GCD measurements reveals the charge storage mechanism of the material. A linear increase or decrease in potential indicates EDLC-type behavior, a non-linear trend corresponds to pseudocapacitive behavior, and the presence of a plateau signifies battery-type charge storage.

2.4.7.3 Electrochemical Impedance Spectroscopy

Electrochemical Impedance Spectroscopy[68] (EIS) measures the response of an electrochemical system to an external alternating current over a wide frequency range (10 mHz to 10 kHz). The resulting Nyquist plot provides insights into material properties: the high-frequency region (10 kHz–10 Hz) reflects charge transfer and solution resistance, while the low-frequency region (10 Hz–10 mHz) indicates ion transport behavior. A straight line inclined toward the imaginary axis represents charge storage capability, whereas a semicircle corresponds to diffusion-controlled processes within the material.

2.4.7.4 Chronoamperometry

Chronoamperometry is a technique used to measure the current response over time for a specific applied potential. It involves the occurrence of a faradic reaction at the electrode surface, enabling the flow of current.

2.4.7.5 Chronopotentiometry

Chronopotentiometry applies a constant current to the working electrode while measuring the potential between the working and reference electrodes. It is commonly used to study the charging and discharging behavior of electrodes in batteries and capacitors

2.4.7.6 In-situ Absorbance Spectroscopy

In this technique, electrochemical measurements are performed directly inside the UV-Vis spectrometer cuvette (**Figure 2.13**), allowing simultaneous recording of absorbance versus wavelength and current versus time under an applied bias. The working electrode (WE) is the electrode of interest, while the reference (RE) and counter (CE) electrodes are typically combined. This method is particularly useful for studying the kinetics and real-time behavior of electrode materials.

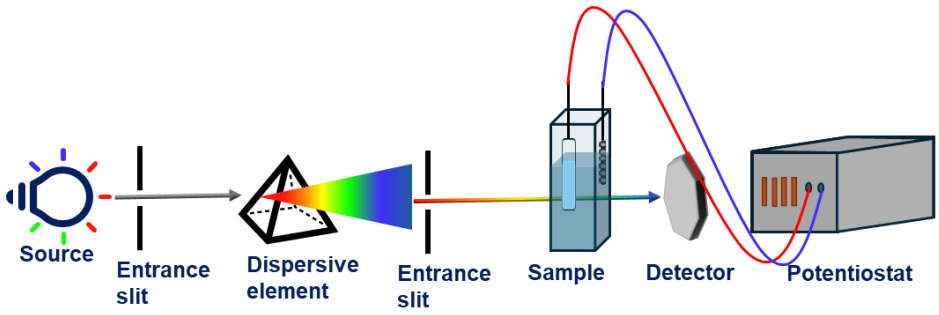

Figure 2.13: Schematic showing In-situ absorbance spectroscopy.

2.5 Methodologies for Device Fabrication

After thorough characterization, the electrodes are fabricated into a fill-fledged device. Typically, two compatible electrochromic (EC) electrodes are selected and assembled as described below. A crucial step is choosing a suitable electrolyte that is compatible with both EC

materials to ensure proper device functionality. The electrolyte incorporated in this work is in semi-solid gel which acts as cushion and holds the electrodes together while enabling ion transport.

Gel Electrolyte: A 5 wt.% PEO solution in acetonitrile was stirred with heating for 5-6 hours, followed by the addition of 0.1 M $LiClO_4$ in a 1:1 ratio (PEO: electrolyte). The mixture was vortexed thoroughly to obtain a thick, homogeneous gel electrolyte.

2.5.1 ECD Assembly Using Flip-Chip Method

The fabricated electrodes are assembled using the following methods.

2.5.1.1 Flexible ECD (*Flex-ECD*)

The electrodes fabricated as described in Sections 2.3.2 and 2.3.3 were assembled to construct the *flex-ECD*. Both electrodes were attached using double-sided tape to hold the PET substrates together, forming the complete *flex-ECD*. The step-by-step process is shown in **Figure 2.14.**

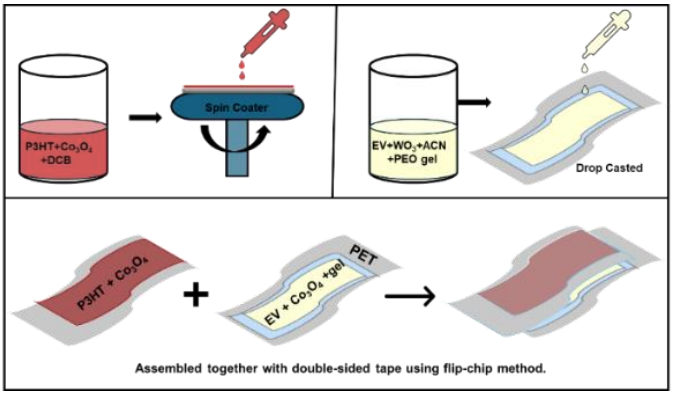

Figure 2.14: Schematic of step-by-step process for the fabrication of device.

2.5.1.2 Flexible NIR-cutting ECD (*flex-NIR cutting- ECD*)

The prepared electrodes as mentioned in **Section 2.3.1 and 2.3.4** were joined together using Flip-chip method to get a ***flex-NIR cutting- ECD***

2.5.1.3 MXene Doped Electrochromic Supercapacitor Device (M-doped ESD)

Both the prepared electrode in **sections 2.3.1** and **2.3.5** were joined together using Flip-chip method to get a M-doped ESD (**Figure 2.15**).

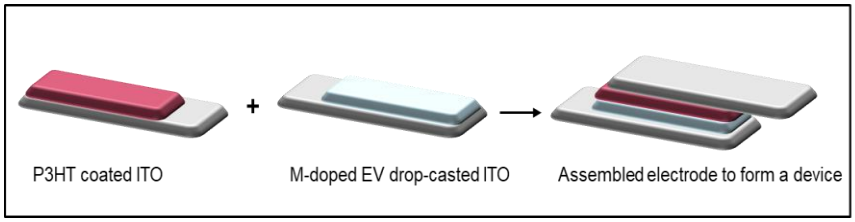

Figure 2.15: Schematic for the fabrication of electrode and device.

2.5.1.4 Perovskite $CoTiO_3$-Doped Electrochromic Supercapacitor device (ESCD)

The prepared CTO-P3HT electrode (**Section 2.3.6**) and WO_3 electrode (**Section 2.3.7**) were assembled together by sandwiching the gel electrolyte (1M $LiClO_4$) in between them to fabricate the ESCD using flip chip method.

2.5.2 Supercapacitor Device (SCD) Assembly

For the fabrication of asymmetric supercapacitor devices, the fabricated electrodes of Gr-NiO and GO-NiO (**Section 2.3.9**) were used as active electrodes. For the counter electrode, a solution of AC in DI water was prepared (10mg/ml). Approximately 100 µl of the AC solution was drop-casted over a cleaned FTO substrate and was left to dry in an oven for 8 hours at 60 °C. Afterwards, both the prepared electrodes, namely the Gr-NiO, GO-NiO electrodes and the prepared AC electrode, were sandwiched together with the help of parafilm, keeping a Whatman filter paper soaked in 2M KOH as a separator between. The prepared asymmetric supercapacitor devices (Gr-NiO-SCD and GO-NiO-SCD) were used as prepared.

2.6 About Software: Osram Sylvania

The CIE-defined color space quantitatively relates visible wavelengths to colors perceived by the human eye, using RGB or LMS coordinates as mathematical constructs. **Figure 2.16** shows a conventional CIE diagram, where combining two colors results in a third coordinate. Specialized software was used to analyze these color coordinates for the electrochromic devices (ECDs).

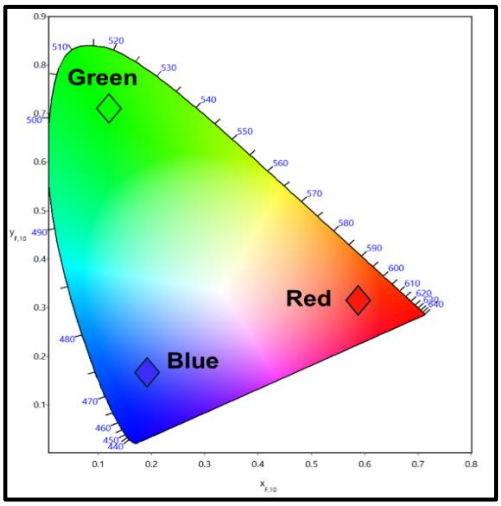

Figure 2.16: A typical CIE chart wherein various colors has been assigned to certain specific co-ordinates.

2.7 Computational Details

Density Functional Theory (DFT) calculates vibrational, magnetic, and electronic properties of atoms, crystals, or many-body systems using electron density instead of the complex many-body wavefunction. This reduces the 3N variables of the Schrödinger equation to just three spatial coordinates. DFT employs various approximations such as Local Density Approximation (LDA), Generalized Gradient Approximation (GGA), Meta-GGA, Hyper-GGA, and Adiabatic Local Density Approximation (ALDA) to model the system efficiently.

Computation details for NiO, Gr, GO, Gr-NiO and GO-NiO.

The theoretical density functional theory (DFT) calculation for the NiO, Gr, GO, Gr-NiO, and GO-NiO, such as optimization of molecular geometries, was carried out using the B3LYP function and 3-21G basis set as implemented in the Gauss 5.0™ software. Geometrical optimizations were performed without imposing any molecular symmetry constraints. For all the computational details, tight convergence criteria with a quadratically convergent SCF method have been used. The molecular electrostatic potential plots of Gr, GO, Gr-NiO, and GO-NiO molecules were plotted to deconvolute the electroactive sites.

Chapter 3

Highly Flexible asymmetric all-organic multifunctional ECDs

Flexible electrochromic (EC) devices have emerged as promising components in wearable electronics, offering dynamic color control and thermal regulation. Several approaches have been made to enhance the performance of all-organic ECDs based on P3HT and ethyl viologen (EV). This chapter highlights the incorporation of nanomaterials, including metal oxides and chalcogenide mixtures, significantly enhancing EC performance while also introducing effective heat-shielding properties to the ECD. The ECDs show fast, reversible color switching across visible and NIR regions with excellent flexibility. Structural analysis through FESEM, XRD, and Raman confirms successful formation of nanomaterials, while in-situ UV–Vis spectroscopy demonstrates the suitability of ECD for real-life smart window applications. This work has been published in international journals[1,2].

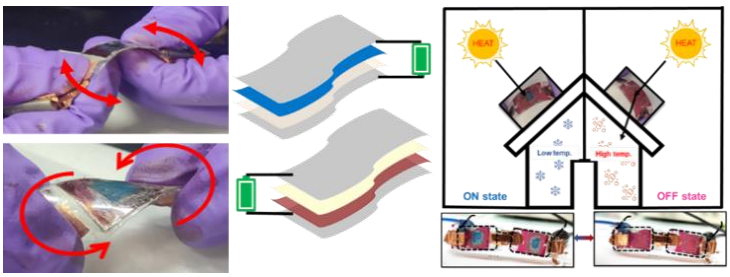

[1] Sahu. B. et al., Mater. Today Electron. 2024, 7, 100082.
[2] Sahu. B. et al., ACS Appl. Opt. Mater. 2024, 2, 10, 2128–2136.

3.1 Complementary Nature of P3HT and Viologen

As discussed in earlier chapters, electrochromism refers to the reversible change in color or transparency of an electrochromic material caused by redox reactions under an applied electric bias. A wide range of electrochromic (EC) materials have been explored and are generally classified as n-type (cathodic) or p-type (anodic) based on their redox behavior in device applications. Among them, poly(3-hexylthiophene) (P3HT) has emerged as an excellent p-type material, while viologen derivatives serve as efficient n-type counterparts. These materials exhibit complementary redox properties and display distinct, complementary color changes upon the application of an electric bias. Here, the P3HT (**Scheme 3.1a**) and Viologen derivative particularly ethyl viologen diperchlorate (**Scheme 3.1b**) have been studied for their EC performances.

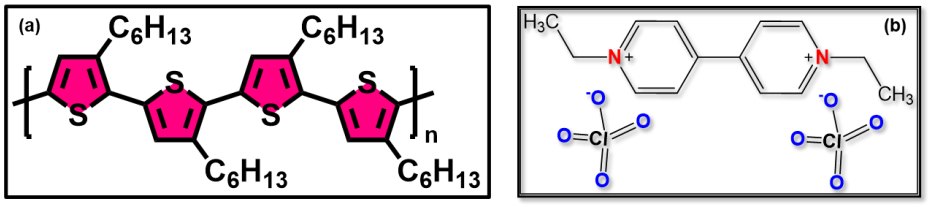

Scheme 3.1: (a) The P3HT and (b) Ethyl viologen diperchlorate molecules.

Thiophenes are inherently p-type materials that exhibit color changes under positive bias. The pristine color of poly(3-hexylthiophene) (P3HT) is magenta, which gradually turns transparent upon applying a small positive bias due to the formation of the polaronic state. With a further increase in bias, the material undergoes another transition from transparent to blue, corresponding to the formation of the bipolaronic state. In contrast, ethyl viologen diperchlorate (EV) exhibits n-type behavior, showing color changes only under negative potentials. The

native EV^{2+} species is colorless or transparent, but upon the application of a small negative bias, it is reduced to the radical cation ($EV^{+\cdot}$) state, displaying a dark blue color. When a device is fabricated using only P3HT and EV, its initial appearance is magenta owing to the intrinsic color of P3HT and the transparent nature of EV^{2+}. Upon applying a small bias, the device color changes to dark blue because of the formation of the bipolaronic state in P3HT and the radical cation state ($EV^{+\cdot}$) in EV. By carefully controlling the applied bias, an intermediate transparent state of P3HT can also be achieved.

3.2 Highly Bendable and Twistable Property of Metal Oxide Doped All-Organic ECDs

Nanomaterials have emerged as versatile components in modern science and technology, finding extensive applications in catalysis[69], sensing[70], energy storage[71], and optoelectronic devices[72,73] due to their large surface area, tunable electronic properties, and high reactivity. In electrochromic device[74,75] (ECD), nanostructured materials play a key role in enhancing ion diffusion, charge transfer, and optical response of the materials and devices. Among them, tungsten trioxide[43] (WO_3) and cobalt oxide[76] (Co_3O_4) have gained particular interest because of their excellent electrochemical activity, optical transparency, and mechanical stability. WO_3, a well-known n-type semiconductor, exhibits high stability with reversible redox behavior, while Co_3O_4, a p-type semiconductor, promotes fast charge transport and structural durability.

Integrating these oxides into organic electrochromic systems enhances overall performance by uniting the mechanical flexibility of polymers with the structural stability and electrochemical strength of inorganic materials[47,77] along with additional property of heat filter[78]. In this context, P3HT and ethyl viologen[79] (EV) serve as complementary

redox-active polymers ideal for metal oxide doping. Here, WO_3 and Co_3O_4 are incorporated into the P3HT–EV-based all-organic ECD, effectively enhancing charge transfer and mechanical endurance, leading to a highly efficient, twistable, and bendable electrochromic device suitable for next-generation flexible applications[80–82].

3.2.1 Structural Characterization of Metal Oxides

Prior to the device formation and electrochromic study of fabricated flexible-ECD (*flex-ECD*), the synthesized dopant materials (**Section 2.2.1 and 2.2.2**), namely WO_3 and Co_3O_4 nanomaterials have been characterized using different techniques (**Figure 3.1**). The size of dopant material plays vital role in influencing the performance of an ECD. Preferably dopant material with nanosized dimensions with high surface porosity shows increase in electrochromic performance. The synthesized WO_3 and Co_3O_4, has been characterized by using field emission scanning electron microscopy (FESEM) to study its morphological and structural properties. The FESEM micrograph shows the formation of flakes-like structure of WO_3 powder (**Figure 3.1a**) evenly distributed all over the surface making the surface highly porosity. At the same time, the FESEM image of Co_3O_4 (**Figure 3.1b**) shows high surface porosity with nano-sized particle.

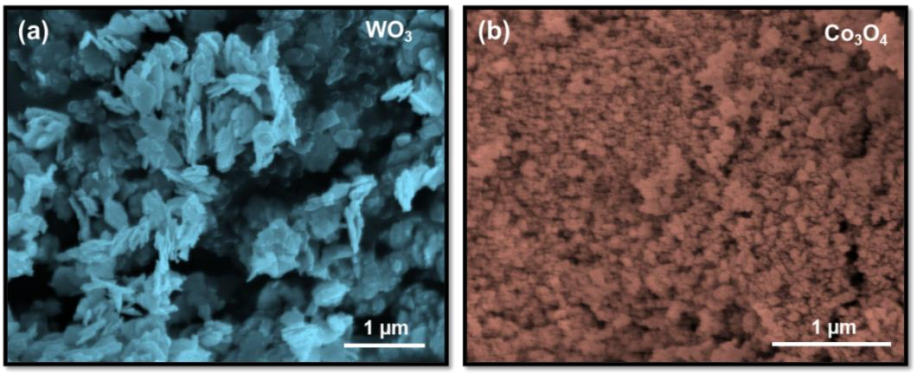

Figure 3.1: The surface morphology of the metal oxides nanomaterials (a) WO_3 and Co_3O_4 (b).

Further, the XRD plot was recorded to examine the crystalline structure, phase purity, and crystallite size of the synthesized dopant metal oxides. The XRD graph (**Figure 3.2a**) shows the crystalline nature of WO_3 powder having monoclinic crystal structure. Diffraction peaks at 2θ values of 23.1˚, 23.6˚, 24.3˚, 26.6˚, 28.7˚, 33.4˚, 34.1˚, 41.6˚, 47˚, 48.1˚, 50.1˚, 51.2˚, 54.5˚ and 55.9˚ corresponds to the (002), (020), (200), (120), (112), (202), (122), (222), (004), (040), (140), (114), (024) and (420) crystal phases of monoclinic structured WO_3 powder (JCPDS card No. 43-1035)[49,83]. Whereas, the diffraction peak from Co_3O_4 were observed at 31.4˚, 36.8˚, 44.7˚, 59.3˚ and 65.2˚ corresponds to (220), (311), (400), (511) and (440) indicates the cubic spinel structure of Co_3O_4 (JCPDS card file No. 43-1003)[84] (**Figure 3.2b**). The absence of any additional peaks in the XRD patterns confirms the high phase purity of both dopant materials.

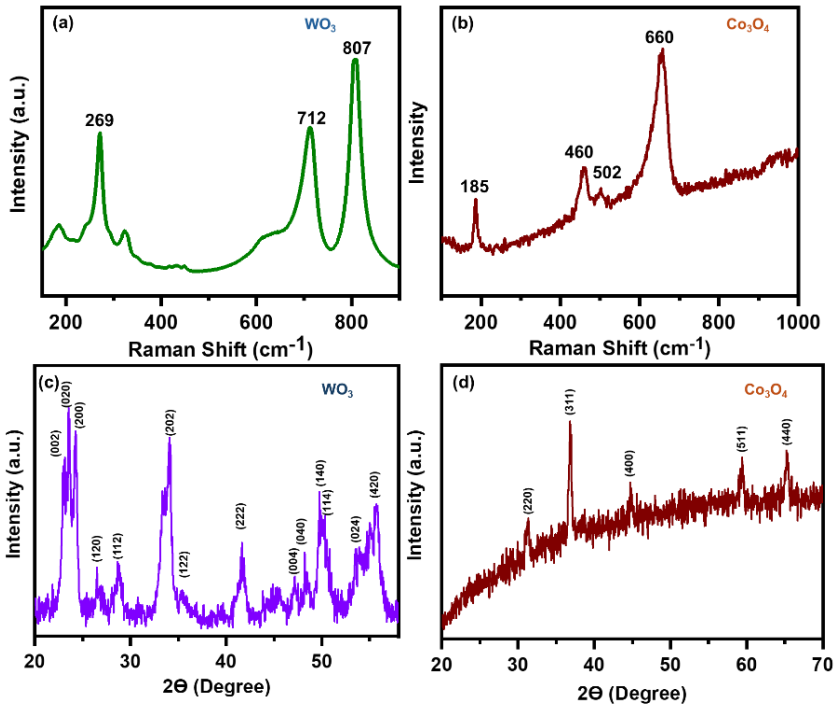

Figure 3.2: The Raman spectrum and XRD plots of the metal oxides nanomaterials (a,c) WO_3 and Co_3O_4 (b,d).

To further quantify the crystallite size of WO_3 and Co_3O_4 nanomaterials, the Debye–Scherrer equation was employed using the Eq. 3.1.

$$D = \frac{0.9\lambda}{\beta \, Cos \, \theta}, \quad (3.1)$$

where D is the average crystallite size, λ is the wavelength of X-ray source, β is the full width at half maxima and θ is the diffraction angle. The average size of Co_3O_4 nanomaterial was calculated to be 28 nm in diameter and WO_3 flakes have average thickness of 10 nm. These nanoscale dimensions, in combination with the high surface porosity observed in FESEM images, provide a large active surface area that facilitates efficient ion intercalation and electron transport, thereby enhancing the electrochromic performance of the flexible devices.

To further investigate the chemical structure of WO_3 and Co_3O_4 powder, Raman analysis has been done. The Raman spectrum of WO_3 (**Figure 3.2c**) shows three main characteristic peaks at around 270 cm^{-1}, 715 cm^{-1} and 805 cm^{-1} arising due to bending and stretching vibration of O-W-O of the monoclinic phase of WO_3[49,85], respectively, which is in accordance with the XRD pattern of WO_3. The Raman spectrum from Co_3O_4 (**Figure 3.2d**) shows three intense peaks and a weak peak at 185 cm^{-1}, 460 cm^{-1}, 502 cm^{-1} and 660 cm^{-1}. The peaks at around 185cm^{-1}, 460cm^{-1}, 502cm^{-1}, and 660 cm^{-1}, attribute[1] $F_{2g}^{(3)}$,E_g, $F_{2g}^{(2)}$, and A_{1g} symmetry respectively[86]. The Raman spectrum of Co_3O_4 is consistent with the above-mentioned XRD pattern.

3.2.2 Flexible ECD Fabrication.

The well-characterized WO_3 and Co_3O_4 powders the *flex-ECD* has been fabricated using the recipe discussed in the experimental section 2.5.1.1 to obtain a device with generic structure "PET/P3HT+Co_3O_4/EV+WO_3/PET" (**Figure 3.3**). Due to the natural shade of P3HT and the transparent nature of EV, the as-prepared *flex-*

ECD had appeared to be magenta (inset Figure 2b). When an external bias of +1.4V is applied to the device (say ON), such that +1.4V is supplied to the Co_3O_4 doped P3HT electrode gets oxidized by losing extra electrons and changes color to blue because of the bipolaronic condition of P3HT (P3HT - e^- → $P3HT^+$) occurs due to dynamic doping [87,88] (**Figure 3.3**). At the same time, the clear tint of the EV turns blue by accepting the extra electrons donated by the complementary Co_3O_4 doped P3HT electrode as the negative bias of -1.4V is getting supplied to the WO_3 doped EV electrode. The transformation of the EV^{2+} ion into its $EV^{\cdot+}$ radical cation is what causes EV to go from transparent to blue ($EV^{2+} + e^-$ → $EV^{\cdot+}$). Hence, under +1.4V bias, the device's overall color was seen to be blue (**Figure 3.3**). The incorporation of Co_3O_4 in P3HT and WO3 in EV helps in the easy access of electron from one electrode to another, improving the performance of *flex-ECD*. On reversing the potential (-1.4V, say OFF), the device returns to its initial state (magenta color) by reverse redox reaction occurring on the electrode, showing the excellent reversibility of *flex-ECD*.

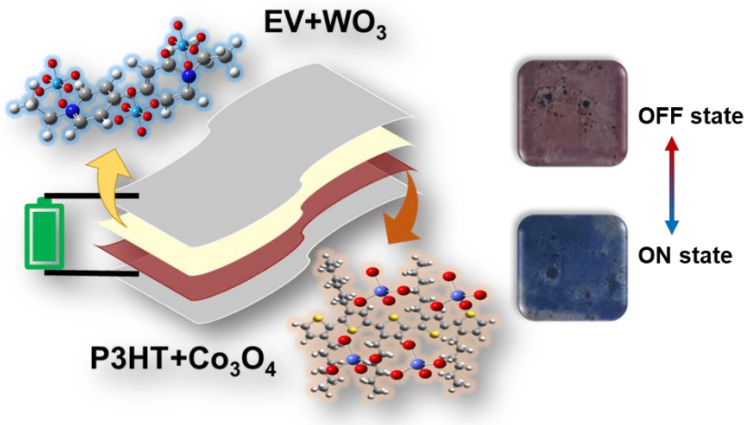

Figure 3.3: The schematic of the fabricated *flex-ECD* with original device color in ON and OFF state.

3.2.3 Optical Measurement of the Initial *flex-ECD.*

To better understand the aforementioned color switching, change in optical spectra has been studied 0V and ±1.4V using UV-Visible spectroscopy (**Figure 3.4a**). Initially, when the *flex-ECD* is unbiased (0V) absorbs maximum green color wavelength of visible spectrum and transmitting the two remaining primary colors (red and blue) giving the magenta color to the device. On application of 1.4V, the whole absorption spectra shift towards lower energy and starts absorbing red-green color with low absorption of blue color, giving the same color to the device. Further, on reversing the polarity (-1.4V), it retraces the initial unbiased curve giving the original magenta color to the *flex-ECD* confirms the color reversal on reversing the bias. This reversible change in the absorbance spectra demonstrates the excellent electrochromic reversibility of the *flex-ECD*, which is a crucial parameter for practical applications such as flexible displays and wearable electronics.

The above-mentioned color modulation can also be understood from the bias-dependent transmittance variation response of the device (**Figure 3.4b**). The *flex-ECD* shows maximum change in transmittance value, called as color contrast at 515 nm in visible spectrum, which can be evaluated from Eq. 1.1. The color contrast of 50 % with change in transmittance value ($\Delta T\% = T_{(1.4V)} - T_{(-1.4V)}$) of 7.34 % has been observed under an external bias of ±1.4 V (Figure 3a) at 515 nm. The high color contrast is due to the complementary nature of the two electrodes (Co_3O_4 doped P3HT & WO_3 doped EV). In addition to this, the maximum change in transmittance (ΔT) value was also observed at around 665nm which is near infrared region (NIR). The observed value of ΔT is ∼29 % (**Figure 3.4b**). The high ΔT value of the device in NIR region make the device to have a possible applicant as heat filter because in ON state the device is highly absorbing NIR region. This dual functionality-visible

color modulation and NIR absorption, enhances the practical scope of the device for smart window with heat filtering capacity.

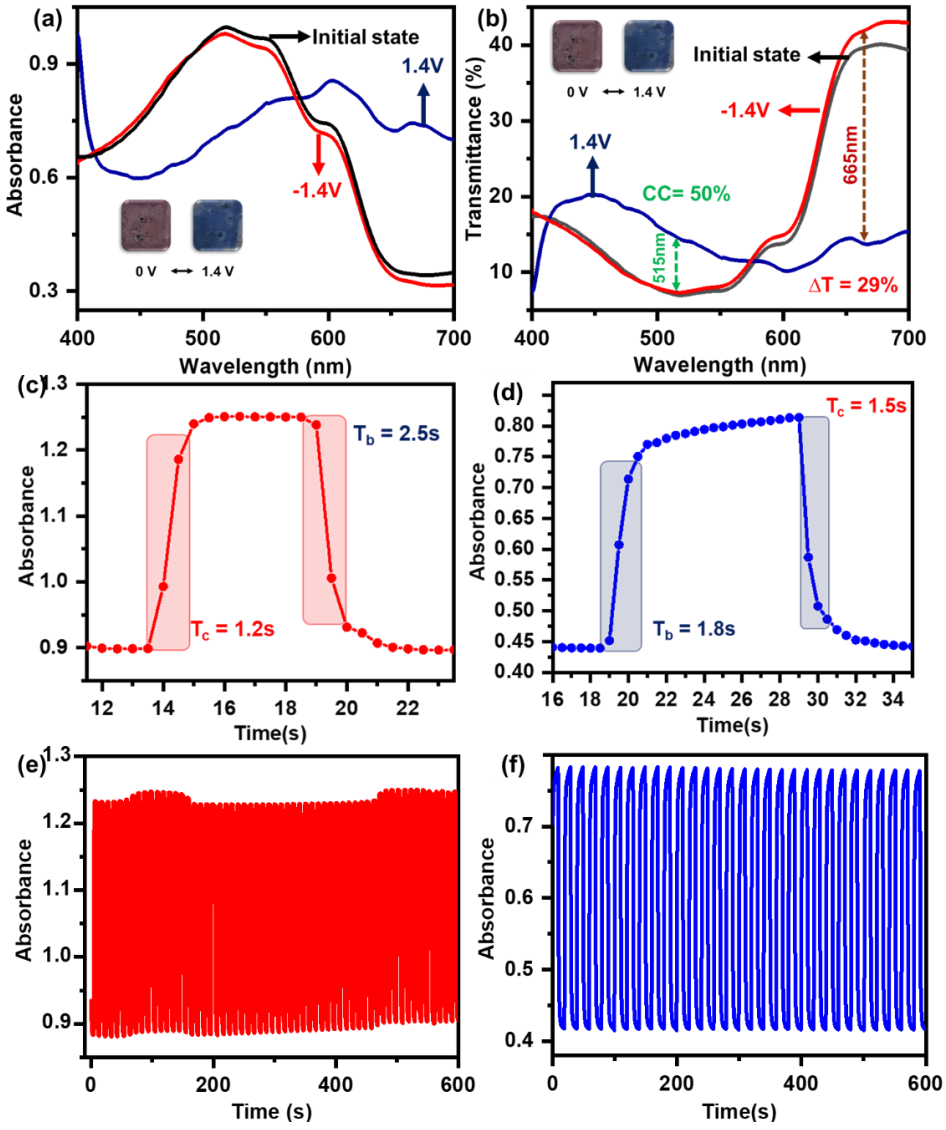

Figure 3.4: Performance of the initially fabricated *flex-ECD* (a) in-situ bias dependent absorbance, (b) in-situ bias dependent transmittance spectra, (c) Single switching cycle at 515 nm, (d) at 665 nm and (e) the cyclic stability at 515 nm and (f) 665 nm.

To study the switching kinematics of the device, how fast the device is changing color from blue to magenta (colored state) and from magenta to blue (bleached state), a continuous square pulse of ±1.4V was applied and corresponding absorbance spectra was recorded. The time required for the *flex-ECD* to switch from blue to magenta (coloration time) (90% change in the absorbance value) is ∼ 1.2 s and to switch from magenta to blue (bleaching time) is ∼ 2.5 s (**Figure 3.4c**). The fast-switching speed with few seconds of switching time can be understood as the doped Co_3O_4 (in P3HT) and WO_3 (in EV) helping the device to switch fast between the two colors by donating/accepting the excess electrons rapidly. The high value of switching speed also indicates the charge is getting stored on the surface of electrode under external bias. Also, the bleaching time of ∼ 1.8s and coloration time of ∼1.5s has been observed for *flex-ECD* at 665nm (**Figure 3.4d**). While studying the electrochromic performance of an electrochromic device, switching stability/cyclability is another crucial aspect for the application purpose as it is used to estimate how fast the *flex- ECD* can switch between the two colors and for how many cycles with little to no stability compromise. The stability of the *flex-ECD* has been checked at 515 nm by applying a continuous square pulse of ±1.4V with 5s of each polarity for 120 switching's (600 s) (**Figure 3.4e**). The flex-ECD shows excellent stability with almost constant change in the absorbance spectra making the device a potential candidate for application purpose. The cyclic stability at 665 nm (**Figure 3.4f**), also shows an excellent performance of the *flex-ECD* by applying the same square pulse of ±1.4V with 10s of each polarity for 30 switching's. The remarkable stability of device could be caused by the doping of Co_3O_4 in P3HT and WO_3 in EV, as it acts as a mediator for the transfer of electron from one electrode to another.

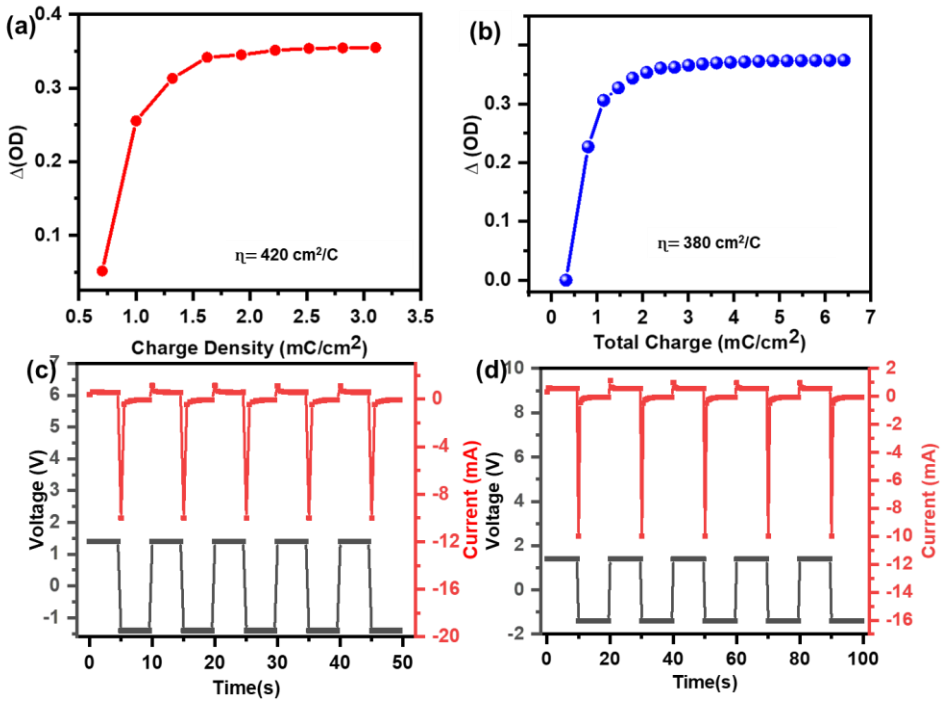

Figure 3.5: (a,b)The ΔOD vs charge density graph for calculating coloration efficiency at 515 nm and 665 nm of the initially fabricated *flex-ECD* with corresponding current vs time vs voltage graph for 515nm and 665 nm (c,d).

Further, the critical factor for evaluating the device's performance is coloration efficiency (η_{ce}), was calculated using Eq. 1.2. The evaluated η_{ce} of the device was found to be 420 cm^2/C for visible region (515 nm) (**Figure 3.5a**) and 380 cm^2/C for NIR region (665 nm) (**Figure 3.5b**). The high coloration efficiency of device is due to the doping of WO_3 and Co_3O_4 nanomaterials to respective electrode which facilitates the easy charge transfer. And the charge density Q has been calculated from the current density response on the application of an external pulse train of ±1.4V (**Figure 3.5c**, @ 515nm & **Figure 3.5d**, @ 665nm)Such high η_{ce} values highlight the effectiveness of incorporating WO_3 and Co_3O_4 nanomaterials into the respective electrodes, as the doping significantly

enhances charge transfer kinetics and optimizes ion diffusion pathways. One more essential parameter is the reversibility of the electrochromic device, which is the defined as the ratio of de-intercalated charge density to the intercalated charge density. The reversibility (R) of the device has been calculated using the Eq. 3.2[89],

$$R = \frac{Q_{de-in}}{Q_{in}} \times 100\% \ , \qquad (3.2)$$

where, Q_{de-in} and Q_{in} denotes the density of charge de-intercalated and intercalated. The effective ion extraction and insertion indicate high electrochemical reversibility. The determined reversibility of the flex-ECD was 56% and 99% at 515 nm and 665 nm. The flexible device shows excellent reversibility at 665 nm. This clearly demonstrates that the flexible device exhibits excellent reversibility in the NIR range, ensuring stable and repeatable optical modulation during multiple switching cycles.

3.2.4 Optical Measurement of the *b-flex-ECD* After 20 Bending.

Afterward, to study the flexibility of the same flex-ECD in terms of bending, it has been bent upward and downward 20 times under ambient condition and left for 60 s. The corresponding bending angle and frequency were calculated and presented in **Figure 3.8a**, and importantly, no device failure was observed during the bending process.

After bending, the device was named as b-flex-ECD, the in-situ bias dependent transmittance spectra have been recorded initially without applying voltage and after applying ±1.4V (inset: **Figure 3.6**). The transmittance curve shows the typical initial behaviour with little decrease in the transmittance value. The little change in transmittance value is due to the bending of the b-flex-ECD. The maximum change in

transmittance spectra was again observed at 515 nm (visible region) and 665 nm for the b-flex-ECD (**Figure 3.6b**).

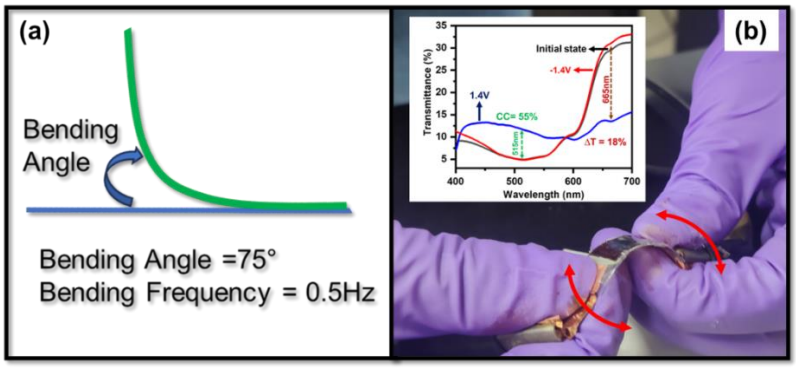

Figure 3.6: (a) The bending angle and bending frequency of the *b-flex-ECD* under ambient condition and (b) Photograph showing the bending of the device along with in-situ bias dependent transmittance spectra (inset) of the *b-flex-ECD* after bending 20 times.

To calculate the greatest spectrum, change at a specific wavelength, the color contrast was calculated using Eq. 1.1. The color contrast of ∼55 % was observed with change in transmittance value of (ΔT%) 6.76 %. The increase in color contrast at 515nm can be understood as due to the bending of the b-flex-ECD, the whole transmittance spectrum has been shifted downward. The value of T_n also became smaller due to the bending; hence the value of color contrast increases due to the lower value in the denominator. Also, the decrease in optical modulation is due to the bending moment. The ΔT value at 665nm has been decreased due to the bending moment of b-flex-ECD. Slight change or no change in absorbance spectra of b-flex-ECD shows its suitability as flexible ECD. This highlights its potential applicability as a mechanically robust and flexible ECD.

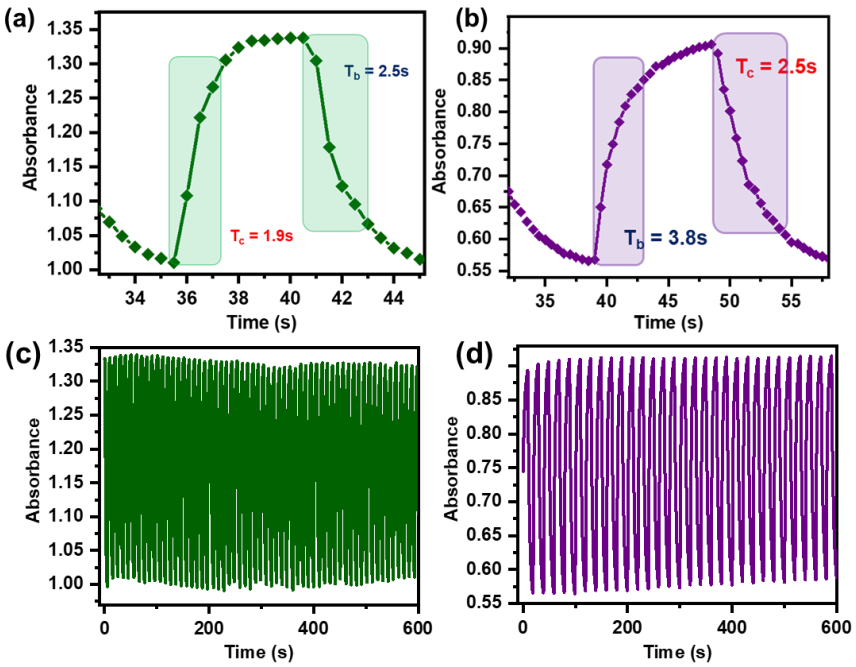

Figure 3.7: Single switching cycle at (a) 515 nm and (b) 665 nm and the cyclic stability at 515 nm and 665 nm of the *b-flex-ECD* (c,d).

To study the switching dynamics of b-flex-ECD, switching time was calculated at 515 nm and 665 nm by applying a square pulse of ±1.4V with 5s and 10s of each polarity, respectively and was calculated at 90% of maximum change in absorption. The coloration time of ∼1.9 s and bleaching time of ∼2.5 s has been observed for 515 nm wavelength (**Figure 3.7a**). The coloration time has been increased to ∼0.7s whereas the bleaching time remains unchanged (2.5s) after bending. The bleaching and coloration time at 665nm have also been calculated (**Figure 3.7b**). It was found that the bleaching time was increased by 2s taking ∼3.8s to switch from magenta to blue. The coloration time was increased by 1s taking ∼2.5s to switch from blue to magenta. The increment in the switching time of post-bending b-flex-ECD is likely due to the bending moment of the device showing little deviation from the originally prepared flex-ECD. Further, the cyclic stability of the b-flex-

ECD was checked, to ensure the performance of device for real life applications. The stability of the b-flex-ECD was examined at 515 nm by applying multiple square pulse of ±1.4V for 60 cycles (600 s) with 5s of each polarity (**Figure 3.7c**). The b-flex-ECD shows great stability with less compromise in the performance. The stability test was also performed at 665 nm by applying multiple pulse train of ±1.4V for 30 cycles (600s), showing high stability with almost no compromise in the performance (**Figure 3.7d**). It is evident from above results that the b-flex-ECD shows high performance with a little increment in switching and high performance in terms of efficiency and stability after bending for 20 times.

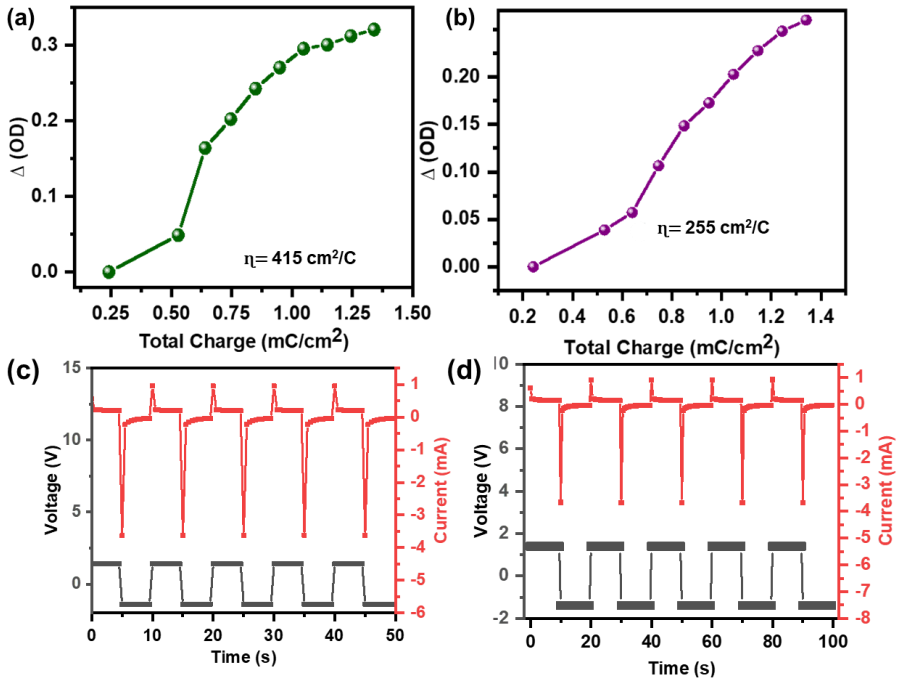

Figure 3.8: (a,b) The ΔOD vs charge density graph for calculating coloration efficiency at 515 nm and 665 nm of the *b-flex-ECD* with corresponding current vs time vs voltage graph for 515nm and 665 nm (c,d).

To study the effective performance of b-flex-ECD, the coloration efficiency has been calculated using Eq. 1.2. It was found that the coloration efficiency has not changed much after bending for 20 times giving 415 cm^2/C efficiency (**Figure 3.8a**). The unchanged efficiency is owing to a little to no change in optical density (OD) and charge flowing through the b-flex-ECD, proves its suitability as flexible ECD. To calculate the efficiency at 665 nm, a pulse train of ±1.4V with 10s of each polarity was provides to the device and corresponding absorbance spectra was recorded. The efficiency of 255 cm^2/C at 665nm was observed (**Figure 3.8b**). The Q value for 515nm and 665 nm were evaluated by current response of device under a pulse train of ±1.4V with 5s (**Figure 3.8c**) and 10s (**Figure 3.8d**) of each polarity respectively. The decrease in efficiency in NIR region is likely due to the observed decrease in OD from 29 % to 18 %. The electrochemical reversibility was found to be 67% and & 75% for 515 nm and 665 nm evaluated using the Eq. 3.2 showing high insertion and extraction of ions within the device. The fabricated b-flex-ECD with such appreciable properties make the device most efficient for application purpose with bending moments.

3.2.5 Optical Measurement of the *tb-Flex-ECD* After 20 Twisting.

Furthermore, the same b-flex-ECD was then used to study the effect of twisting moments on the device performance. The b-flex-ECD was twisted for 20 times without device failure under ambient conditions (**Figure 3.9a**) and left idle for 60 s and the post twisting device (say *tb-flex-ECD*) was tested for its performance. The twisting angle and frequency has been shown in **Figure 3.9a**.

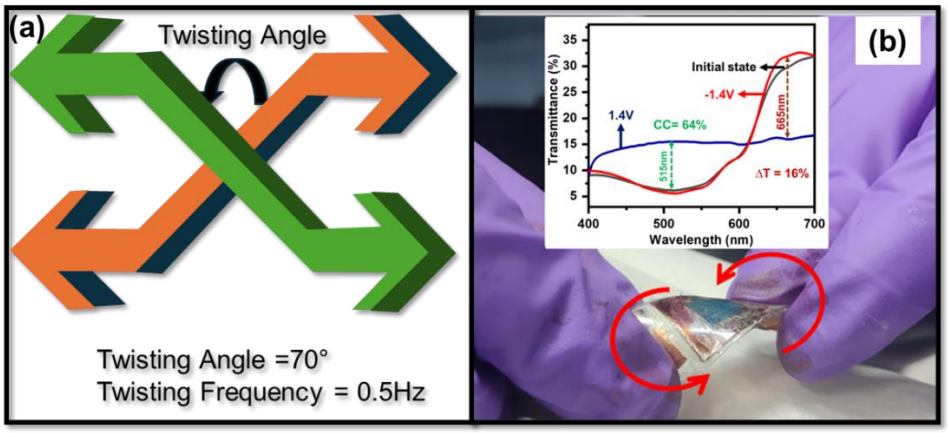

Figure 3.9: (a) The twisting angle and twisting frequency of the *tb-flex-ECD* under ambient condition and (b) Photograph showing the bending of the device along with in-situ bias dependent transmittance spectra (inset) of the *tb-flex-ECD* after twisting 20 times.

The bias dependant transmittance spectra were recorded for the tb-flex-ECD with no bias (0V) at first and then by the application of ±1.4V (inset: **Figure 3.9b**). The transmittance spectra of the device were not much changed after twisting with little upward shift in the ON state. In the transmittance spectra of tb-flex-ECD, the maximum change in transmittance spectra was observed at 515 nm and 665 nm. At 515nm, the tb-flex-ECD shows high color contrast (calculated using Eq. 1.1) of 64 % in visible region after the twisting. The color contrast was increased by ∼10 % after twisting with respect to the b-flex-ECD. The increment in color contrast can understood as the difference in ON and OFF state ($T_n - T_f$) of the device is more as compared to b-flex-ECD, hence increment in optical modulation was observed having value 10 %. The change in transmittance (ΔT) at 665nm was observed to be 16 %, with a little decrease in the value. The decrease in the ΔT value at 665 nm is due to the twisting of the device.

The switching time was determined for both the wavelengths by the application of square pulse of ±1.4V and corresponding absorbance spectra was recorded. At 515 nm (**Figure 3.10a**), the tb-flex-ECD takes 2.9 s to switch from blue to magenta (coloration) and 2.7 s to switch from magenta to blue (bleaching). In comparison to the b-flex-ECD, the tb-flex-ECD is taking 1s of extra time to go to the colored state and 0.2 s more time to go to bleached state. The bleaching and coloration time at 665nm was found to be 4.4 s and 3.9 s (**Figure 3.10b**). An increase of 0.6s and 1.4s was observed after twisting the b-flex-ECD. The switching time was increased by few seconds after bending and twisting moment of the flex-ECD at 515 nm and 665 nm without much compromise in contrast.

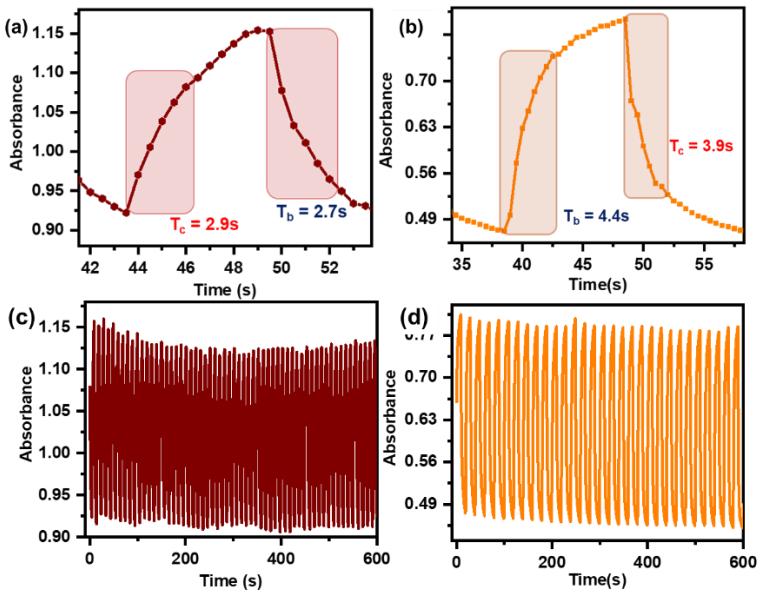

Figure 3.10: (a,b) Single switching cycle at 515 nm and 665 nm and the cyclic stability at 515 nm and 665 nm of the *tb-flex-ECD* (c,d).

The switching stability of the device is also a parameter to check its suitability as ECD. To examine the cyclic stability at 515nm and 665nm, a continuous train pulse of ±1.4V was applied with 5s and 10s of each

polarity, respectively and corresponding absorbance spectra was recorded. At 515nm (**Figure 3.10c**), the tb-flex-ECD shows excellent switching stability for 60 cycles (600s). Similarly, the tb-flex-ECD exhibits high stability over 30 cycles (600s) at 665 nm (**Figure 3.10d**) as well.

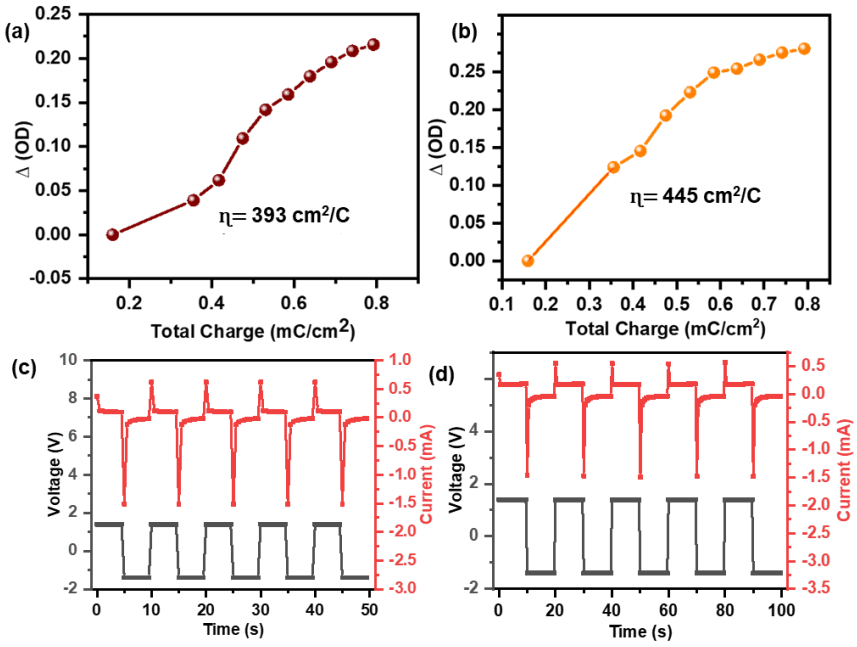

Figure 3.11: (a,b) The ΔOD vs charge density graph for calculating coloration efficiency at 515 nm and 665 nm of the *b-flex-ECD* with corresponding current vs time vs voltage graph for 515nm and 665 nm (c,d).

At 515 nm and 665 nm wavelengths, the device's performance was examined in terms of coloration efficiency. The coloration efficiency of 393 cm^2/C was evaluated for 515 nm wavelength (**Figure 3.11a**) which is of the same order as of the pre-bending and pre-twisting device. The coloration efficiency at 665 nm was observed to be 445 cm^2/C (**Figure 3.11b**). The Q value was calculated using current response of device

under external bias of ± 1.4 V (**Figure 3.11c** for 515 nm) and (**Figure 3.11d** for 665 nm). The sudden increase in the efficiency of the tb-flex-ECD was due to the low charge flow in the device. As the current flowing through the tb-flex-ECD is decreased (**Figure 3.13b**), the charge was also get decreased as Q is the product of current and time. So, as the current value decreases, the charge transfer decreases and hence the efficiency of the device increases as Q value is in the denominator (Eq. 1.2). The electrochemical reversibility was also determined for tb-flex-ECD having value 79% and 66% for 515 nm and 665 nm using Eq. 3.2. The high value of reversibility indicates that after twisting ion diffusion was still high, indicating no device failure.

Table 3.1: Comparison of different flexible devices on basis of different performance parameters.

S. No.	**Device**	**Color Contrast**	**Coloration/ Bleaching time(s)**	**Efficiency (cm^2/C)**	**Reference**
1.	WO_3/ZnO	68.2%	6.2/2.8	80.6	Bi et al.[90]
2.	PANI/EV	41%	0.5/0.8	-	Ghosh et al.[91]
3.	PET/NiO_x	40%	-	67	Lin et al.[92]
4.	PET/V_2O_{5-z}	43.3%	-	102.5	Lin et al.[93]
5.	This work	50%	1.2/2.5	420	Sahu et al.

The overall performance of the device is comparable to the recently reported flexible electrochromic devices, Table 3.1. To compare the performance of the flex-ECD, b-flex-ECD and tb-flex-ECD a comparison table has been made (Table 3.2). These super bending and super twisting moments make the device appropriate for futuristic wearable device.

Table 3.2: Comparison table between the flex-ECD, b-flex-ECD and tb-flex-ECD on basis of their performances.

Device	**Wavelength (nm)**	**CC @ 515nm/ ΔT @ 665nm (%)**	**Switching (s) (tc/tb)**	**Efficiency (cm^2/C)**
Initial ***flex-ECD***	515 665	50 29	1.2/2.5 1.5/1.8	420 380
b-flex-ECD	515 665	55 18	1.9/2.5 2.5/3.8	415 255
tb-flex-ECD	515 665	64 16	2.9/2.7 3.9/4.4	393 445

3.3 Flexible NIR-Cutting Electrochromic Goggles Using Metal Chalcogenides Oxide Mixture.

The global demand for smart, flexible, and energy-efficient electronic devices has driven interest in multifunctional systems[94–96] such as supercapacitors[97,98], batteries[99,100], LEDs[101], solar cells[102], and heat filters[103]. Flexible electrochromic devices[104–106] (ECDs) with additional heat filtering applications are particularly promising as they block near-infrared (NIR) radiation and modulate optical properties with very low energy input. Their bendable and twistable nature makes them suitable for smart windows, energy-efficient buildings, and camouflage applications[80]. However, challenges such as mechanical deformation, low electrochemical performance, and electrolyte leakage limit their stability[105,107,108]. These issues can be mitigated by using suitable substrates like ITO-coated PET and carefully selecting compatible electrochromic materials with complementary redox and color properties[109]. Flexible electrochromic devices (ECDs) based on P3HT and EV are attractive due to their complementary redox behavior, little heat filtering property and easy processability, but they suffer from poor stability and slow switching. These limitations can be addressed by doping with transition metal oxides (TMOs) and chalcogenides (TMCs), which enhance redox activity and electrochemical stability[110]. In particular, a WS_2/WO_3 composite provides both NIR heat shielding and improved stability, while its charge storage facilitates redox reactions in P3HT and EV, enhancing ion flow and switching performance[111]. Such doped systems significantly boost the overall performance of flexible NIR-cutting ECDs, making them suitable for versatile applications[30].

3.3.1. Structural Characterization of WS_2/WO_3 Nanoflakes.

Prior to their incorporation into a flexible electrochromic device (ECD), the synthesized materials (**Experimental Section 2.2.3**) were examined to study their surface morphology, as it provides crucial information about particle size, shape, and distribution, which directly influence the device's electrochemical performance and optical modulation. The FESEM micrograph (**Figure 3.12**) provides a clear view of the morphological characteristics of the hydrothermally synthesized WS_2/WO_3 nanoflakes, showing a thickness of a few nm. The flakes morphology of the WS_2/WO_3 mixture with the presence of open voids will be utilized in easy facilitation of electrons. Also, due to the empty space present, it has the capability to store some charges. These stored charges will help in accelerating the redox reaction and hence improve the performance of flexible ECD.

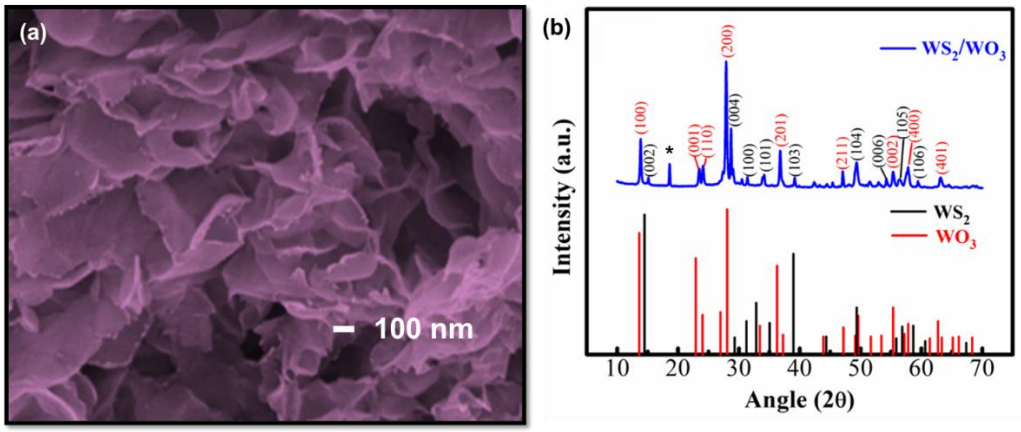

Figure 3.12: (a) The FESEM image and (b) the XRD plot of the WS_2/WO_3 nanoflakes mixture

The XRD analysis of synthesized WS_2/WO_3 nanoflakes provides crucial structural insights (Figure 1a). The peaks were indexed using ICDD database by using inbuilt software in the XRD setup. The card numbers

corresponding to WO_3 and WS_2 were 1004057 and 9012191 respectively. The diffraction peaks at 2θ ~ 13.8 °, 23.6 °, 24.1°, 27.3 °, 36.8 °, 47 °, 57.7 °, 63.1 ° corresponds to the (100), (001), (110), (200), (201), (002), (400) and (401) crystal planes of 2H-WO_3, respectively, whereas the peaks at 2θ ~ 14.9 °, 28.8 °, 31.3 °, 34.1 °, 39.1 °, 49.2 ° and 55.6 ° corresponds to the (002), (004), (100), (102), (103), (105) and (106) planes of hexagonal WS_2 (2H-WS_2)[112,113]. The peak marked by an asterisk (*) corresponds to the (111) plane of orthorhombic $WO_3 \cdot 0.33H_2O$[114]. The presence of both (002) and (100) peaks corresponding to WS_2 and WO_3, respectively in the spectrum served as compelling evidence for the coexistence of WO_3 and WS_2.

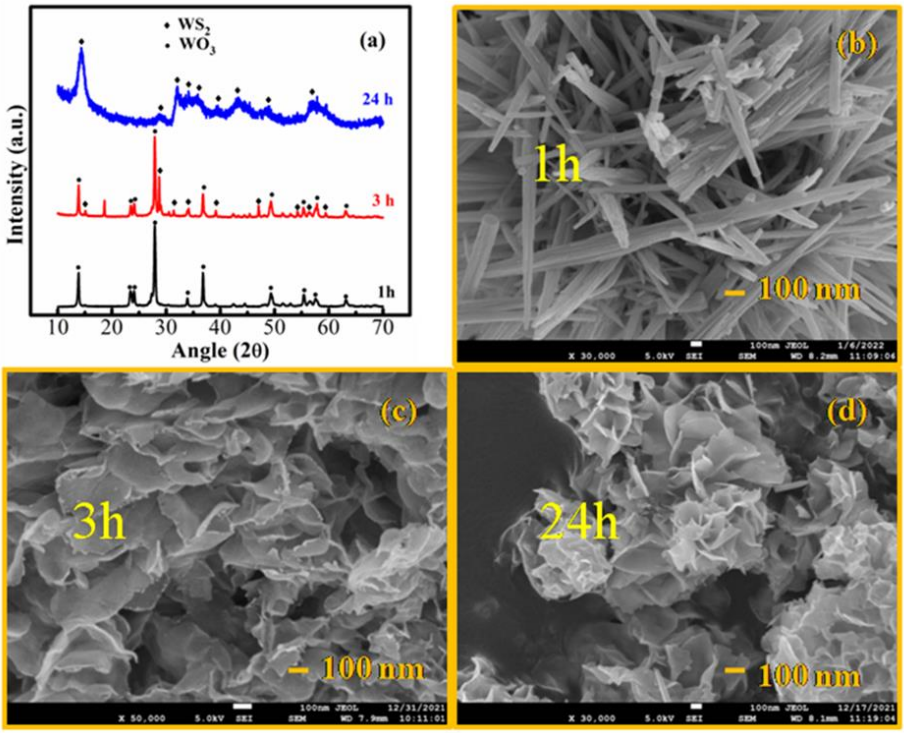

Figure 3.13: (a) XRD pattern and FESEM micrographs of (a) WO_3 nanorods (1h), (c) WS_2/WO_3 nanoflakes (3h) and (d) WS_2 nanoflakes (24h).

Thus, it indicated the formation of mixed phase of WO_3 and WS_2, providing a unique insight into the evolving structure of the materials. Further, the formation of the mixed phase of WS_2/WO_3 can also be understood by the varying reaction time. As the XRD patterns and FESEM micrographs corresponding to reaction times of 1, 3, and 24 h (**Figure 3.13**) reveal the transformation process, WO_3 nanorods (at 1 h) convert into WS_2 nanoflakes (at 24 h), and WS_2/WO_3 nanoflakes (at 3 h) represent a mixed state. Therefore, the flakes synthesized at the 3 h reaction time correspond to a mixed phase of WS_2/WO_3 nanoflakes.

3.3.2 Flexible NIR-Cutting ECD Fabrication.

Following the successful synthesis of WS_2/WO_3 nanoflakes, the fully flexible-NIR cutting-electrochromic device (flex-NIR cutting-ECD) was fabricated in the configuration "PET/P3HT//EV+WS_2/WO_3/PET", as depicted in **Figure 3.14**, using the recipe mentioned in the experimental section 2.5.1.2. The WS_2/WO_3 is n-type material, showing redox activity in negative potential and EV is also an n-type material changing color in negative bias, so the mixture of WS_2/WO_3 was mixed in EV solution to accelerate the redox activity of the EV-P3HT-based ECD.

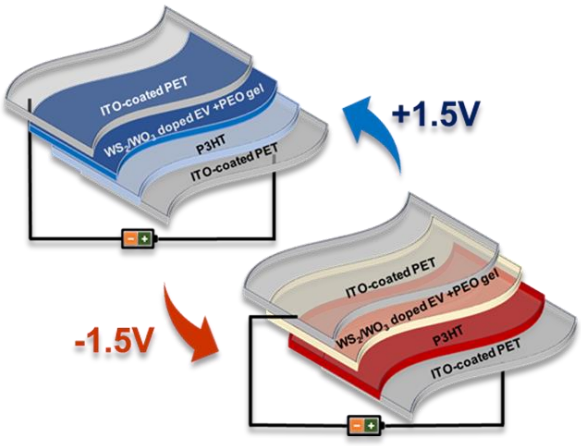

Figure 3.14: Schematic of the flex-NIR cutting-ECD in ON and OFF states.

At first, the as-prepared flex-NIR cutting-ECD appeared magenta in color due to the natural pristine color of P3HT and transparent nature of WS_2/WO_3 mixed EV. When a bias of 1.5 V (with respect to P3HT electrode) is applied to the flex-NIR cutting-ECD (say ON state), the color of the device changes from magenta to blue (**Figure 3.14**) due to the redox reaction between the two electrodes containing redox active materials, which is rejecting the NIR component. The change of color from magenta to blue of flex-NIR cutting-ECD is due to the occurrence of a bipolaronic state of P3HT which is formed after losses of electrons as a result of bias-induced oxidation also known as "dynamic doping". The electron lost by P3HT gets consumed by the WS_2/WO_3 mixed EV layer present in the device, and as a result, the EV changes its color from the transparent state to blue (EV radical to EV radical cation). Hence, the overall color of the flex-NIR cutting-ECD appears as dark blue (colored state). The device has a significantly reversible feature whereby it regains its original magenta color (bleached state) when reverse bias is applied.

3.3.3 Flex-NIR Cutting ECD As Smart Eye-Soothing Goggle Prototype

In the same ON state (the blue color state), the flex-NIR cutting-ECD is highly cutting the NIR region, making it suitable for a heat cutting/filtering application to reduce the use of air conditioning during summer as has been discussed in detailed below. A prototype resembling a goggle has been fabricated by connecting two identical flex-NIR cutting-ECD in series to demonstrate its practical use in the real world (**Figure 3.17**).

In the initial/OFF states, the goggle's glass is magenta in color and has no heat cutting properties (**Figure 3.15a**). The color of the glass changed

to dark blue when exposed to a 3 V external bias (ON state) due to a redox reaction between the two electrodes containing P3HT and WS_2/WO_3 mixed EV (**Figure 3.15b**). As soon as the color of the goggle glass changes, the goggles begin to function as a heat cutting device. The designed prototype goggle offers good reversibility and excellent flexibility.

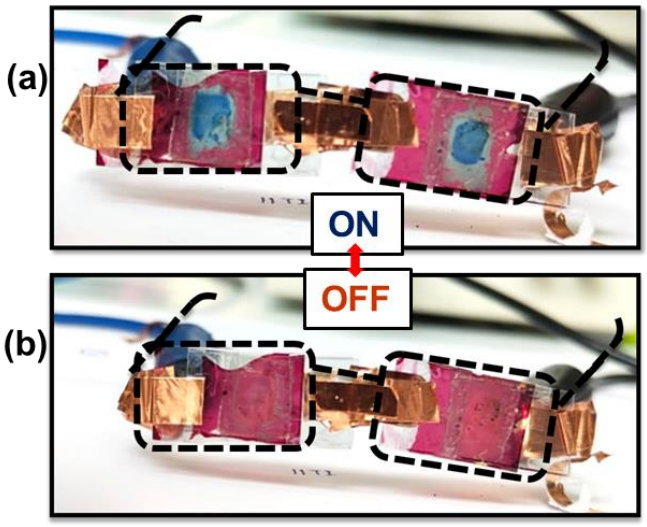

Figure 3.15: Flex-NIR cutting-ECD in goggle form showing two different shades in ON and OFF states

3.3.4 Optical Study of the Flex-NIR Cutting ECD in NIR Region.

The above-mentioned NIR cutting and change in (visible) color between magenta to blue to magenta was further analyzed by recording the in-situ bias-dependent transmittance spectra. The transmittance spectra (Figure 2c) show that without any bias the flex-NIR cutting-ECD was following the black curve, and when +1.5 V (with respect to P3HT electrode) is applied (ON state), the device was following the purple curve. In the ON state of the device, the transmittance value is decreased as the flex-NIR cutting-ECD means it starts cutting the NIR wavelengths thus working as heat filter/NIR filter by decreasing the room's temperature. When the

polarity is reversed (to −1.5 V, with respect to P3HT) the flex-NIR cutting-ECD regains its initial magenta color and starts transmitting more in the NIR region in comparison to the ON state. The actual photographs of the device in ON (NIR cutting) and OFF (initial state) states have been shown in the inset of **Figure 3.16a**.

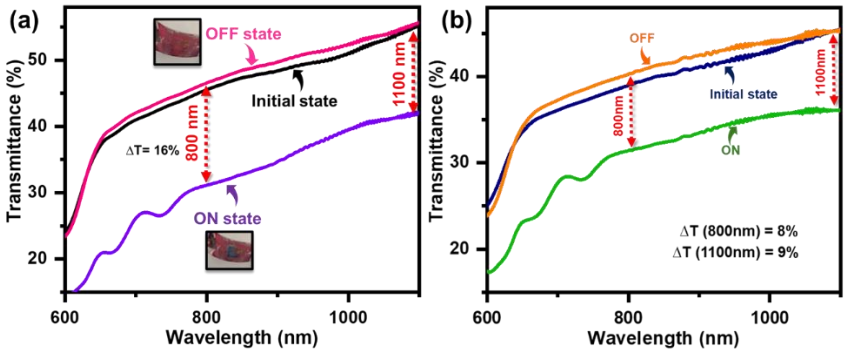

Figure 3.16: (a) In-situ transmittance spectra in NIR region for (a) *flex-NIR-Cutting ECD* and (b) pristine EV-P3HT-based ECD.

The minimum transmittance (or maximum absorbance) was observed at 1100 and 800 nm, with change in transmittance (ΔT) value of 15% and 16%, respectively, between the ON and OFF states, whereas in the case of pristine EV-P3HT-based ECD the observed value of ΔT is only 9% and 8% at 1100 and 800 nm wavelengths, respectively (**Figure 3.16b**). The increased value of Δ*T* for flex-NIR cutting-ECD in both wavelengths is due to the doping of the WS_2/WO_3 mixture, as WO_3 is known as a heat filtering application.

Owing to the flex-NIR cutting-ECD's capacity to filter heat and cause a maximal change in transmittance at 1100 and 800 nm, key performance metrics have been investigated at this NIR wavelength. First, a continuous train of voltage pulse of ±1.5 V with 5 s of each for 1000 s has been given to examine the cyclic stability of the flex-NIR cutting-ECD at 1100 nm (**Figure 3.17a**). The change in absorbance value was

almost constant throughout the stability testing duration. Although little spikes had appeared in between, no change in the difference of absorbance (ΔA = change in absorbance value in ON and OFF states of the device) for 100 cycles was observed, ensuring good stability when used for heat cutting. A similar cyclic stability check was performed at 800 nm (**Figure 3.17b**), which demonstrates that the device is very stable for 100 switching cycles with little to no change in the Δ*A* value. The remarkable stability of the flex-NIR cutting-ECD is attributed to the doping of a highly stable WS_2/WO_3 mixture.

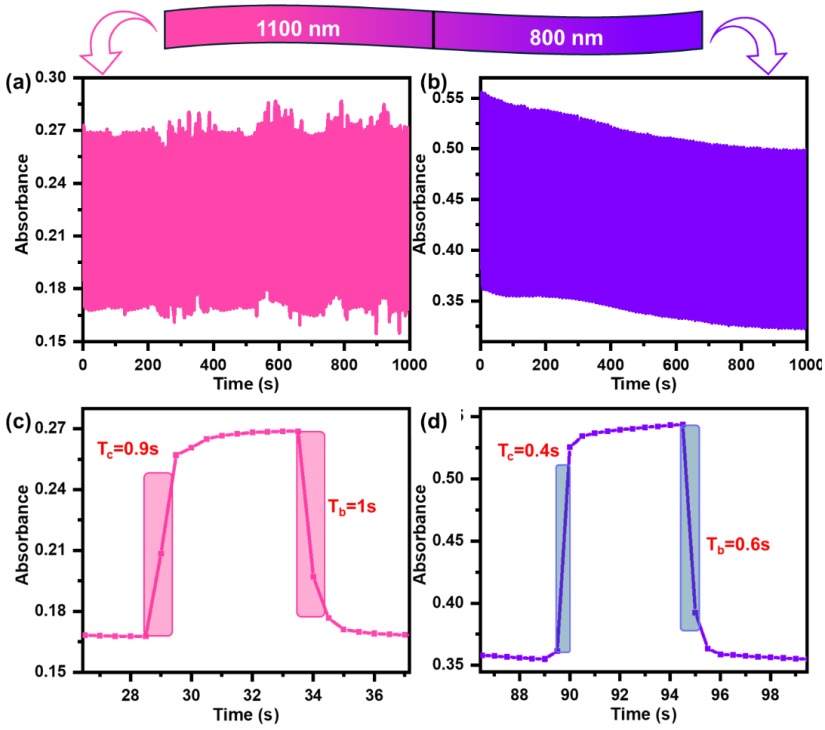

Figure 3.17: The switching stability of the *flex-NIR-Cutting ECD* at (a, b) 1100 nm and 800 nm with single switching cycle at (c,d) 1100 nm and 800 nm.

A closer switching cycle was closely analyzed to see the time taken to achieve 90% change in the absorbance value which gives the switching

time. The flex-NIR cutting-ECD takes ~0.9 s to switch from the ON state to OFF state or vice versa at 1100 nm (**Figure 3.17c**). At 800 nm, a very high switching time of ~0.5 s was obtained for coloration and bleaching (**Figure 3.17d**). A switching time of a few sub seconds, one of the fast switchable devices, could be achieved due to the doping of the WS_2/WO_3 mixture, which facilitates the electrons' flow. The flake morphology of the WS_2/WO_3 mixture provides open voids for the movement of electrons from one electrode to another, which significantly improved the performance of flex-NIR cutting-ECD in terms of switching speed.

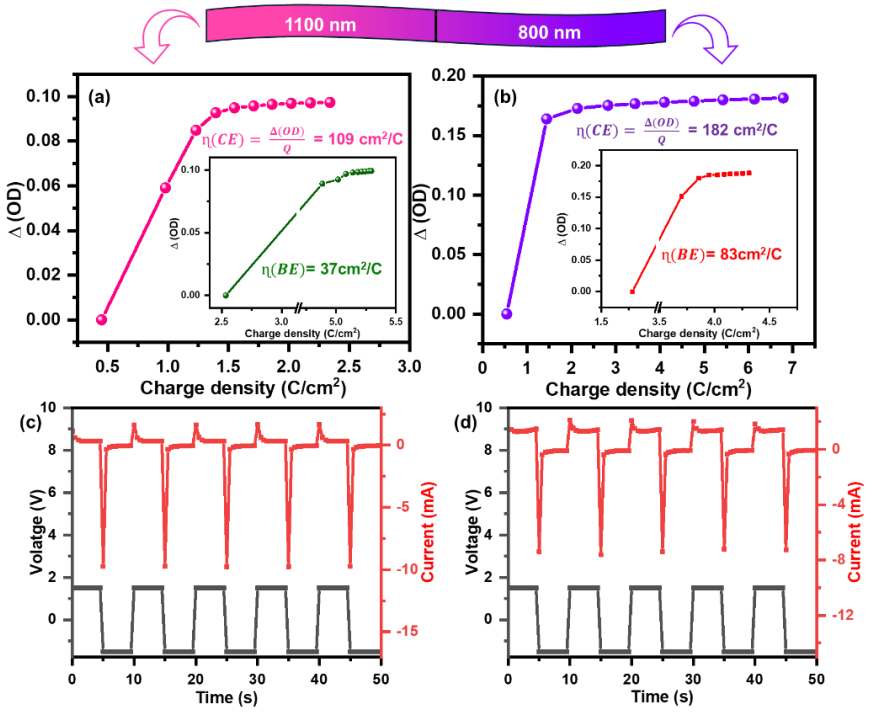

Figure 3.18: (a,b) Variation of change in optical density as a function of charge density for coloration and bleaching process (inset) at 1100 nm and 800 nm and (c,d) Current v/s voltage response of the flex-NIR cutting-ECD at 1100 nm and 800 nm respectively.

Further, another important parameter is coloration (filtering)/bleaching (non-filtering) efficiency, which is defined as ease to filter/nonfilter the heat per unit inserted charge. The coloration efficiency (η_{ce}) or bleaching efficiency (η_{be}) has been calculated using Eq. 1.2. The evaluated value of CE at 1100 nm is 109 cm^2/C (**Figure 3.18a**), while the BE is 37 cm^2/C (inset, **Figure 3.18a**). The η_{ce} and η_{be} at 800 nm were determined to be 182 cm^2/C (**Figure 3.18b**) and 83 cm^2/C (inset, **Figure 3.18b**). For calculation, the value of charge density has been calculated from the current v/s voltage graph (**Figure 3.18c** for 1100 nm and **Figure 3.18d** for 800 nm). The comparatively higher value of coloration efficiency with respect to the bleaching efficiency is due to the less charge involved in coloration. While the high charge is involved in the bleaching, the same can be seen in the current v/s voltage graph (**Figure 3.18c**), which increases the Q value in the denominator (Eq. 1.2), hence decreasing the value of BE. The above calculations make the flex-NIR cutting-ECD a fast switchable device with stable cyclic performance and moderately high coloration efficiency, which qualifies for a practical use as a heat filtering device for real life.

3.3.5 Practical Evaluation of NIR-Cutting Performance of *flex-NIR Cutting ECD.*

The above-mentioned heat cutting operation can be meaningful only if it can be of practical usage as has been investigated here. In order to check the NIR cutting practicability of ECD, the fabricated flex-NIR cutting-ECD was further checked by keeping the device, in its ON and OFF states, on a hot plate which was kept at a constant temperature of 55 °C (**Figure 3.19a**). The device shows the temperature of 43.7 °C in the OFF state (**Figure 3.19a**). The decrease in temperature between the hot plate and device was due to some heat isolation by the substrate. The photo of

the device as seen under white light is shown in **Figure 3.19b**. On applying the potential (+1.5 V), the flex-NIR cutting-ECD shows the temperature of 37.7 °C, 6 °C less than the OFF state of the device (**Figure 3.19c**). A 15% reduction in temperature makes the other area more soothing if seen from a safety goggles design point of view. The actual photo of device in ON state under white light is shown in **Figure 3.19d**. The observed decrease in temperature of the device in the ON state is due to the NIR shielding effect of the device. These above results adequately establish that the flex-NIR cutting-ECD can be used for eye soothing heat shielding flexible ECD as discussed in the above discussion.

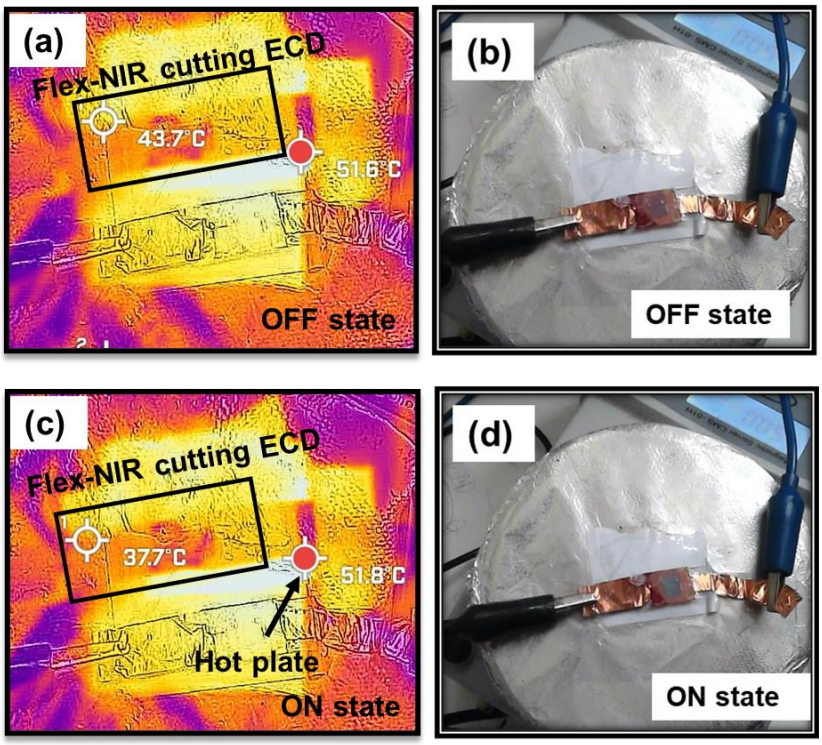

Figure 3.19: Photograph captured using a thermal (IR) camera of a hot plate covered with flex-NIR cutting-ECD in (a,b) OFF and (c,d) ON states.

3.3.6 Optical Study of the Flex-NIR Cutting ECD In the Visible Region.

In addition to the NIR region, a notable bias-dependent color transition (magenta to blue) was observed in the visible range, and the corresponding spectral variations were systematically analyzed to evaluate the device performance. As the human eye is highly sensitive to 500–600 nm in the visible region, the optical modulation or color contrast of flex-NIR cutting-ECD was studied at 515 nm in the visible region (**Figure 3.20a**). and the actual photograph of the device in colored (ON) and bleached (OFF) states is also shown in the inset of **Figure 3.20a**. Hence, the device performance has been measured in the visible regions as discussed below. The maximum optical change of the device was also observed at 515 nm. Consequently, the optical modulation or color contrast at 515 nm has been calculated using Eq. 1.1. A high OM (or CC) value of 60% was evaluated for flex-NIR cutting-ECD at 515 nm; on the other hand, the pristine EV-P3HT device shows 37% of OM only (**Figure 3.20b**). Owing to the device's great degree of reversibility, the flex-NIR cutting-ECD transmittance spectra nearly trace the curve for unbiased state.

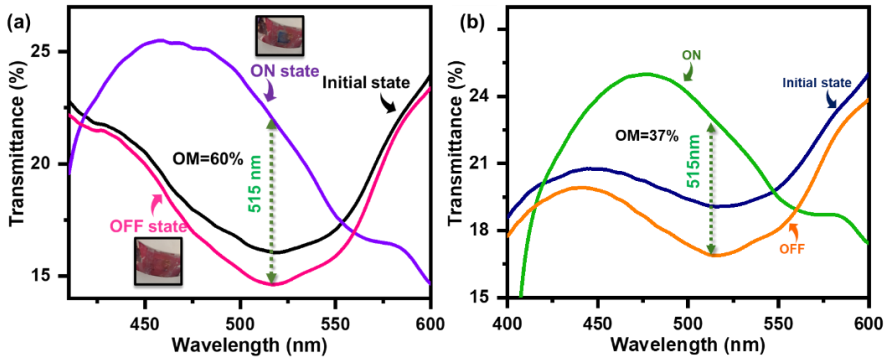

Figure 3.20: (a) In-situ transmittance spectra in visible region for (a) *flex-NIR-Cutting ECD* and (b) pristine EV-P3HT-based ECD.

The switching stability (**Figure 3.21a**) of the device was studied at 515 nm as the human eye is very sensitive to this wavelength (500 to 600 nm). Again, a pulse train of ±1.5 V (5 s each for coloration/bleaching) was applied, and the corresponding change in absorbance spectra was recorded for 1000 s. The flex-NIR cutting-ECD gives high switching stability at 515 nm with no variation in absorbance value (ΔA) for up to 100 cycles. Additionally, **Figure 3.21b** illustrates a single switching cycle of the device, indicating ~0.9 s for coloration and bleaching (90% of coloration/bleaching), in order to assess the device's switching time. Like in the NIR range, the switching speed is high also in the visible region. Furthermore, the coloration/beaching efficiency of the flex-NIR cutting-ECD has been evaluated using Eq. 1.2. A high coloration and bleaching efficiency values of 260 and 91 cm^2/C, respectively, was achieved at 515 nm wavelength (**Figure 3.21c**). For estimating the efficiency, the *Q* value has been calculated from the current v/s voltage response graph (**Figure 3.21d**).

As the human eye is more sensitive to visible range, therefore photopic coloration efficiency which covers the whole visible spectra has been calculated using Eq. 3.3

$$T_{photopic} = \frac{\int_{380}^{780} T(\lambda).S(\lambda).P(\lambda).d\lambda}{\int_{380}^{780} S(\lambda).P(\lambda).d\lambda}, \qquad (3.3)$$

where $T(\lambda)$ is the spectral transmittance of the flex-NIR cutting-ECD, $S(\lambda)$ is the normalized spectral emittance of the light source, and $P(\lambda)$ is the normalized spectral response of the eye. The $T_{photopic}$ for coloration and bleaching can be determined using the transmittance spectra in colored and bleached states of the flex-NIR cutting-ECD. The evaluated photopic transmittance values for T_b and T_c are 28.3% and 21.8%, respectively. The final photopic coloration efficiency at charge

density of 3.3 C/cm^2, which is evaluated from **Figure 3.21d**, was found to be 34 cm^2/C.

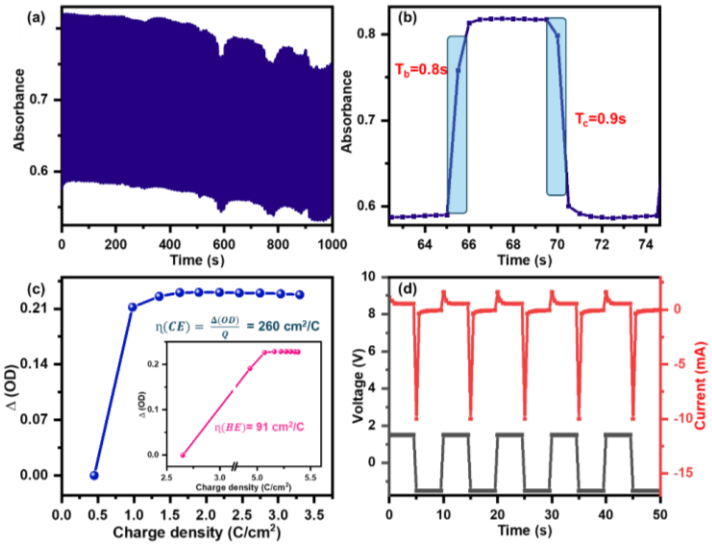

Figure 3.21: (a) Switching cyclic stability. (b) Single switching cycle. (c) Variation of change in optical density as a function of charge density for coloration and bleaching process (inset). (d) Current v/s voltage response of the flex-NIR cutting-ECD at 515 nm.

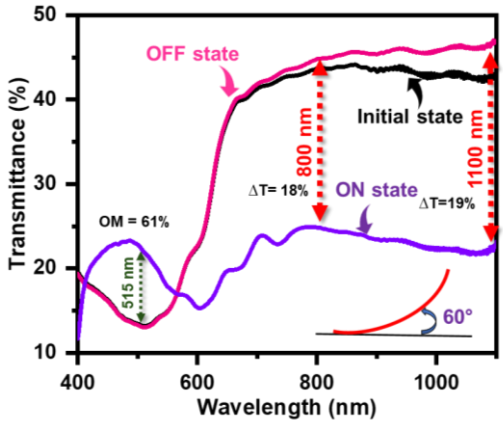

Figure 3.22: In-situ transmittance spectra of the flex-NIR cutting ECD in bent state with a bending angle of 60° (inset) in initial, ON and OFF states.

Afterward, the flexibility as well as the EC performance of flex-NIR cutting-ECD have been checked in the bent state. The bias-dependent transmittance spectra have been recorded in the bent state by bending the device 60° under ambient condition as shown in **Figure 3.22** inset. The transmittance spectra of the flex-NIR cutting-ECD in the bent state (**Figure 3.22**) is comparable with the original device as there is no significant changes in OM at 515 nm, and ΔT values at 800 and 1100 nm were observed which show the robust nature of the flex-NIR cutting-ECD. It is worth mentioning here that the little increment in the ΔT value was observed in the bent state, as the transmittance spectra has been shifted a little bit downward in the ON state. This downward shift of transmittance spectra in the ON state has increased the ΔT value at 800 and 1100 nm by 2% and 4%, respectively. The flex-NIR cutting-ECD exhibits significant performance at three different wavelengths (515 nm, visible; 800 and 1100 nm, NIR), which are collectively shown in **Table 3.3**, and has been compared with related recent works.

Table 3.3: Comparison of performance parameters for the flex-NIR cutting-ECD.

S. No.	Wavelengths (nm)	Coloration		Bleaching		Reference
		Time (s)	Efficiency (cm^2/C)	Time (s)	Efficiency (cm^2/C)	
1.	1100	0.9	109	1	37	This work
	800	0.4	182	0.6	83	
	515	0.8	260	0.9	91	

2.	700	5.1	120.9	9.7	-	Liang et al.[115]
3.	750	5	87.6	3	-	Amarri et al.[116]

The device exhibits notable electrochromic performance and blocks a sufficient amount of NIR radiation to give a soothing effect as it cuts 15% of heat by not letting the NIR radiation pass through the device when in the ON state. These above results adequately establish that a flex-NIR cutting-ECD can be used for eye soothing heat shielding flexible ECD using P3HT and WS_2/WO_3 nanoflakes' mixed viologen.

3.4 Summary and Conclusion

The incorporation of metal oxides and chalcogenides nanomaterials into the P3HT–EV-based electrochromic device enhances its performance in both visible and NIR regions. Doping p-type Co_3O_4 into P3HT and n-type WO_3 into EV enables efficient charge transfer and rapid redox switching. The flexible device shows fast coloration (1.5 s) and bleaching (2.5 s) with a high coloration efficiency of 420 cm^2/C. Maximum change in transmittance occurs at two wavelengths 515 nm and 665 nm with 50% color contrast at 515 nm. Even after repeated bending and twisting, it retains 445 cm^2/C efficiency, confirming excellent mechanical stability.

Similarly, the incorporation of a WS_2/WO_3 mixture into EV-P3HT based ECD, accelerates redox kinetics, enabling ultrafast switching of the flex-NIR-cutting ECD in both visible and NIR regions within milliseconds, with a photopic coloration efficiency of ~34 cm^2/C. The goggle-like prototype has been prepared, which offers efficient NIR shielding and a ~6 °C temperature drop under 3 V bias, providing a soothing thermal

effect to eye. The device exhibits excellent cyclic stability and high efficiency, confirming the synergistic effect of metal oxide and chalcogenide doping for next-generation flexible electrochromic and heat-filtering device.

Chapter 4

MXene-Based Asymmetric All-Organic Multifunctional Electrochromic Supercapacitor

In this chapter, an all-organic multifunctional solid-state electrochromic supercapacitor device was developed by integrating 2D-MXene with ethyl viologen and polythiophene. The incorporation of MXene into device combines electrochromic and pseudocapacitive functions within a single platform, offering high stability and dual functionality. The integration enhances charge transfer and optical modulation, enabling rapid and reversible color switching along with efficient energy storage capability. This study presents a promising strategy for designing next-generation flexible and multifunctional electrochromic supercapacitors suitable for practical and wearable applications. The findings of this work have been published in a peer-reviewed international journal[3].

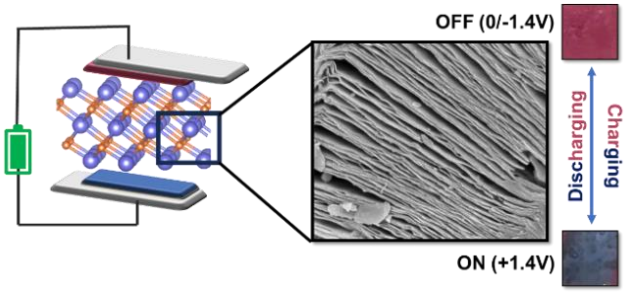

[3] Sahu. B. et al., Adv. Eng. Mater. 2024, 26, 2401295

4.1 Multifunctional All-Organic Electrochromic Supercapacitor Doped With 2D MXene

MXenes are a class of two-dimensional transition metal carbides and nitrides, synthesized by selectively etching "A" layers from MAX phase[117]. They exhibit exceptional electrical conductivity, large surface area, hydrophilicity, and pseudocapacitive behavior[53,118], making them highly suitable for applications in energy storage and electrochromic devices. Their unique thin sheet-like structure facilitates rapid ion diffusion and efficient charge transfer, enhancing both electrochemical performance and optical modulation of EC based devices. However, some EC materials also possess charge storage capability itself[43], enabling integration into multifunctional electrochromic supercapacitors that visually indicate their charge state[119–123]. Organic materials such as polythiophene (namely, P3HT) and viologens (particularly Ethyl viologen, EV) provide high conductivity and complementary redox behavior but have limited energy storage capacity. Incorporating 2-D MXenes into these polymers based ECD significantly improves charge transport, coloration efficiency, and device stability. By tuning the amount of MXene doping[124], a balance can be achieved between optical contrast and energy storage performance. MXene-doped all-organic EC devices therefore offer a versatile platform for multifunctional optical-energy applications, combining rapid optical switching with efficient energy storage[19].

4.2 Structural Characterization of 2-D MXene $Ti_3C_2T_x$

The synthesized MXene (**section 2.2.4**) has been initially characterized using FESEM, the formation of nanosheet (**Figure 4.1a**) having a few nanometers thick sheets (**Figure 1a,** inset), which will likely provide essential surface area to the electrolyte for the proper movement of

electron for energy storage application. The elemental mappings of $Ti_3C_2T_x$ were also done (**Figure 4.1b**), revealing a uniform distribution of Ti, F, C, and O throughout the material. The presence of gold (Au) is attributed to the conductive coating applied during sample preparation. These findings confirm the successful etching of the MAX phase, resulting in pure $Ti_3C_2T_x$ MXene.

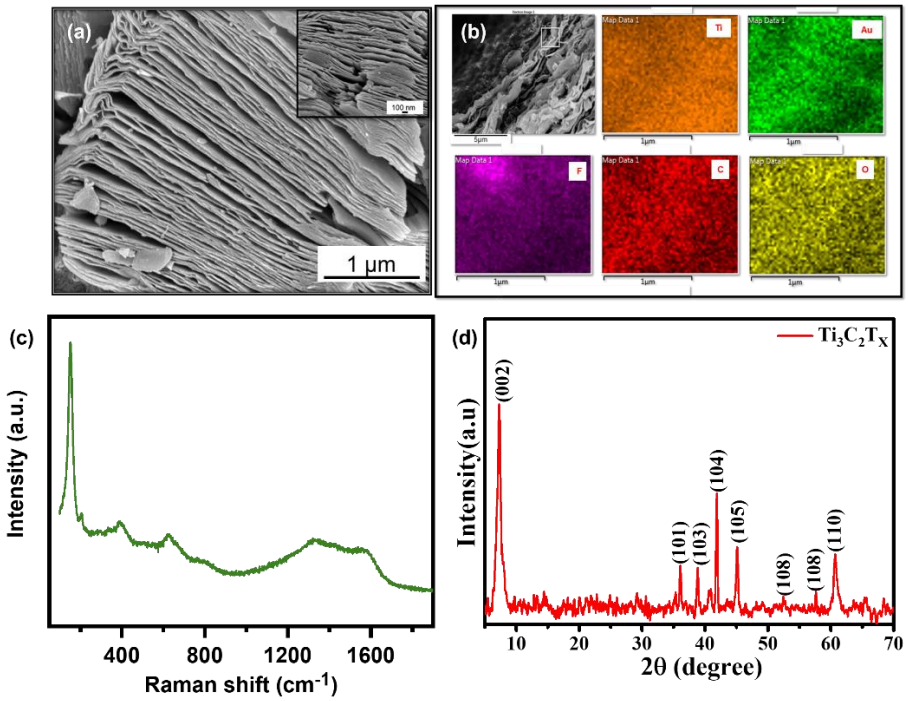

Figure 4.1: (a) FESEM micrograph along with a magnified portion (inset), (b) Elemental mapping of the synthesized MXene from MAX phase, (c) The Raman spectrum and (b) XRD pattern of MXene.

Further to validate the formation of desired MXene, Raman spectroscopy was carried out (**Figure 4.1c**). The peak at 152 cm^{-1} and 624 cm^{-1} corresponds to A_{1g} vibration modes for both the carbon layer and titanium outer layer of MXene respectively[53]. The peak at around 1320 cm^{-1} and 1570 cm^{-1}, which corresponds to the carbon D and G bands, indicates that the sample contains some free carbon.

In addition, the Powder X-Ray Diffraction (p-XRD) has been used to validate the crystallinity as well as formation of MXene from MAX phase (**Figure 4.1d**). An intense peak at 2θ = 7.2°, which corresponds to the (002) plane in the p-XRD pattern, indicates the unoxidized form of Ti3C2Tx, that is further supported by the absence of a peak at 2θ = 25°, the characteristic peak of TiO2 (JCPDS No. 52-0875). Further significant peaks were seen at 2θ = 36°, 38°, 41.8°, 45.1°, 52.5°, 57.6°, and 60.6°, which correspond to the (002), (101), (103), (104), (105), (107), (108), and (110) planes[125] respectively. These peaks demonstrate strong crystallinity of the MXene that was formed from the MAX phase. The absence of impurities in MXene is essential for having strong electrochemical characteristics, which is verified by the absence of any extra peaks in the XRD pattern.

4.3 Structural Characterization of EC Active Electrode

The prepared electrodes of MXene-doped EV and P3HT, the two EC active electrodes have been characterized using FESEM and Raman.

4.3.1 MXene Doped Ethyl Viologen (EV) Electrode

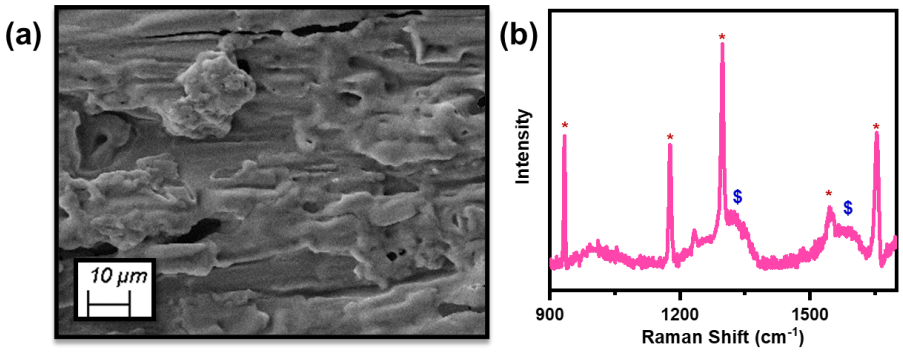

Figure 4.2 (a) The FESEM micrograph and (b) Raman spectra of MXene doped EV electrode.

The MXene-doped EV electrode has been characterized using FESEM to study surface morphology. For the same, 0.1 wt.% MXene doped in 4

wt.% EV has been drop-casted over ITO substrate. The FESEM micrograph of MXene doped EV (**figure 4.2a**) shows uniform distribution of MXene doped EV over the substrate. In the Raman spectra (**figure 4.2b**), the peak at 936 cm^{-1}, 1176 cm^{-1}, 1298 cm^{-1}, 1545 cm^{-1} and 1653 cm^{-1} corresponds to the Cl-O symmetric stretching, N-CH_2CH_3 stretching, inter-ring vibration of C-C bond, H-C-C bending along with C-N stretching and C-C inner ring vibration, respectively (represented by *)[126].

4.3.2 The Poly (3-Hexyl thiophene-2,5 diyl) (P3HT) Electrode

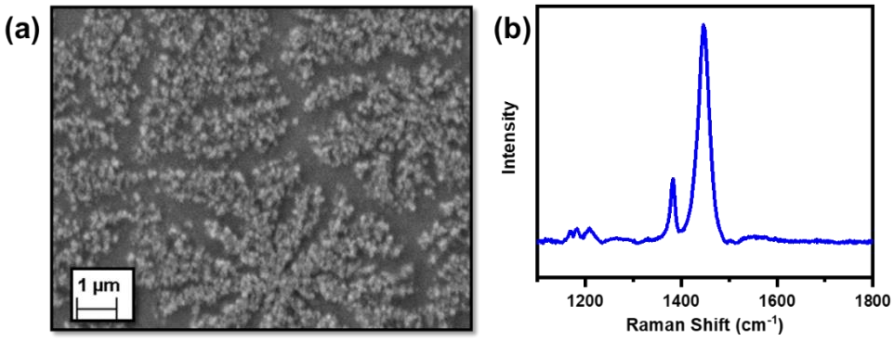

Figure 4.3: (a) The FESEM micrograph and (b) Raman spectra of P3HT electrode.

Nextly, the P3HT (chosen as secondary electrode to make M-doped ESD) spin coated over ITO electrode has been characterized using FESEM and Raman are shown in **Figure 4.3**. The FESEM micro-image shows the uniform coating of P3HT over the ITO substrate (**Figure 4.3a**). And in the Raman spectra (**Figure 4.3b**), the peak around 1380 $cm^{-1}$and 1446 cm^{-1} are the characteristic peaks corresponding to the P3HT[78].

4.4 Electrochemical Measurement of MXene And Electrodes.

The electrochemical activity of the MXene, successfully synthesized from the MAX phase, was investigated, which was studied in a standard three-electrode cell setup consisting of Platinum (Pt.) wire and Ag/AgCl

as counter and reference electrodes, respectively. A suspension of MXene was prepared for this by dispersing 10 mg of MXene in 1ml ethanol which was drop casted (10µl) on carbon cloth (CC) and used as working electrode in a 1M KOH as electrolyte.

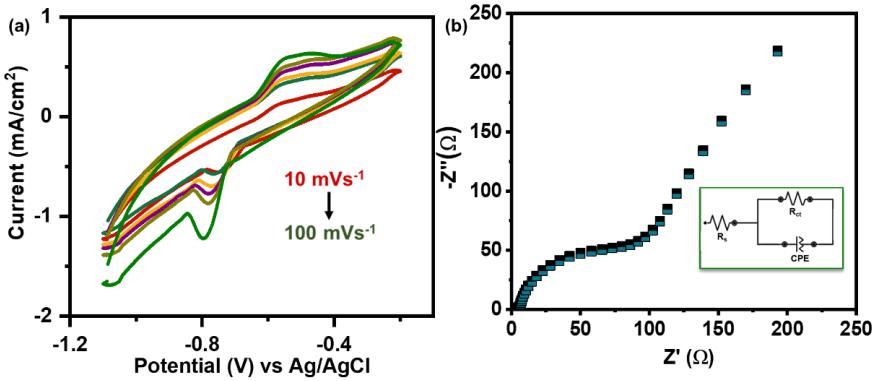

Figure 4.4: (a) The CV curves of MXene on carbon cloths at various scan rate and (b) Nyquist plot of MXene on CC with equivalent electrical circuit.

The scan rate-dependent CV curve (10 mV/s to 100mV/s) of MXene is shown in **Figure 4.4a** in the potential range of -0.2 V to -1.1 V. MXene exhibits redox activity in the negative potential, with redox peaks appearing at -0.8 V (reduction) and -0.5 V (oxidation), at 100 mV/s scan rate indicating pseudocapacitive nature of the same. Afterward, in order to look into the charge transfer mechanism, electrochemical impedance spectroscopy (EIS) was done (**Figure 4.4b**) in the frequency range of 100 kHz to 10 mHz. The Nyquist plot of MXene on CC was obtained without any bias with an amplitude of 10 mV, showing a semicircle in the high-frequency region with 2 Ω (Rs) and 98 Ω (Rct) solution and charge transfer resistance, respectively. The straight line in the lower frequency range describes the redox process at the electrode-electrolyte interface. Also, an equivalent electrical circuit has been drawn to fit the

EIS data (**Figure 4.4b,** inset). The electrochemical investigation reveals the pseudocapacitive nature of MXene.

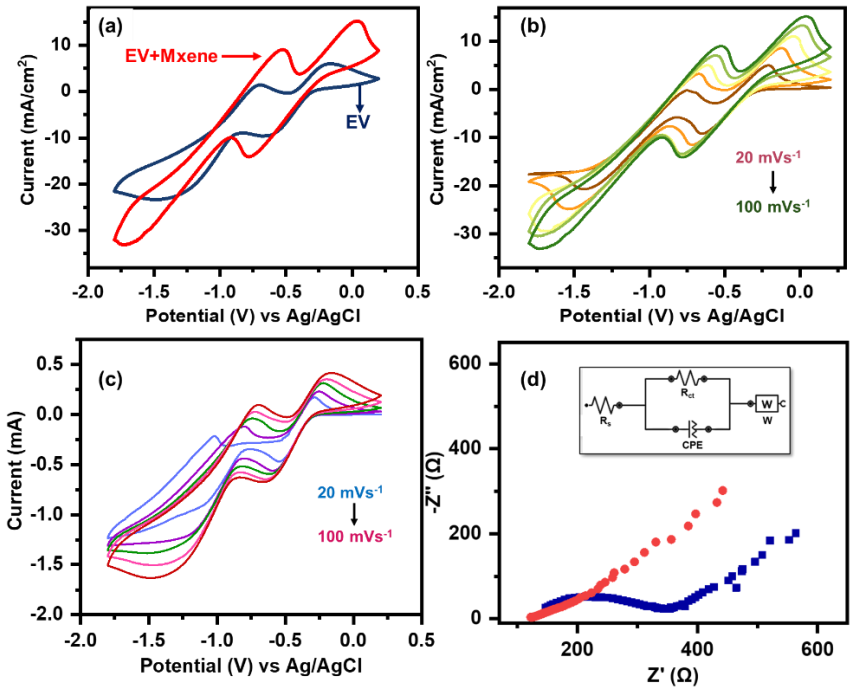

Figure 4.5: (a) Comparative CV curves of alone EV and EV+MXene on GC electrode at 100 mV/s scan rate (b) CV curves of EV+MXene with varying scan rate (c) CV curve of EV on bare GC with varying scan rate (d) Nyquist plot of alone EV and EV+MXene along with equivalent electrical circuit (inset).

Owing to the redox activity of the MXene at the negative potential, it is expected that it may enhance the electrochromic property when combined with ethyl-viologen (EV) by providing electrons and accelerating the redox reaction. For the same, electrochemical measurements were done from EV (blue curve) by using it in the solution (4 wt.% EV in ACN), and bare glassy carbon (GC) was used as the working electrode in three-electrode setup in the potential range 0.2V to -1.8V. Again, Pt. wire and Ag/AgCl were used as counter and reference electrodes, respectively. To see the effect of EV and MXene together,

MXene ink (MXene, activated carbon, and nafion were added to DI water in ratio of 75:10:15) was drop-casted on GC ∼10 µl and using which the CV was measured in an electrolyte where 4wt.% EV in ACN was present. The comparison of both the CV curves can be seen in **Figure 4.5a**. It is clear from the cyclic voltammogram, MXene in EV (red curve) shows high current giving larger area under the CV curve along with more prominent reduction (-0.8 V & -1.7 V) and oxidation peaks (-0.52 V & 0.04 V) when compared with the only EV curve when recorded at scan rate of 100 mV/s (blue curve, **Figure 4.5a**). The CV curve of MXene in EV and alone EV at various scan rates are shown in **Figure 4.5b** and **Figure 4.5c** respectively. The large area under the CV curve reveals the high charge storage capability (pseudocapacitive nature) in response to electrolyte ions intercalating on the electrode surface of the MXene, making it a viable material for doping in EV to improve their electrochromic properties and offers an additional charge storage feature, creating a device that may be used for multiple purposes. Furthermore, EIS has been carried out to better understand the ion diffusion mechanism in alone EV and MXene in EV. Nyquist plots were obtained for alone EV and EV+MXene in the frequency range of 100 kHz to 10 mHz using the same set up in which CV were obtained as mentioned at -0.5 V with an amplitude of 20 mV (**Figure 4.5d**). It is evident from **Figure 4.5d** that the Nyquist plot for MXene with EV (red curve, Figure 1d) has almost same solution resistance (R_s = 115Ω) with very low charge transfer resistance (R_{ct} = 104 Ω) due to the presence of very small semicircle show the degree of interaction between the electrolyte ions and the electrode surface is high, on the other side, the EV alone (using blank GC as electrode) has high R_{ct} value of 240 Ω in higher frequency side (blue curve, Figure 2d). When observed in the lower frequency side, MXene+EV has comparatively more inclination

towards the imaginary axis suggesting typical pseudocapacitive nature of the MXene when doped in EV. The equivalent electrical circuit has been obtained by fitting both the EIS, both alone EV and MXene+EV have same electrical circuit as shown in Figure 2d. Also, **Table 4.1**, shows the collective solution (R_s) and charge transfer (R_{ct}) resistance of MXene on carbon cloth, alone EV and MXene-doped EV electrodes. The above study confirms the pseudocapacitive nature of the MXene in 4wt.% EV (in ACN) giving high current value along with high area under the curve, proves its suitability as dopant. Consequently, MXene doped EV has been selected as n-type electrochromic active material for solid-state electrochromic device preparation to improve the electrochromic performance along with charge storage properties.

Table 4.1: Collective solution and charge transfer resistance of MXene on carbon cloth, EV and MXene-doped EV electrodes.

Electrode	Solution resistance (R_s) (Ω)	Charge transfer resistance (R_{ct}) (Ω)
MXene on carbon cloth	**2**	**98**
EV	**114**	**241**
MXene-doped EV	**115**	**104**

4.5 Optical Study of MXene Doped EV Electrode.

After successfully analyzing the electrochemical properties, the electrochromic performance of the MXene-doped EV electrode was studied in two electrode setups consisting of MXene ink (prepared

above) deposited over ITO and Pt. wire in 4 wt.% EV in ACN solution. The in-situ biased dependent transmittance spectra has been recorded by applying the ± 0.7V to the MXene-doped EV electrode (**Figure 4.6a**). Initially, during the unbiased condition, it was following the blue curve. The high transmittance was observed initially due to the transparent nature of EV. When a negative bias of -0.7V was applied to the electrode, due to the presence of EV, electrode changes its color to blue ($EV^{++} + e^{-} \rightarrow EV^{\cdot +}$), giving the red curve (**Figure 4.6a**). Again, when the reverse bias (+0.7V) is applied to the electrode, it follows the pink curve (**Figure 4.6a**). The maximum color contrast (CC) of 62.4% was observed at 600 nm which is calculated using Eq. 1.1.

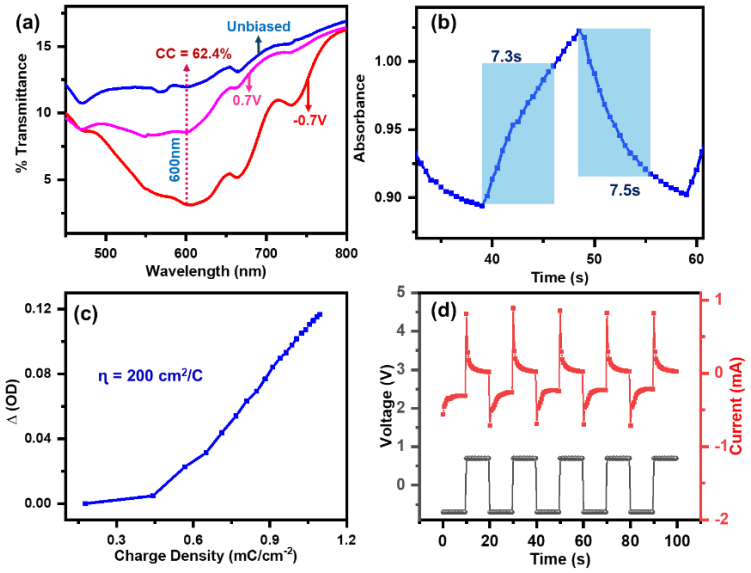

Figure 4.6: (a) In-situ transmittance spectra, (b) Single switching cycle ,(c) Current response with varying voltage pulse of ± 0.7 V, and (d) Coloration Efficiency of the MXene-doped EV in two-electrode setup.

Afterward, a crucial factor, which is the electrode's switching speed (time taken to switch between the two colors), was also examined by giving the pulse of ± 0.7V for 10 seconds each (Figure S3c, SI). The

electrode is taking ~7.5s (90% of coloration/beaching) to switch between the two colors (transparent ↔ blue) (**Figure 4.6b**). Another important parameter from the electrochromic application point of view is the coloration efficiency (η_{ce}) has also been calculated using Eq. 1.2. The η_{ce} for MXene-doped EV electrode was evaluated to be 200 cm^2/C (**Figure 4.6c**). The value of η_{ce} of the MXene-doped EV electrode was estimated from the slope of the graph between *ΔOD v/s* charge density (*Q*). The charge density has been calculated from the current *v/s*. time graph (**Figure 4.6d**).

4.6 The Fabrication of MXene-Doped EC Supercapacitor Device.

After examining the MXene-doped EV electrode's electrochromic performance and effectively characterized both electrodes, a solid-state electrochromic device (ECD), in the geometry "ITO/P3HT//EV+MXene/ITO" (schematic in **Figure 4.7**) was fabricated using the technique discussed above and as summarized in Section 2.5.1.3, in Experimental section. The schematic also shows various components and bias polarity protocol along with the photograph of the device in two different bias conditions of 1.4V (say blue or ON state) and -1.4V (say magenta or OFF state) which also corresponds to the initial or unbiased state of the device.

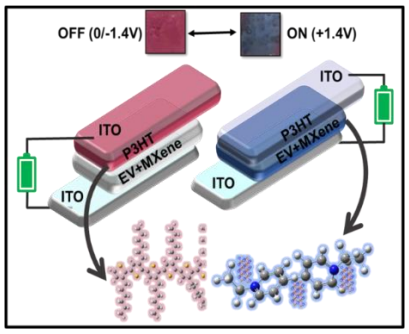

Figure 4.7: Schematic of fabricated device and corresponding photograph of actual device in two different states

As can be seen, originally, due to the transparent nature of EV and the natural color of P3HT, the M-doped-ESD was seen to be magenta in color (0V) (**Figure 4.7,** inset). After the application of 1.4 V (with respect to P3HT), the color of the device changes to blue due to the coupled redox reaction taking place between the P3HT and MXene doped EV (**Figure 4.7,** inset) as a result of dynamic doping taking place in the device. The process of dynamic doping means, due to the application of bias, the P3HT loses its electron (gets oxidized) and changes color from magenta to light blue (occurrence of bipolaronic state). Simultaneously, the MXene doped EV gains the electron given by P3HT and changes color from transparent to blue. Thus, giving overall blue color to the device. On reversing the bias polarity, the device regains its original magenta color, due to the reverse redox reaction between P3HT and MXene doped EV electrodes, showing good reversibility of the device.

4.7 Optical Study of the M-Doped ESD.

The same above-mentioned color switching mechanism of the M-doped ESD has been investigated using in-situ transmittance spectroscopy (**Figure 4.8**). The bias dependent transmittance spectra show the device's optical modulation with applied bias which corresponds to the observed color of the device. In the initial/off state the device has magenta color (black & pink curves, **Figure 4.8**) and when bias is applied, (on state) device shows blue color (blue curve, **Figure 4.8**). The maximum variation in transmittance of 13.5% and 57% was observed at 515 nm and 700 nm wavelengths respectively. The very high color contrast (CC) estimated using Eq. 1.1 was obtained to be 86% in the visible region at 515 nm, showing its suitability for smart window application.

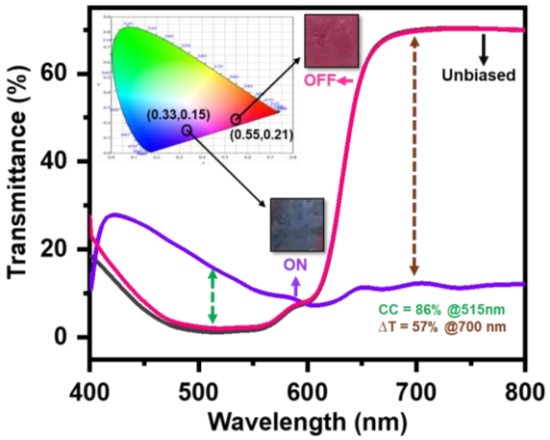

Figure 4.8: in-situ transmittance spectra of device at 0V and ± 1.4V (inset CIE plot along with actual image of the device)

Furthermore, due to the notable variation in the near-infrared region at 700 nm, high transmittance values are observed when turned off and low transmittance values when turned on, indicating its suitability as IR/thermal filter. Despite being black in appearance, the MXene doping has greatly enhanced the CC, demonstrating high appropriateness for usage in smart buildings. The reversible switching of M-doped-ESD between the magenta and blue color, when analyzed using CIE (Commission Internationale de l'Eclairge International Commission on Illumination) color chart, corresponds to coordinate (**Figure 4.8** inset) (x, y) of (0.55,0.21) in OFF state and (0.33,0.15) in ON state (Osram Sylvania).

For quantifying any electrochromic device's suitability for application, different performance parameters need to be known. As the device shows maximum variation in transmittance at 515nm and 700nm (**Figure 4.8**) therefore, these two wavelengths are chosen to study the further performance of the device like switching kinematics and coloration efficiency.

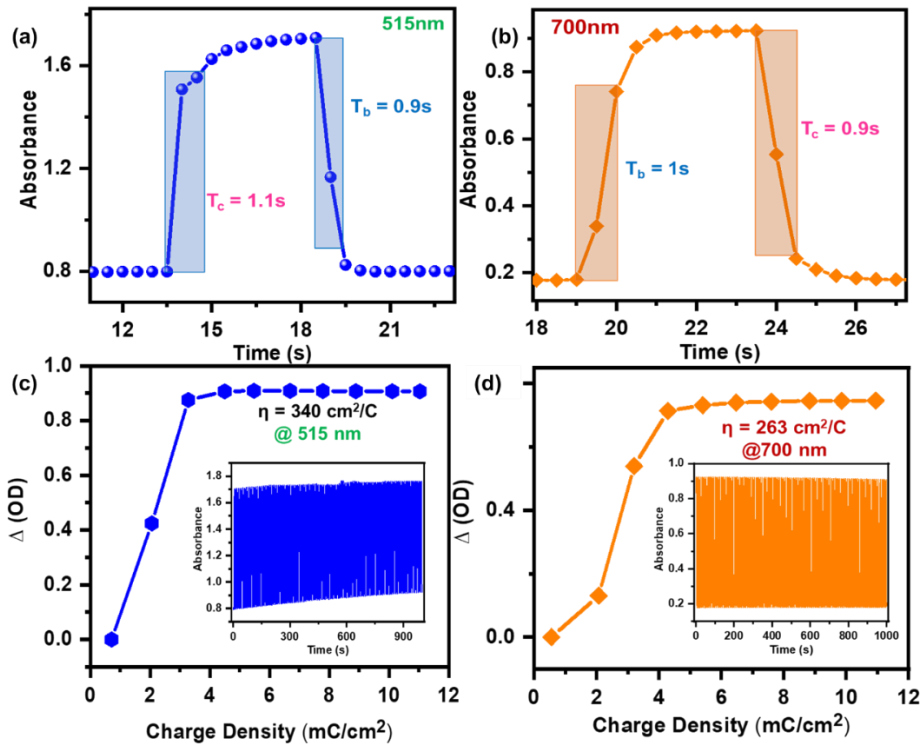

Figure 4.9: (a, b) Single switching cycle of the device at 515nm and 700nm (c, d) coloration efficiency at 515 nm and 700 nm along with stability diagram (inset).

A crucial factor is switching kinematics to study how much time is required to switch between the observed color (magenta to blue & vice versa). The device takes ∼1s (90% of coloration/beaching) to switch between the two perceived colors in both wavelengths (515nm & 700nm), meaning significantly high switching speed (coloration and bleaching) between the two colors (**Figure 4.9a, 4.9b**). Apparently, the doping of MXene, which aids in accelerating the redox reaction by providing the desired charge/electrons required for necessary redox reaction, is responsible for the device's observed rapid switching speed. Another important parameter to study ECD behavior is coloration efficiency defined in Eq. 1.2. For 515 nm (**Figure 4.9c**) and 700 nm

(**Figure 4.9d**), a significant coloring efficiency of 340 cm^2/C and 263 cm^2/C, respectively, was obtained. As mentioned above, these values were determined from the graph's slope between ΔOD *v/s* Q using Eq 1 where the necessary charge values were estimated from the current *v/s* time plot (**Figure 4.10**).

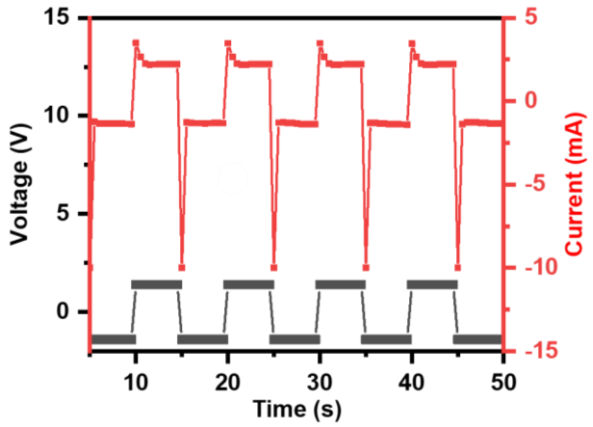

Figure 4.10: Applied square pulse of ± 1.4V and corresponding current flowing through the device.

In addition to the faster speed and high η_{ce}, the devices need to have good cycle life. The switching kinematics of device was checked for 1000s by applying the square pulse of ± 1.4V of 5s each to investigate the stability of the device. The M-doped-ESD shows great stability without much compromise in stability even after switching for 100 cycles at 515nm (inset**, Figure 4.9c**) and 700nm (inset**, Figure 4.9d**). The cyclic stability of the device at 515nm is almost constant for up to 1000s with very little gradual increase in both upper and lower absorbance value but the value of ΔA is almost constant throughout the cycle. The (little) gradual increase in absorbance value at 515nm is likely because of charge storage property of the device as some charge is getting permanently stored which does not get reversed completely while switching the bias. Therefore, a gradual increase in absorbance value was

observed in both upper and lower absorbance value side for 515 nm. But in the NIR region, constant stability was achieved as no change in the ΔA was observed for first and last cycle. On a closer look the variation looks almost similar with a small change in the absolute absorbance value in the visible region. These devices show such typical behavior and the switching gets stabilized with prolonged usage. The doping of MXene has apparently made a good performing solid state electrochromic device which is one of the best in this family as can be seen from the comparison table (**Table 4.2**). The doping of MXene in the ESD has significantly increased the performance of the device, by giving high optical contrast and accelerating the switching speed along with high efficiency. As mentioned above, the MXene has charge storage property, the doping of which in EV has increased the area as well as current, therefore the fabricated M-doped-ESD has been studied to explore the charge storage property.

Table 4.2: Comparison table for comparing the electrochromic performance of the M-doped ESD.

S.NO.	Device	Color Contrast (%)	Coloration Efficiency (cm^2/C)	References
1.	P3HT	40	230	Li et al.[127]
2.	Viologen	65	75.5	Alesanco et al.[128]
3.	P3HT/viologen	50	222	Chaudhary et al.[47]
4.	P3HT/IAI/PET	82.4	252	Kim et al.[129]

5.	P3HT+ $CoTiO_3/WO_3$	50	166	Sahu et al.[130]
6.	P3HT/EV+MXene	86	340	This work

4.8 Charge Storage Study of the M-Doped ESD

As discussed above, the prepared M-doped-ESD can have charge storage property, therefore an investigation using cyclic voltammetry (CV), electrochemical impedance spectroscopy (EIS) and galvanostatic charging discharging (GCD) has been performed. The CV curve of the device has been taken by varying the scan rate from 20 mV/s to 200mV/s in the potential window of 1.7V to 0V (**Figure 4.11a**). The oxidation and reduction peak were observed at 1.4V and 1.2V respectively for scan rate 20 mV/s which shifts to 1.6V and 0.9V respectively for higher scan rate (200mV/s), showing pseudocapacitive type nature of the device. With an increase in scan rate, the current value and the area under the curve both increases, indicating a high diffusion of ions in the device at higher scan rates.

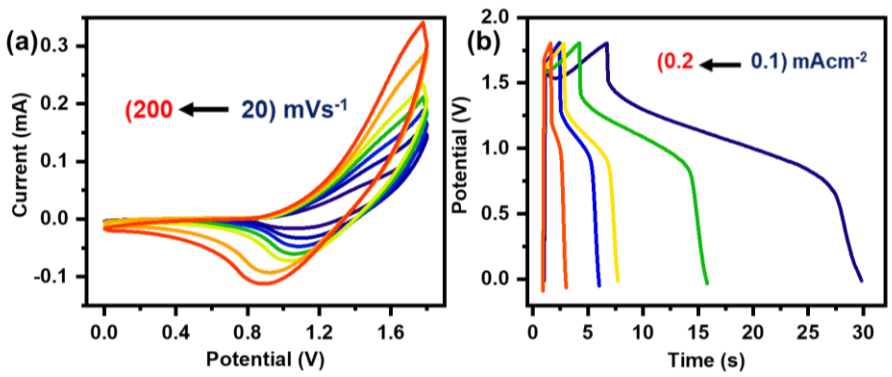

Figure 4.11: (a) Scan rate dependent CV curves from the device along with GCD plots (b).

Since the electrochromic device is storing charge, as indicated in the CV curve, the charging and discharging phenomena has been investigated

using GCD by varying the current density (0.1mA/cm^2 to 0.2mA/cm^2) in potential window 0V to 1.7V (inset **Figure 4.11b**), which shows that as the current density increases the discharging time decreases due to the high diffusion of electrolyte ions into the active materials. It was found that, for 0.1mA/cm^2, the M-doped-ESD takes a bit longer to get discharged (23.1s) than charging times (6.7s), indicating high columbic efficiency of the M-doped-ESD. When the M-doped-ESD is fully charged, it appears blue due to the positive application of a potential to the device (with respect to P3HT), and when fully discharged, it appears magenta, making it an electrochromic charge indicative supercapacitor. The pseudo-triangular shape of the GCD (**Figure 4.11b**) demonstrates the device's pseudocapacitive charge-storing capability.

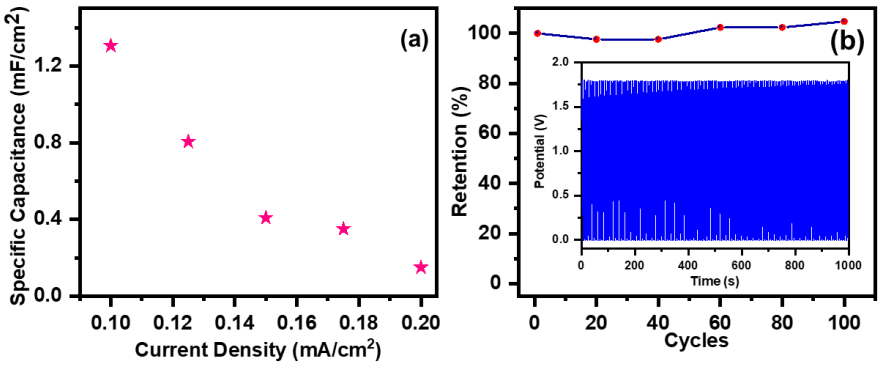

Figure 4.12: (a) Specific capacitance vs current density curve, (b) Retention graph of M-doped-ESD with capacitive stability (inset)

The specific capacitance has also been calculated for the device (Eq. 1.3, experimental section), giving a moderate value of 1.3 mF/cm^2 at 0.1mA/cm^2 (**Figure 4.12a**), and is comparable with the recently published article (**Table 4.3**).

The capacitive stability of the device has also been done at 0.3mA/cm^2 (**Figure 4.12b**, inset). The retention has been calculated (Eq 1.7) for M-

doped-ESD shows ~100% retention even after 100 cycles of switching (**Figure 4.12b**), showing its applicability for use as supercapacitor.

Table 4.3: Comparison table for comparing the energy storage application of the M-doped ESD.

S. No.	Device Name	Specific Capacitance (mF/cm^2)	Current Density (mA/cm^2)	Ref.
1.	WO_3NB/P_5W_{30}// MXene	2.84	0.98	Yang et al.[131]
2.	Asymmetric ECSC	4.0	0.1	Qu et al.[132]
3.	M-doped ESD	1.3	0.1	This work

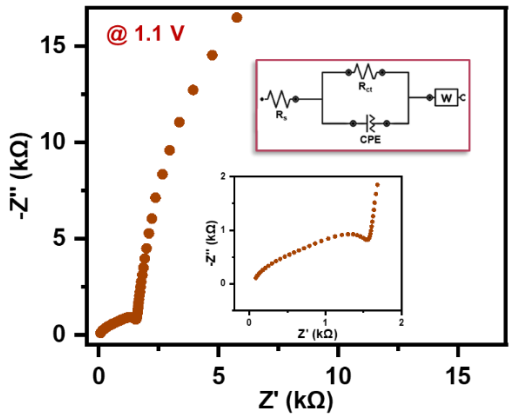

Figure 4.13: Nyquist plot of device at 1.1V with equivalent circuit (inset).

Further, to study the ion diffusion mechanism in the device, Nyquist plot has been obtained by varying the frequency from 100 kHz to 10 mHz at

voltage 1.1V with an amplitude of 20 mV (**Figure 4.13**). The Nyquist plot exhibits semicircle and linear curve in higher and lower frequency range associated with solution and charge transfer resistance giving value of 0.08 kΩ and 1.47 kΩ respectively which can also be seen in the zoomed portion of the plot in the inset. The EIS fitting has also been done to obtain the equivalent electrical circuit plot and is shown in the inset of Figure 4b. It is evident from the detailed electrochemical and spectroscopic studies that the M-doped-ESD displays improved electrochromic performance and adds supercapacitive properties. The charge storage property of MXene works as the facilitator in the process of dynamic doping to improve performance and a supercapacitor with electrochromic color indicator can be designed.

4.9 Summary and Conclusion

The incorporation of 2D MXene into an EV/P3HT-based electrochromic device enables multifunctional operation by enhancing color modulation and adding supercapacitor capability. The MXene-doped system shows reversible magenta-blue switching with high optical contrast (86%), coloration efficiency (~340 cm^2/C), and stable cycling stability over 200 cycles. It operates effectively in both visible and NIR regions, making it suitable for smart window applications. Additionally, the device exhibits color-indicative supercapacitor behavior with longer discharge, moderate capacitance (1.3 mF/cm^2), and efficient charge transfer. The improvement in the overall performance of the device is due to the doping of MXene as it is accelerating the transfer of electron from one electrode to another along with storing the charge. The doping of MXene in the device provides a viable approach to effectively create a multipurpose device for energy storage and smart window applications in real-world scenarios.

Chapter 5.

Perovskite-Based Asymmetric Organic-Inorganic Electrochromic Supercapacitor Device.

In this chapter, an organic–inorganic solid-state asymmetric electrochromic supercapacitor device (ESCD) is presented, based on nano-$CoTiO_3$/P3HT and WO_3 as two active electrodes. The $CoTiO_3$ acts as a pseudocapacitive material, adding energy storage capability while enhancing electrochromic performance of the ESCD. The device demonstrates rapid and reversible optical switching, high stability, and effective near-infrared heat blocking, highlighting its potential as a multifunctional smart heat-filtering system. This study demonstrates a viable approach to design a multifunctional electrochromic device for practical and smart applications. This result has been published in peer-reviewed international journal[4].

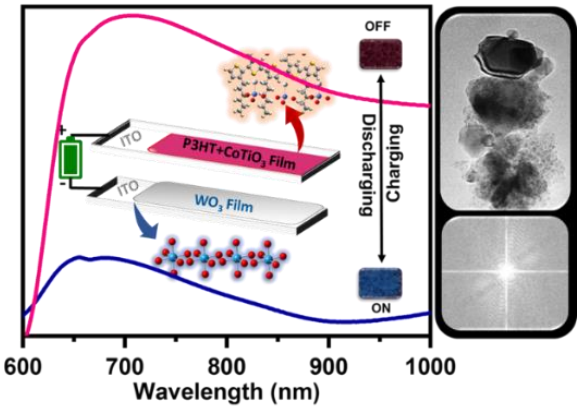

[4] Sahu. B. et al.,. J. Phys. D. Appl. Phys. 2024, 57 (24), 245110

5.1 Nano-$CoTiO_3$/P3HT and WO_3-Based ESCDs

Perovskite materials[133], characterized by their ABX_3 crystal structure, have attracted significant attention due to their exceptional optical, electronic, and ionic properties[134]. They have been widely explored in photovoltaics[135], light-emitting devices[136], sensors[137], and catalysis[138] because of their high carrier mobility, tunable bandgap, and structural versatility. In electrochromic devices, incorporation of perovskites provides strong electrochemical activity, enabling rapid and reversible color changes under applied bias. Moreover, perovskites possess high dielectric constants, which enhance their charge storage capability by facilitating efficient ion accumulation and improved capacitance. This combination of high dielectric property and redox activity makes perovskites ideal for doping in multifunctional electrochromic devices, offering both fast color switching and efficient energy storage applications. Electrochromic devices (ECDs) based on organic polymers like P3HT offer high conductivity and complementary redox activity but often suffer from slow switching and limited stability. Metal oxides such as WO_3 provide structural robustness and high stability but have lower electrochromic efficiency. Organic polymers like P3HT provide good conductivity and redox activity but suffer from slow switching, while metal oxides such as WO_3 offer stability yet lower efficiency; combining them synergistically enhances overall electrochromic performance. Additional incorporation of pseudocapacitive materials like $CoTiO_3$ further accelerates redox reactions and adds energy storage capability, enabling multifunctional, fast, and durable electrochromic devices.

5.2 Structural Characterization of $CoTiO_3$ Perovskite.

Before fabricating the solid state asymmetric ECD, the prepared $CoTiO_3$ nanoparticles powder by sol gel method (section 2.2.5) has been

characterized using FESEM techniques to confirm the formation of nano-$CoTiO_3$ (**Figure 5.1a**). The morphology of $CoTiO_3$ shows the formation of ~80 nm sized structures uniformly distributed all over the surface. The micrograph also shows the presence of macropores which is crucial for the diffusion of electrolyte ions into the inner surface of electrode. The formation of $CoTiO_3$ clusters was further confirmed from the TEM micrograph (**Figure 5.1b**). The TEM image of the $CoTiO_3$ also confirms the formation of spherical shaped material.

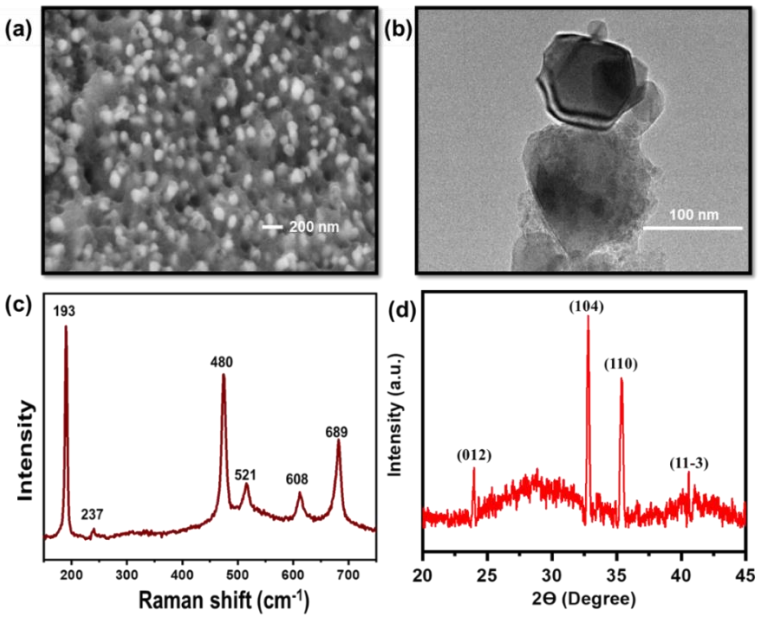

Figure 5.1: (a) The FESEM image, (b) TEM image, (c) The Raman spectrums and (b) the XRD plot of $CoTiO_3$.

Further, to verify the structural composition of $CoTiO_3$, Raman spectroscopy (**Figure 5.1c**) and XRD have been done. The Raman modes detected at 193, 237, 480, 521, 608, 689 cm^{-1} are characteristic peaks of ilmenite $CoTiO_3$[139], which is further confirmed from the XRD plot (**Figure 5.1d**). The XRD plot shows diffraction peaks at 24°, 32.8°, 35.4°, 40.5° corresponds to the (012), (104), (110), $(11\bar{3})$ planes, respectively (JCPDS Card No. 77-1373)[140]. Absence of any additional

peaks in XRD plot indicates the absence of impurity in $CoTiO_3$ which is a crucial factor for high electrochemical properties.

For the fabrication of devices, WO_3 electrode (synthesized as described in section 2.3.7) is used as a negative electrode due to its complementary redox behavior with P3HT. Before being applied to the device, WO_3 electrode was used to study its surface morphology and electrochemical performance. The surface morphology of the WO_3 electrode was studied using FESEM showing the uniform deposition of WO_3 film on ITO substrate (**Figure 5.2a**). The FESEM micrograph at higher magnification shows the formation of nano sized flower (inset, **Figure 5.2a**) of WO_3.

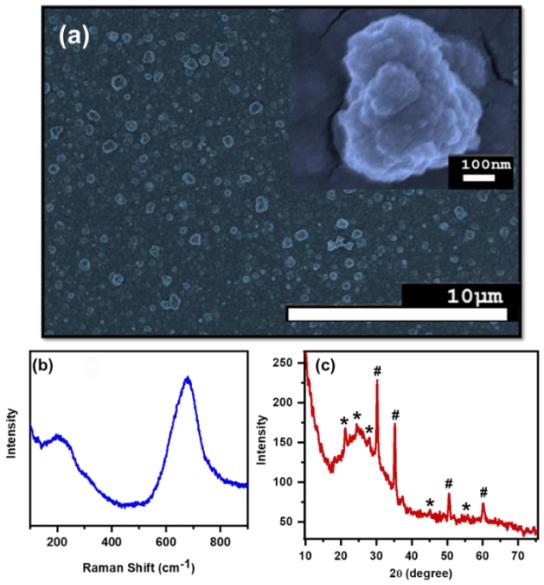

Figure 5.2: SEM micrograph of WO_3 evenly spread all over the ITO substrate along with nano flower (Inset), (b) The Raman spectrum and (b) XRD plot of WO_3 film.

The chemical composition of WO_3 have been confirmed using Raman spectroscopy and XRD (**Figures 5.2b**) [56]. The Raman spectrum exhibits two prominent features-one broad peak centered around ~758 cm^{-1} corresponding to the O–W–O stretching vibration and another near 217 cm^{-1} associated with its bending mode (**Figure 5.2b**). These

characteristic bands are in close agreement with the reported vibrational modes of monoclinic WO_3, confirming the formation of the intended oxide phase with good structural integrity.

Further the XRD plot of WO_3 film (**Figure 5.2c**) displays several distinct diffraction peaks. The peaks marked with '*' correspond to tungsten trioxide (WO_3), consistent with the JCPDS reference data (File No. 01-072-1465) [141], appearing at 2θ values of 22° (001), 23.4° (110), 25° (101), 42° (220), and 55° (202) [142]. The broad peak centered at 23.4° corresponds to the monoclinic phase of WO_3 [143]. Additional peaks marked with '#' are attributed to the underlying ITO layer on the glass substrate, appearing at 30°, 35°, 50°, and 60° [144]. The coexistence of clear and intense diffraction peaks along with the characteristic Raman bands collectively confirms the successful synthesis of a monoclinic WO_3 film.

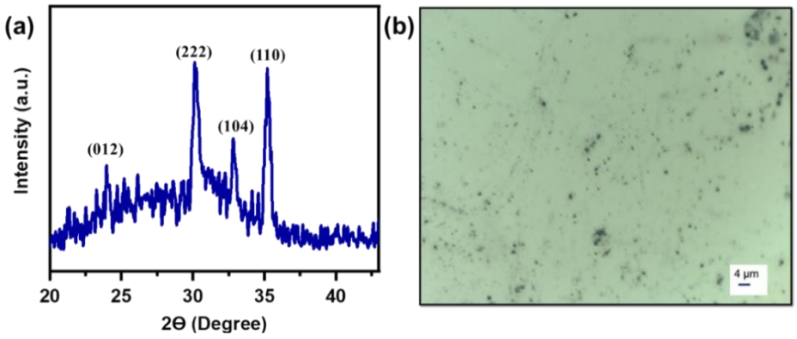

Figure 5.3: (a) The XRD plot and (b) optical image of CTO-P3HT film.

The spin-coated $CoTiO_3$-doped P3HT (CTO-P3HT) electrode (synthesized as described in section 2.3.6) has been characterized using XRD and optical microscopy which has been used to study the surface morphology of the electrode. The XRD plot (**Figure 5.3a**) of CTO-P3HT shows prominent peaks of $CoTiO_3$ at 24°, 32.8° and 35.4°along with ITO peak at 30.1° corresponding to (222) plane (JCPDS: 71-2194) [145]. Since the CTO-P3HT was coated in the indium doped tin oxide (ITO)-covered glass substrate, an obvious ITO peak has been seen. Also, the

polymer does not exhibit a peak on the XRD map, no P3HT peak has been detected. The optical micrograph of CTO-P3HT electrode shows the homogeneous distribution of $CoTiO_3$ nanoparticle over the substrate (**Figure 5.3b**).

5.3 Electrochemical Measurement of the Electrodes.

To study the electrochemical properties of $CoTiO_3$, Cyclic voltametery (CV) in the potential range of -0.5 V to 0.6 V was done at different scan rates (**Figure 5.4**) in 1 M KOH electrolyte in three-electrode arrangement. Ag/AgCl as reference electrode, Pt-wire as counter electrode and $CoTiO_3$ drop casted (10 µl) on GCE as working electrode were used.

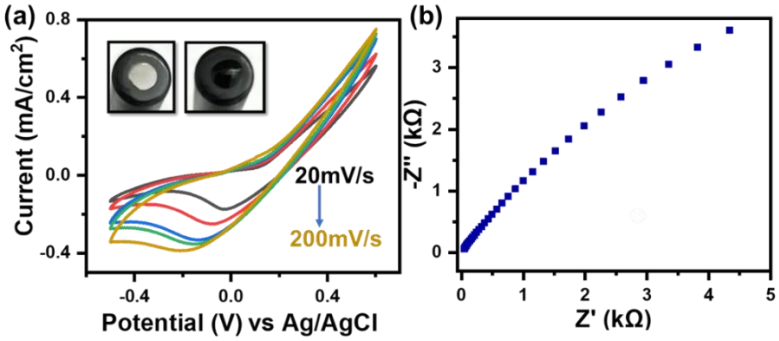

Figure 5.4: The Cyclic Voltammetry curve of $CoTiO_3$ with bare glassy carbon electrode and $CoTiO_3$ drop-casted over glassy carbon electrode and (b) Nyquist plot of $CoTiO_3$.

The CV curve of $CoTiO_3$ shows the presence of reduction peak at -0.05 V for 20 mV/s scan rate showing the material is redox active and has pseudo capacitive nature (**Figure 5.4a**). As increasing the scan rates from 20 mV/s to 200 mV/s the reduction peak gets shifted from -0.05 V to -0.2 V approximately showing faster intercalation of electrolyte ions, hence increasing the area under the curve. The presence of pseudo-rectangular shape of CV curve at negative potential window shows the charge storage capability which can be used to store charge in

electrochromic active material. A linear increase in current at positive potential window was also observed. The high current value in the positive potential window shows the presence of excess electrons which can be used to participate in redox activity of electrochromic active material to enhance its performance. So, the doping of $CoTiO_3$ in electrochromic active material P3HT helps in enhancing the redox reaction due to the presence of excess electron by adding an extra feature of charge storage property in electrochromic material P3HT in the negative potential window. To study the ion diffusion mechanism in $CoTiO_3$, electrochemical impedance spectroscopy (EIS) has been done in the frequency range 100 kHz to 10 mHz at -0.1 V, 0 V and 0.4 V with 20 mV amplitude (**Figure 5.4b**). Nyquist plot of $CoTiO_3$ at -0.1 V in high frequency range shows the solution-electrolyte contact resistance (R_s) of value 0.04 kΩ with low to negligible charge transfer resistance (R_{ct}) due to absence of semi-circle which increases for the Nyquist plot at 0 V due to the incomplete redox activity, indicating the pseudocapacitive nature of nanomaterial at -0.1 V. Also, Diffusion arc in the low frequency range at -0.1 V indicates redox mechanism and ion transport/interaction in the electrode-electrolyte interface. The diffusion arc increases from -0.1 V to 0.4 V as the diffusion increases at higher voltage as also expected from the CV curve. So, from the CV curve and EIS data it is confirmed that the $CoTiO_3$ has pseudocapacitive nature in negative potential window with high diffusion current value in the positive potential window. The charge storage nature in negative potential with high current value in the positive potential makes $CoTiO_3$ a good candidate for doping with P3HT to have application as supercapacitor, and to further increase its electrochromic property by fasting the redox activity. Thus, $CoTiO_3$ doped P3HT (CTO-P3HT) is used as positive electrode for the fabrication of device.

5.4 Electrochemical Measurement of CTO-P3HT Electrode

To check the electrochemical activity and compatibility of CTO-P3HT electrode and WO_3 electrode, CV of CTO-P3HT electrode has been performed in 0.5M $LiClO_4$ in PC, in the potential window of 1.2 V to -0.1 V at various scan rates (20mV/s to 200mV/s) (**Figures 5.5a**). Three electrode systems consisting of Ag/AgCl as reference electrode, Pt-wire as counter electrode and $CoTiO_3$ doped P3HT/ WO_3 electrode as working electrode has been used for this purpose.

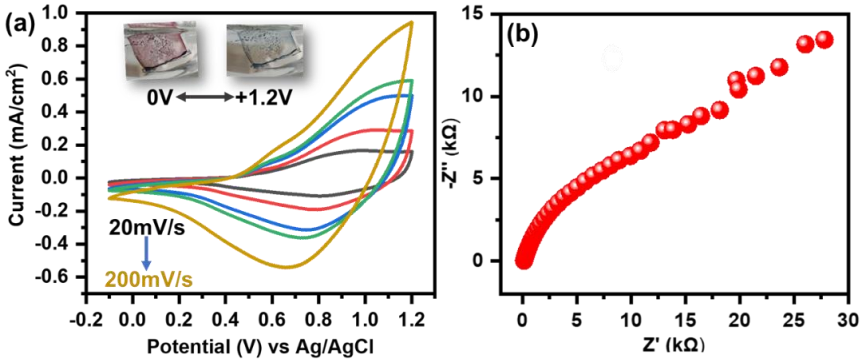

Figure 5.5: (a) Cyclic voltammetry at different scan rates (Inset: actual images) and (b) Nyquist plot at 0V of CTO-P3HT electrode

Initially, the above-mentioned P3HT electrode with incorporated $CoTiO_3$ appeared magenta in color (0V) which turns to light blue color with an applied bias (1.2V) (inset**, Figure 5.5a**). The magenta appearance of the CTO-P3HT electrode is purely due to the natural shade of P3HT. Consequently, when no bias is applied to the CTO-P3HT electrode it appeared magenta (a natural color of P3HT). However, when an external bias of 1.2V is applied to the CTO-P3HT electrode it changes its color from magenta to light blue due to the necessary redox reaction taking place on the electrode, which causes the occurrence of polaronic state of P3HT. The color change of electrode is solely due to the electrochromic active material (P3HT). No influence in the color change was observed due to the doping of $CoTiO_3$, as it is not electrochromic

active material. The doping of $CoTiO_3$ was done to enhance the electrochromic property by fasting the redox reaction and to add the charge storage property due to the pseudocapacitive nature of $CoTiO_3$. In CV curve of $CoTiO_3$ doped P3HT electrode (Figure 2a), the presence of redox peak indicates redox active nature with oxidation and reduction peak at around 0.7 V and 0.8 V respectively at 20 mV/s scan rate. The high area under the CV curve indicates more intercalation of electrolyte ions on the electrode surface confirming its charge storage capability.

Further to confirm the charge storage capability of CTO-P3HT electrode, EIS was performed (**Figure 5.5b**) at 0V in the frequency range 100 kHz to 10 mHz with 5 mV amplitude, which shows linear increase in graph, indicating pseudocapacitive nature which is in accordance with the CV curve (**Figure 5.5a**). Further the dominance of diffusion controlled and surface capacitance was evaluated using Dunn's power-law relationship Eq. 5.1:

$$i_p = av^b, \tag{5.1}$$

where i_p is the peak current at particular voltage, v is the scan rate, a and b are adjustable constants. The value of b = 0.44 for CTO-P3HT electrode at 0.8 V indicates the dominance of the diffusion-controlled process (**Figure 5.6**). The dominance of diffusion-controlled process enables faster movement of ions from electrolyte to electrode indicating the high electrochromic performance of electrode.

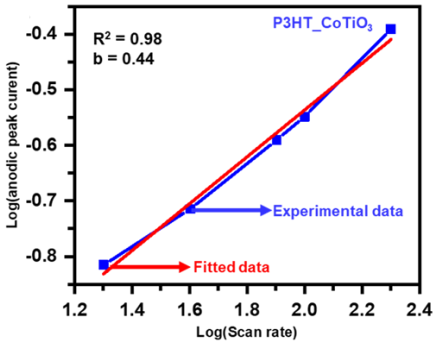

Figure 5.6: Logarithmic peak current distribution as a function of logarithmic scan rate for $CoTiO_3$ doped P3HT

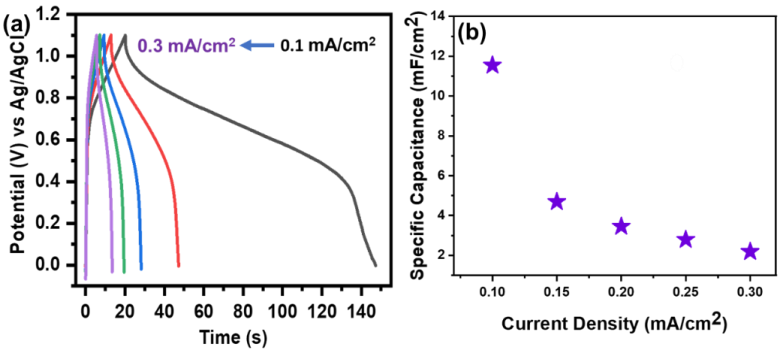

Figure 5.7: (a) Charging/discharging curves with increasing current densities and (b) corresponding Specific Capacitance vs Current density graph of CTO-P3HT electrode.

To further evaluate the charging discharging property of electrode, Galvanostatic charge-discharge (GCD) has been done at various current densities (**Figure 5.7a**). The electrode takes 20 s to completely charge whereas 127s was required to completely discharge it at a current density of 0.1 mA/cm^2 indicating a high coulombic efficiency. The non-linear decrease in potential with time under the bias of external current confirms the pseudocapacitive nature of electrode. The specific capacitance has also been calculated using Eq. 1.3. The specific capacitance calculated from GCD plot has value 11.5 mF/cm^2 for 0.1 mA/cm^2 current density (**Figure 5.7b**).

5.5 Electrochemical Measurement of WO_3 Electrode

Additionally, to check the compatibility of WO_3 electrode with CTO-P3HT, the CV curve of WO_3 film has been recorded in the electrolyte containing 0.5M H_2SO_4, in the potential range of 0.5 V to -0.5 V respectively at various scan rates (20mV/s to 200mV/s) (**Figures 5.8**). Three electrode systems consisting of Ag/AgCl as reference electrode, Pt-wire as counter electrode and $CoTiO_3$ doped P3HT/ WO_3 electrode as working electrode has been used for this purpose.

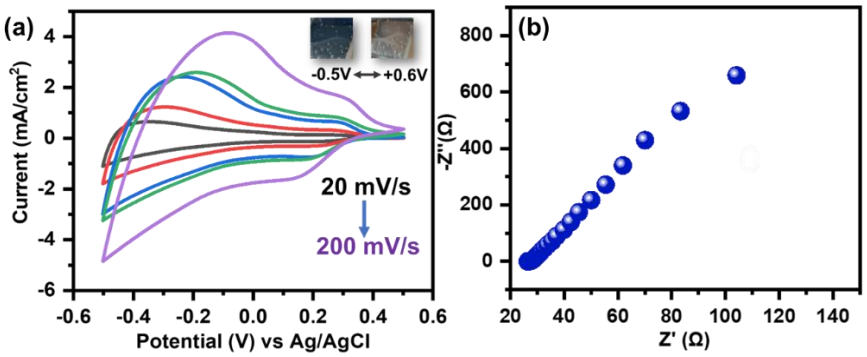

Figure 5.8: (a) Cyclic voltammetry at different scan rates (Inset: actual images) and (b) Nyquist plot at 0V of the WO_3 electrode.

Afterward, the WO_3 electrode synthesized using electrodeposition method, was used to study the electrochemical behavior in 0.5M H_2SO_4 in three electrode system as mentioned earlier. The WO_3 electrode appeared transparent under unbiased condition (0 V) and changes color to a dark blue when a field is applied (-0.5 V) (inset, **Figure 5.8a**). The change in color from transparent to blue is due to the redox reaction taking place on the WO_3 electrode. The CV curve of the WO_3 (Figure 2b) electrode shows redox peaks at 0.15 V and -0.1 V at 200 mV/s which confirms the redox active nature. The redox activity of WO_3 electrode is due to insertion and extraction of H^+ ion from electrolyte to WO_3 electrode which is given by the following equation:

$$WO_3 + n\,e^- + n\,H^+ \leftrightarrow H_nWO_3 \quad , \qquad (4.1)$$

The apparent high area under the CV curve of WO_3 predicts the high charge storage capacities due to intercalation of electrolyte ions on the electrode surface which further increases with scan rate. To further confirm the charge storage properties of WO_3 electrode, EIS was performed (**Figure 5.8b**). The linear increase of resistance in low frequency region indicates pseudocapacitive nature as also expected from the CV curve of WO_3.

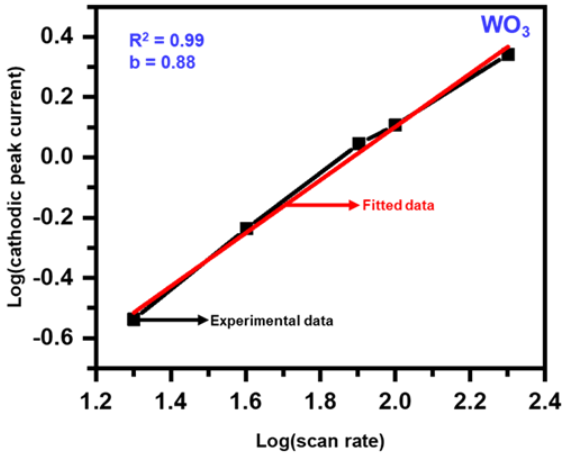

Figure 5.9: Logarithmic peak current distribution as a function of logarithmic scan rate for WO_3 electrode.

Additionally, the dominance of diffusion controlled- and surface-capacitive current was further evaluated for WO_3 film using Eq. 5.1 (**Figure 5.9**) which helps in finding the value of b which in turn helps in inferring the above dominance. The value of b = 0.88 for WO_3 electrode at -0.15 V indicates the dominance of surface capacitance.

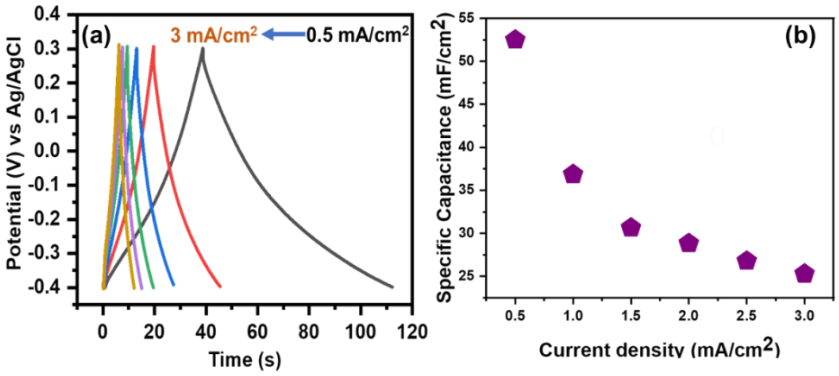

Figure 5.10: (a) Charging/discharging curves with increasing current densities and (b) corresponding Specific Capacitance vs Current density graph of WO_3 electrode.

To determine the charging discharging properties of WO_3 electrode, GCD tests have been taken at various current densities (0.5mA/cm^2 to 3mA/cm^2). This data shows that discharging takes more time than charging the WO_3 electrode. The WO_3 electrode takes ∼ 38 s to charge and ∼74 s to discharge completely at 0.5 mA/cm^2 (**Figure 5.10a**), indicating high coulombic efficiency of the WO_3 electrode. The specific capacitance (**Figure 5.10b**) has been calculated using Eq.1.3 with various current densities from the GCD plot of the WO_3 electrode. These calculations show a maximum capacitance of 53 mF/cm² at 0.5 mA/cm² current density. From the above discussion of the two electrodes, it is confirmed that WO_3 and CTO-P3HT electrode have complementary optical properties with complementary redox activity and showing a pseudocapacitive nature, which confirms that CTO-P3HT and WO_3 electrodes have excellent compatibility for the fabrication of device. In addition, the dominance of diffusion-controlled process in CTO-P3HT electrode and dominance of surface capacitance with pseudocapacitive nature can enhance the electrochromic performance along with the supercapacitive nature. So, with the help of these two electrodes, a solid state asymmetric electrochromic supercapacitor device (ESCD) can be

fabricated and is expected to have charge storage capacity with high electrochromic performance.

5.6 Optical Study of the CTO-P3HT Electrodes

To study optical properties of CTO-P3HT electrode in two electrode system using CTO-P3HT electrode and Pt- wire as two electrodes in 0.5 M $LiClO_4$ in PC, the bias dependent spectro-electrochemistry of CTO-P3HT electrode has been taken. Initially the color of electrode was magenta owing to natural color of P3HT (0 V, initial state). After the application of 1.4 V, the CTO-P3HT electrode changes its color from magenta to light blue as P3HT goes to bipolaronic state[146] by losing electrons, called as bleached state. Again, when reverse bias of -1.4 V is applied it regains its original color that is magenta (colored state), revealing high color reversibility of the CTO-P3HT electrode (inset **Figure 5.11a).** The same has been verified from the in-situ biased dependent transmittance spectra of CTO-P3HT electrode. Initially the electrode absorbs green color thus transmitting magenta color (combination of red and blue), giving low transmittance value in the green region (**Figure 5.11a**). Under the external bias (1.4 V), the overall transmittance of electrode increases, or transmits all the color wavelengths implies the transparent to light blue color of the CTO-P3HT electrode. On reversing the potential (-1.4 V), the transmittance spectra of CTO-P3HT electrode retraces its initial curve confirming the reversibility of electrode. The maximum change in the transmittance of CTO-P3HT electrode was measured using color contrast (*CC*) which was achieved at 515 nm, which is calculated using the Eq. 1.1. The color contrast of ∼46 % under an external bias of ± 1.4 V was observed with color modulation $(T_n - T_f)$ of 15%. The fact that $CoTiO_3$ is not transparent and electrochromic active results in a little reduction in color contrast.

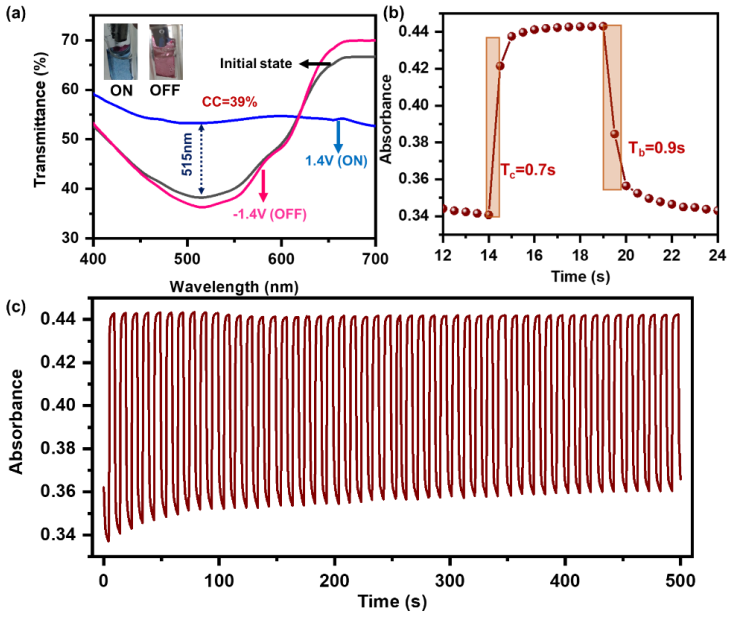

Figure 5.11: (a) In-situ transmittance spectra of $CoTiO_3$ doped P3HT electrode under an external bias of ± 1.4 V (b) single switching cycle of $CoTiO_3$ doped P3HT electrode and (c) cyclic stability at 515 nm.

The rate at which the CTO-P3HT electrode is changing color was studied using switching mechanism of the electrode (**Figure 5.11b**), under an external pulse of ±1.4 V, and corresponding absorbance spectra has been taken at 515 nm. The electrode takes 0.7 s to switch from light blue state to magenta state (coloration time) and it takes 0.9 s to switch back from magenta to light blue state (bleaching time) at 90 % of maximum transmittance change. Switching time of less than a second represents a fast color switching of the CTO-P3HT electrode, which make it a good candidate for the fabrication of device. To study the switching stability of the CTO-P3HT electrode, a square pulse of ±1.4 V was applied in an interval of 5 seconds of each polarity for 100 switching (500 s). The electrode shows excellent cyclic stability over 100 switching without much change in the transmittance value (**Figure 5.11c**). The excellent electrochromic properties of CTO-P3HT electrode

with charge storage properties shows its ability to be a potential electrode candidate for the application of electrochromic supercapacitor.

5.7 The Fabrication of Asymmetric EC Supercapacitor Device (ESCD) by Doping $CoTiO_3$

Owing to high electrochemical and optical properties of CTO-P3HT electrode with excellent compatibility with WO_3 electrode, an asymmetric electrochromic supercapacitor device (ESCD) has been fabricated (section 2.5.1.4). The CTO-P3HT was chosen as a positive electrode, and WO_3 as negative electrode for device fabrication using a flip chip method as discussed in the experimental section 2.5.1.4. The fabricated structure of solid-state asymmetric ESCD obtained was ″ITO/CTO-P3HT // WO_3/ITO″, by sandwiching PEO gel containing 1M $LiClO_4$ in PC between the two electrodes aligned as schematic shown in **Figure 5.12**, along with the actual photographs of the device in ON and OFF state. The PEO gel containing 1M $LiClO_4$ in PC is transparent in nature due to its application in electrochromism by creating a channel for electron transport from one electrode to another which is important for redox reaction to occur.

Initially, identical to the electrode (Figure 2) the color of the device is magenta due to the transparent nature of WO_3 and magenta color of P3HT in its initial state (0 V). Under the external bias of 1.6 V, the device changes its color from magenta to blue, due to the electrode containing $CoTiO_3$ in the P3HT matrix loses its electrons and goes to a bipolaronic state, resulting in change of color from its initial magenta color to blue. At the same time, the electrode containing WO_3 changes its color from transparent to blue by gaining the electrons donated by the P3HT matrix, resulting in a reduction of W^{+6} to its reduced W^{5+} state, depicting the overall color of device as blue (inset, Figure 4b).

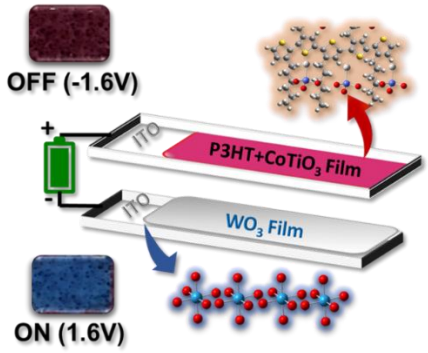

Figure 5.12: Schematic of the fabricated ESCD.

5.8 Optical Study of the Fabricated EC Supercapacitor Device (ESCD)

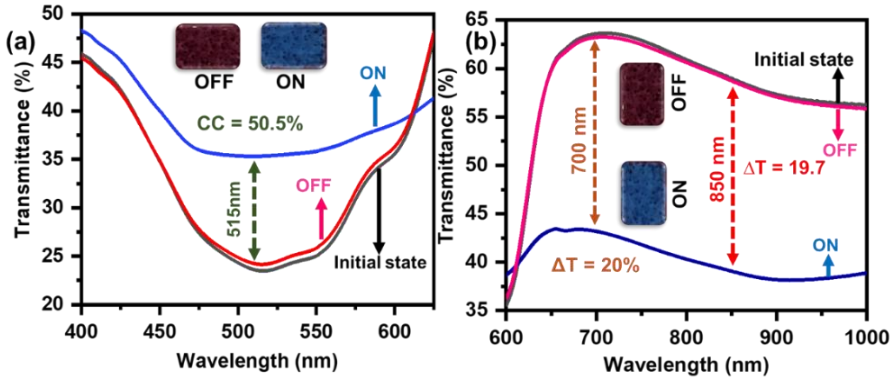

Figure 5.13: In-situ biased dependent transmittance spectra of the device at initial, on and off state with actual photographs (a) in visible range (b) in NIR range.

Owing to the gradual change in optical properties of device ESCD, in-situ biased dependent tranmittance spectra has been recorded to study the optical change in ESCD under an external bias of ±1.6 V. Initially the device is in magenta color which was confirmed using tranmittance spectrum (**Figure 5.13a**), under an bias of +1.6 V the color of device changes from magenta to dark blue due to transmitting all wavelength as can be understood from almost purple flat line. On reversing the bias, the device regains its magenta color, as P3HT comes back to its neutral state

while at the same time WO_3 get oxidised re-establishing its orginal W (VI) state

The maximum change in transmittance of 11.2% occurs at 515 nm in the visible range, corresponding to the color contrast value of 50.5%, calculated using Eq. 1.1. The high color contrast of device is due to the complemetary redox active nature of device with complementary color. In addition to that, the maximum change in transmittance was also observed at 700 nm and 850 nm (NIR region), giving the value of ΔT as 20% and 19.7% respectively (**Figure 5.13b**). The high transmittance change at 850 nm indicates the possible application as heat filter, as the device is blocking the heat in ON state and transmitting heat in OFF state. The switching dynamics of device was studied by applying continous square pulse of ±1.6 V and corresponding absorbance spectra was recorded at 515 nm, 700 nm, and 850 nm. The coloration time (blue to magenta) and the bleaching time (magenta to blue) was calculated at 90% of its maximum change and is found to be 0.8 s and 1.8 s respectively at 515 nm (**Figure 5.14a**). On the other hand the device takes 1 s for coloration time and and 3 s for bleaching time at 700 nm (**Figure 5.14b**), and 1.5 s for absorbing and 2.2 s for transmitting 90% of its maximum absorbance change at 850 nm (**Figure 5.14c**).

The coloration efficiency is one of the crucial factors to quantify the performance of electrochromic devices. The coloration efficiency (η_{ce}) of the prepared device is calculated by the Eq. 1.2. The η_{ce} was found to be 166 cm^2/C, 91cm^2/C and 80 cm^2/C at 515 nm (**Figure 5.15a**), 700 nm (**Figure 5.15b**), and 850 nm (**Figure 5.15c**) respectively. The coressponding Q value has been calculated from current density response of device under an external pulse train of ±1.6 V (**Figure 5.15d**), an excellent current stability was observed. The low coloration efficiency of device was due to the charge storage capability of the device (being charge

stored at denominator in formula) which also validates the conclusion drawn from the electrochemical properties of the electrodes .

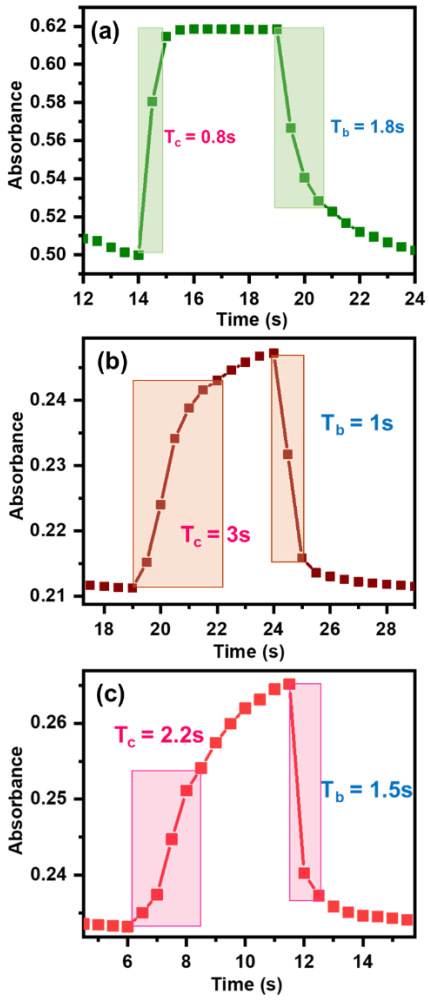

Figure 5.14: Single switching cycle of colored and bleached state of the device at (a) 515 nm, (b) 700 nm and (c) 850 nm.

For the application purpose the device should show good stability and switchability under the external stimuli, the cyclic stability of the solid state asymmetric ESCD is the measure of how effectively it can switch between the two color and for how many cycles. The stability of device at 515 nm has been measured by applying a continous pulse of ±1.6 V in an interval of 5 s each polarity for 200 pulses (1000 s) (**Figure 5.16**).

Almost constant change in absorbance spectra in cycle life of solid state asymmetric ESCD except a little change in the beigining where the devices encounters a bit initial chemical modifications and remains almost constant afterwards.

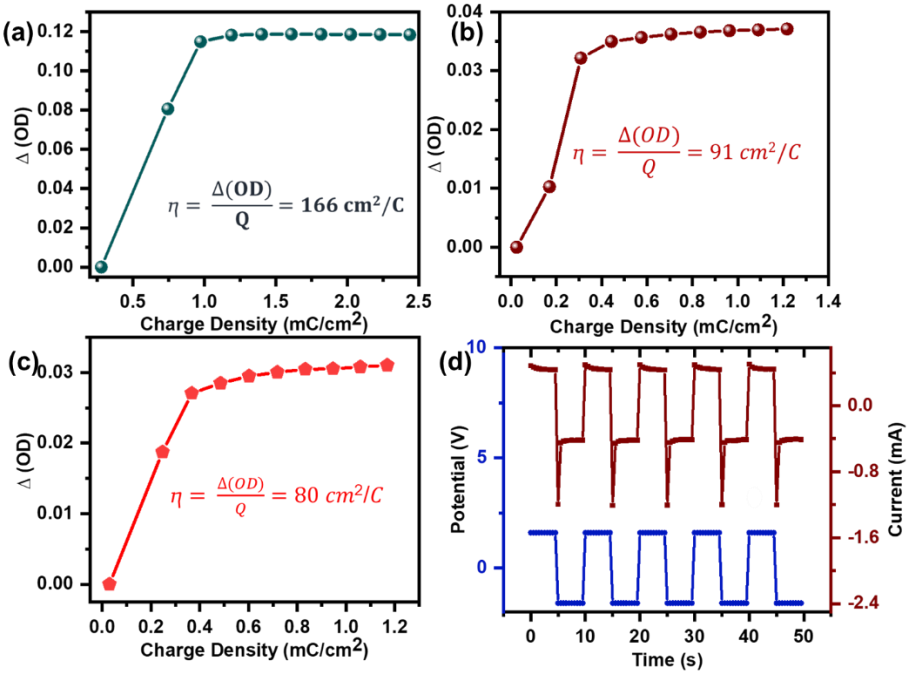

Figure 5.15: Coloration Efficiency of ESCD at (a) 515 nm, (b) 700 nm and (c) 850 nm and (d) Current vs time vs potential plot.

Further cycle stability for 700 nm (**Figure 5.16b**) and 850 nm (**Figure 5.16c**) has been measured by applying a square pulse of ±1.6 V in an interval of 5 s each polarity for 80 switching (700 nm) and 70 switching (850 nm) respectively. The device shows remarkable stability at both 700 nm and 850 nm, keeping change in absorbance constant even after continious use for 80 and 70 switchings. The high cyclic stability of the shown device might be due to the integration of CTO-P3HT polymer matrix which acts as an electron donor at positive applied potentials. It is worth mentioning here that absorbance of the device decreases (keeping change constant) is due to the charge storage capability of $CoTiO_3$

integrated into P3HT and WO_3 electrodes as also predicted earlier by CV analysis of electrodes.

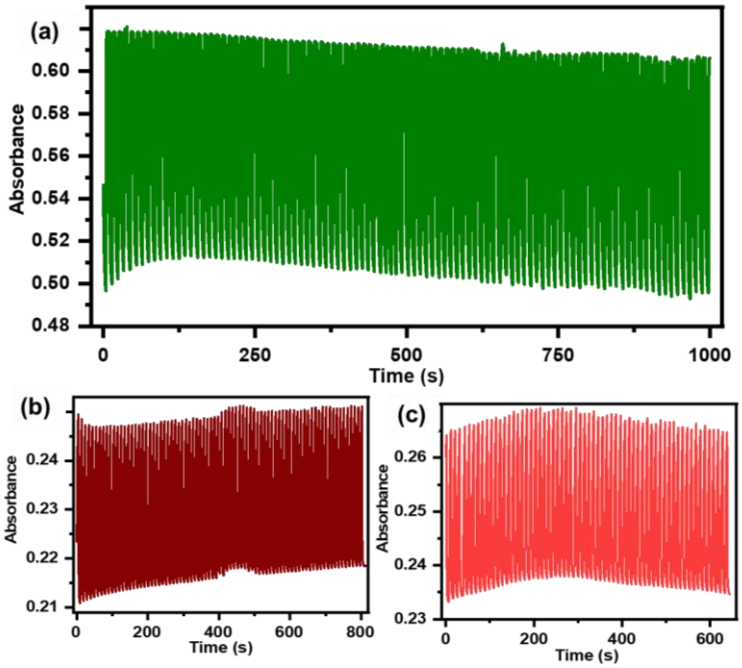

Figure 5.16: Cycle life of ESCD at (a) 515 nm, (b) 700 nm and (c) 850 nm.

5.9 Charge Storage Property of the ESCD.

As mentioned above, both the chosen electrode shows supercapacitive properties, therefore the charge storage property of device has been investigated using the electrochemistry. To study the charge storage dynamics of the fabricated ESCD, CV was obtained (**Figure 5.17**) at various scan rates (20 mV/s to 200 mV/s) in potential range of 1.6 V to 0 V. A proportionality between the current and the scan rate was observed, which implies that the electrolyte ions can easily access the active material. The CV curve of the device also shows redox peaks indicating the pseudocapacitive nature. The high area under CV curve indicates the charge storage capability of the ESCD.

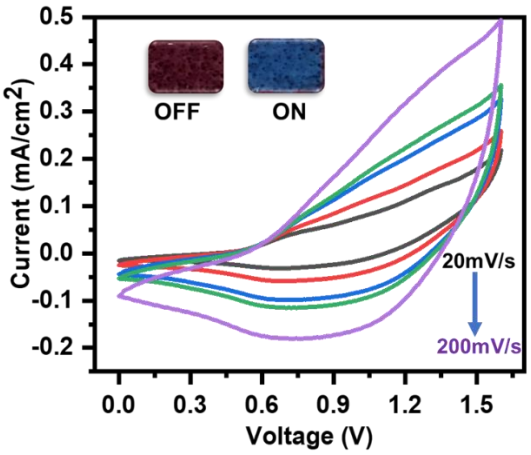

Figure 5.17: Cyclic voltammetry of the device at different scan rates (20mV/s to 200mV/s).

The dominance of diffusion controlled, and surface capacitance was further calculated at various potential (**Figure 5.18a- 5.18c**) using Eq. 5.1. The value of b = 0.44 and b= 0.43 at 0.8 V and 1.4 V respectively, indicates the dominance of diffusion-controlled process while charging. The dominance of diffusion-controlled process while charging indicates faster charging. Similarly, the value of b = 0.94 at 0.8V while discharging indicates the dominance of surface-controlled process. The dominance of surface capacitance while discharging indicates supercapacitive nature of device.

Further the overall contribution from diffusion-controlled and surface capacitance is calculated using the Dunn method (Eq. 5.2) as below-

$$i_p = k_1 v + k_2 v^{\frac{1}{2}}, \qquad (5.2)$$

where $k_1 v$ and $k_2 v^{\frac{1}{2}}$ represent the current response for surface capacitance and diffusion-controlled contributions respectively.The value of k_1 = 0.816 and k_2 = 0.066 is calculated from the slope and intercept value respectively from the graph of graph $i_p/v^{1/2}$ v/s $v^{1/2}$ plotted at 0.8 V for discharging process (**Figure 5.18d**). On putting the values

of k1 and k2 in Eq. 5, it is found that 64% of maximum current contributes to the surface capacitance at low scan rate of 20 mV/s which increases to 85 % at 200 mV/s (**Figure 5.19**).

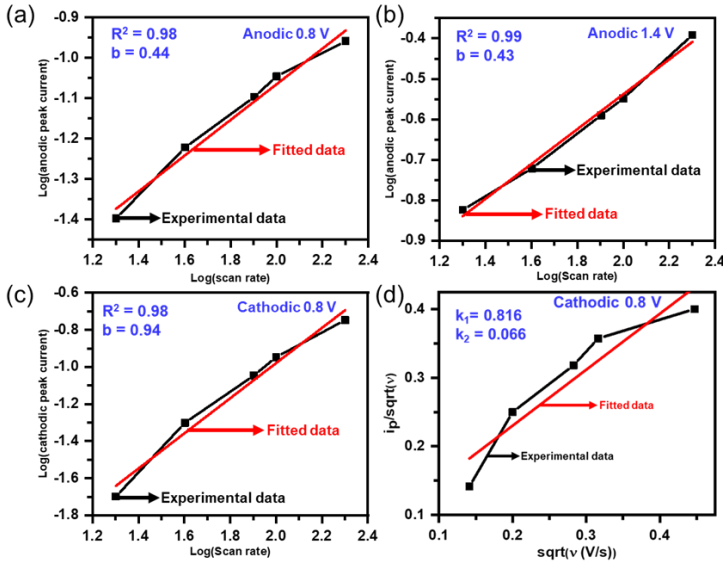

Figure 5.18: Logarithmic peak current distribution as a function of logarithmic scan rate @ 1.4 V (anodic current) (b) 0.8 V (anodic current) and (c) 0.8V (cathodic current), and $i_p/sqrt(scan\ rate)$ as a function of *sqrt(scan rate)*.

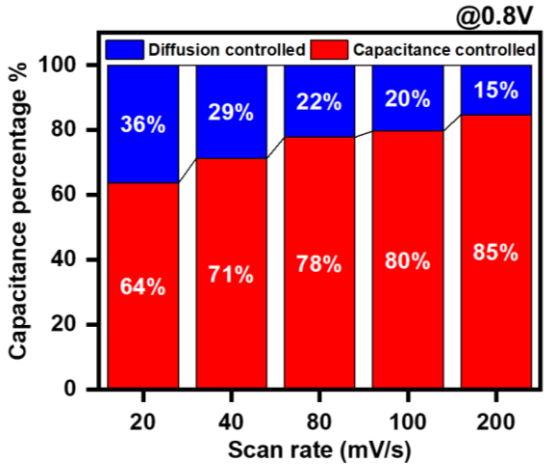

Figure 5.19: Capacitance percentage distribution as a function of scan rate.

The charging/discharging mechanism of the ESCD has been studied using GCD profile in the potential range of 0 V to 1.4 V (**Figure 5.20a**) at various current density. The ESCD gradually changes its blue state to magenta under discharging and regain its blue state quickly while charging. The GCD plot shows that the ESCD is taking more time to discharge compared to charging, indicating the high columbic efficiency of the ESCD. The ESCD takes only ~8 s to completely charge whereas it takes ~45 s to get completely discharged, which decreases at higher current densities indicating the faster charging and discharging mechanism at high current density as expected. The specific capacitance of ESCD has been calculated using Eq. 1.3, resulting in a maximum specific capacitance of 6.4 mF/cm^2 at 0.2 mA/cm^2 which decreases to 0.8 mF/cm^2 at 0.6 mA/cm^2 (**Figure 5.20b**). As increasing the current density there is a gradual decrease in specific capacitance of the ESCD, which also proves pseudocapacitive nature of the device. The specific capacitance of the here presented ESCD is comparable to perivously reported devices with similar active materials (**Table 5.1**), showing appreciable results .

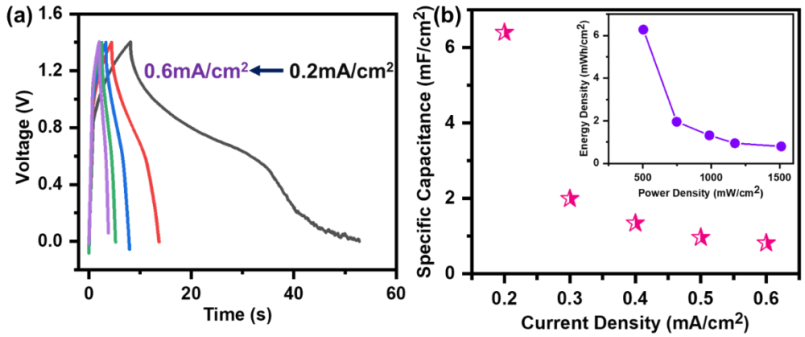

Figure 5.20: (a) charging/discharging curve of ESCD and (b) varying specific capacitance value with energy density vs power density graph. Further energy density (E) and power density (P) (inset **Figure 5.20b**) of the ESCD has been calculated at various current densities using the Eq. 1.7 and 1.8. The maximum energy density of the ESCD is 6.3

mWh/cm^2 at a power density of 500 mW/cm^2 was observed, whereas the maximum power density of 1500 mW/cm^2 was observed which is also comparable with fabricated devices of a similar type. The high charge storage property along with high energy density is due to the capability of device to strore charge in both positive and negative bias. When +1.6V (Positive bias) is applied to the ESCD, such that CTO-P3HT electrode gets +1.6V and WO_3 electrode gets -1.6V, so WO_3 electrode acts as charge storage electrode as WO_3 has property to store charge in negative region (figure 2b). When negative bias (-1.6V) is applied to the ESCD, WO_3 electrode getting +1.6V and CTO-P3HT electrode getting -1.6V. Under negative bias, CTO-P3HT electrode acts as charge storage electrode due to the charge storage property of $CoTiO_3$ in negative region. Thus, making the devcie a good candidate for real life application.

Table 5.1: Comparison of various already reported electrochromic supercapacitor device.

S.No.	Capacitor Combination	Electrolyte	Specific Capacitance (mF/cm^2)	Reference
1	P3HT|PVA-H_2SO_4|P3HT	H_2SO_4	0.91	Kasana et al[147]
2	P3HT|EC-PC$LiClO_4$|P3HT	$LiClO_4$	2.98	Kasana et al[147]
3	P3HT:PCBM/NiAl-LDH-GF	KOH	1.22	Momodu et al[148]

4	Ag-grid/PEDOT:PSS	Polymer electrolyte	2.79	Xu et al[149]
5	e-WO_3	H_2SO_4	3.5	Zhu et al[150]
6	$Ni(OH)_2$ (100 mM NiCl)-PEIE/PEDOT:PSS	PVA/LiCl	3.3	Ginting et al[151]
7	Ag/Au/PPy	KNO_3	0.58	Moon et al [152]
8	GNHC-GF	H_2SO_4–PVA	5.48	Na et al[153]
9	Au/MnO_2	Na_2SO_4	0.66	Kiruthika et al[154]
10	P3HT+$CoTiO_3$|PEO-$LiClO_4$|WO_3	$LiClO_4$	6.4	This work

Considering the above discussion, it is obvious that the fabricated solid state asymmetric ESCD ″ITO / CTO-P3HT// WO_3/ITO″, shows appreciable electrochromic performance along with super capacitive nature. The doping of $CoTiO_3$ in P3HT electrode plays a crucial role in charge storage capability of the device making its application as super capacitor along with the easy transport of charge improving the performance of solid state asymmetric ESCD. The solid state asymmetric ESCD shows good value of color contrast in three wavelengths, visible (515 nm & 700 nm) and NIR (850 nm), making it multiwavelength switching solid state asymmetric ESCD, and since it shows good change

in transmittance value in NIR region can have application as heat filter. So, due to the doping of $CoTiO_3$ in the solid state asymmetric ECD, the device shows multifunctional properties, as it has the ability to store charge and also shows satisfactory electrochromic properties.

5.10 Summary and Conclusion

A multifunctional solid-state electrochromic supercapacitor (ESCD) was developed by integrating nano-$CoTiO_3$ with P3HT and WO_3 to achieve enhanced electrochromic and supercapacitive performance. Electrochemical analysis confirmed the pseudocapacitive nature of $CoTiO_3$, facilitating efficient charge storage and electron transport. The ESCD exhibited reversible color switching between magenta and dark blue under an applied bias of ±1.6 V, showing a fast coloration and bleaching time with a color contrast of about 50% at 515 nm. Additionally, strong absorption in the NIR region (700–850 nm) indicated its heat-filtering capability. The ESCD also shows a maximum specific capacitance of 6.4 mF cm^{-2} at 0.2 mA cm^{-2} with high coulombic efficiency and stable charge–discharge behavior. Overall, the incorporation of $CoTiO_3$ effectively enhanced both electrochromic and supercapacitive functions, making the device promising for energy-saving smart window applications

Chapter 6

Carbon Materials Based Asymmetric Electrochromic Supercapacitor Devices

This chapter highlights how charge storage mechanisms govern the design of high-performance, application-specific devices. Although belonging to same carbon-based family, graphene (Gr) and graphene oxide (GO) exhibit distinct electrochemical behaviors. DFT-optimized Gr and GO nanoflakes were doped into NiO to develop electrochromic supercapacitors. GO-NiO shows diffusion-controlled charge storage with effective color modulation, enabling a color-indicative supercapacitor, while Gr-NiO exhibits a surface-controlled mechanism, allowing ultrafast color switching. Tailored carbon doping in NiO thus merges energy storage with real-world electrochromic functionality for multifunctional smart devices. This result has been published in peer-reviewed international journal[5].

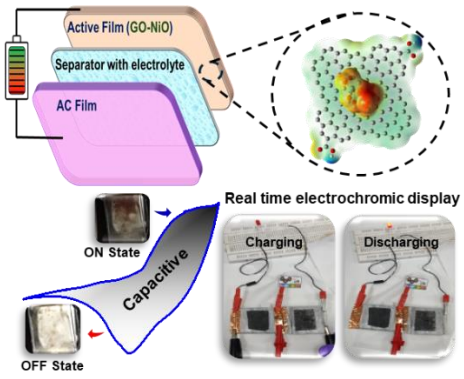

[5] Sahu. B. et al., J. Mater. Chem. C, 2026, 14, 5284 - 5297

6.1 The Family of Carbon: Graphene (Gr) and Graphene Oxide (GO)

Carbonaceous materials, including graphene (Gr), graphene oxide (GO), carbon nanotubes, MXene, and reduced graphene oxide, exhibit high electrical conductivity, large surface area, and hierarchical pore structures[155], making them widely used in electrochemical applications such as hydrogen and oxygen evolution reactions, photocatalysis[156], electrochromic windows[157], batteries[158], and supercapacitors[159]. Among these, 2-D carbon materials like Gr and GO are particularly attractive for charge storage due to their excellent conductivity, abundant active sites, tunable surface chemistry, and ability to support both surface- and diffusion-controlled charge storage mechanisms. However, the limited energy storage capacity and non-redox activity of carbon-based materials restricts their potential as electrode material in supercapacitors. These issues can potentially be addressed by combining NiO with appropriate forms of carbon. Furthermore, integrating these materials into heterostructures is expected to enhance energy storage, charge-discharge kinetics, and cyclic stability in EC and Supercapacitor devices (ECSCD).

6.2 Theoretical Optimization of Gr and GO.

Prior to doping of graphene (Gr) and graphene oxide (GO) in NiO experimentally, the molecular geometry of Gr and GO **(Figure 6.1a & 6.1b)** has been optimized theoretically. The molecular electrostatic potential (MEP) contours were plotted using the optimized geometry of Gr and GO to predict the high intercalation zones for positive and negative ions (**Figure 6.1c and 6.1d**). The high intercalation zones for positive and negative ions are indicated by the red and blue color parts in the MEP plot, respectively, with a decrease in potential value as moving from blue to red color region.

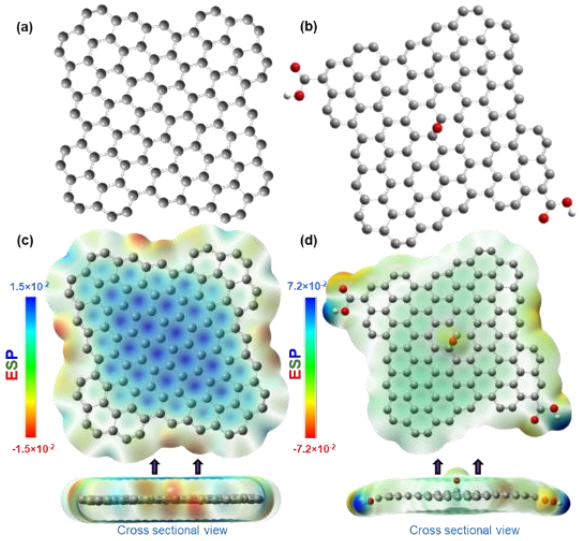

Figure 6.1: Optimized molecular geometry (a,b) and corresponding molecular electrostatic potential (MEP) plot (c,d) of graphene (Gr) and graphene oxide (GO). Cross sectional view of MEP is shown in corresponding insets.

The blue color region of the MEP plot will preferably be attacked by negative ions (OH^-), whereas the red color region will be attacked by positive ions (K^+, and Ni^{2+}). In the case of Gr, the high intercalation sites for OH^- ions are in the bulk of the material (blue region, **Figure 6.1c)**, whereas for GO, the potentially high intercalation sites are at the bulk as well as on the edges (blue region, **Figure 6.1d**). For additional clarity, the cross-sectional views of the Gr and GO are also displayed (insets **Figure 6.1c & 6.1d)**. It is worth mentioning here that the potential values for the GO molecule in the MEP plot are higher, indicating a greater intercalation of electrolyte ions, favoring diffusion diffusion-controlled charge storage mechanisms compared to Gr. The low potential values for Gr in the MEP plot indicate that less energy (or potential) will be required to intercalate/de-intercalate the electrolyte ions, implying a faster redox mechanism and surface-controlled charge storage mechanism. Hence,

high charge storage capability in the case of GO-NiO is expected, whereas faster redox switching is expected in the case of Gr-NiO.

6.3 Structural Characterization of Gr and GO Nanoflakes.

To confirm and utilize the above prediction, Gr and GO were synthesized using the recipe mentioned in the experimental section (section 2.2.6). The synthesized materials were first characterized using FESEM and Raman spectroscopy (**Figures 6.2a & 6.2b**). The FESEM shows the nano-flake-like morphology of both the materials (**Figure 6.2a**). The presence of G and D bands at 1570 cm^{-1} and 1325 cm^{-1} for Gr and 1570 cm^{-1} and 1326 GO[55] (**Figure 6.2b**).

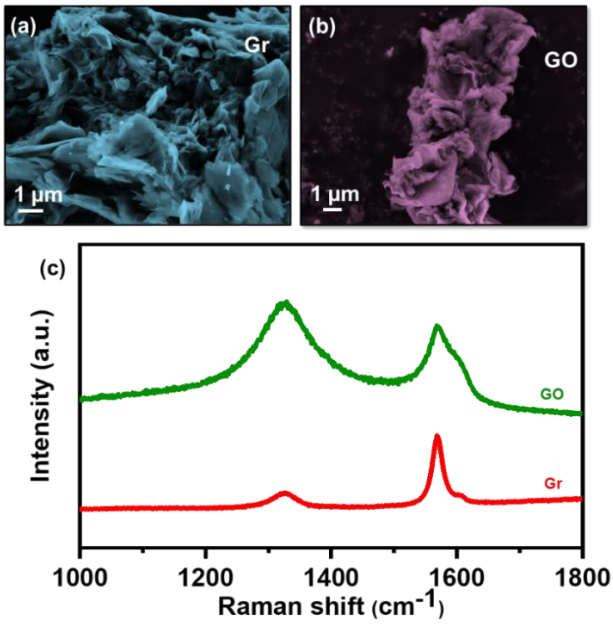

Figure 6.2: The FESEM micrographs of (a) Gr, (b) GO and Raman spectra of Gr and GO.

Following the successful synthesis of Gr and GO, it was doped in the NiO precursor solution, and the electrodes of NiO (undoped), Gr-NiO (Gr doped NiO) and GO-NiO (GO doped NiO) were prepared as mentioned in the experimental section (section 2.3.8). The FESEM image of NiO (**Figure 6.3a**) shows a nano-grain-like morphology with enough pores

uniformly distributed over the substrate. The grains are of NiO as confirmed using the Raman spectrum (inset**, Figure 6.3a**) where the peaks ~460 cm^{-1} and ~558 cm^{-1} correspond to the one phonon transverse optical (TO) and longitudinal optical (LO) modes respectively, and the other peaks ~783 cm^{-1} and ~1104 cm^{-1} correspond to the two phonon TO and LO modes respectively[160]. Similarly, the FESEM images of the Gr-NiO (**Figure 6.3b**) and GO-NiO (**Figure 6.3c**) electrodes also show the nano-grain-like morphology with sufficient porosity for intercalation of electrolytic ions, consistently distributed over the FTO-coated glass substrate.

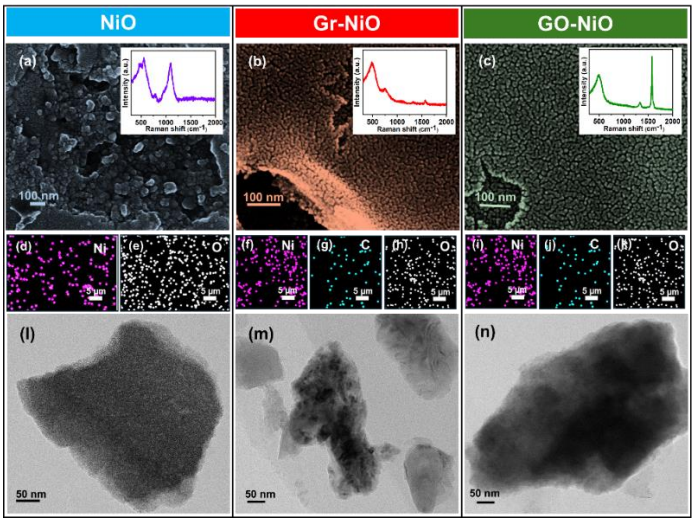

Figure 6.3: The FESEM micrographs along with Raman spectra in insets (a) NiO electrode, (b) Gr-NiO electrode, (c) GO-NiO electrode, elemental mapping images of NiO electrode (d, e), Gr-NiO electrode (f-h), GO-NiO electrode(i-k). The HRTEM microscopic images of (l) NiO, (m) Gr-NiO, and (n) GO-NiO electrodes.

Further the successful doping of Gr and GO in NiO was confirmed using the Raman spectroscopy **(**insets**, Figures 6.3b & 6.3c)**. The peak at around 489 and 755 cm^{-1} in the Gr-NiO electrode (inset, **Figure 6.3b**), and 492 cm^{-1} in the GO-NiO (inset, **Figure 6.3c**), reflects the presence of the NiO matrix. The peaks at 1321 and 1570 cm^{-1} in Gr-NiO (inset, **Figure 6.3b**),

and 1332 and 1576 cm^{-1} in GO-NiO (inset, **Figure 6.3c**) are the signature peaks of D and G bands, confirming the successful doping of GO and Gr in NiO as desired. The absence of other peaks indicates the high purity of the fabricated electrodes. Furthermore, to demonstrate the uniform distribution of Ni, O and the dopants, the elemental mapping of the electrodes NiO (**Figures 6.3d & 6.3e**), Gr-NiO (**Figure 6.3f, 6.3g & 6.3h)** and GO-NiO (**Figure 6.3i, 6.3j & 6.3k**) were done. The EDS spectra confirm the presence of Ni, O, and the presence of C in Gr-NiO and GO-NiO electrodes confirms the effective doping of Gr and GO in NiO. The morphologies of NiO, Gr-NiO, and GO-NiO were further validated by the high magnification HRTEM images (electrodes were sonicated in 0.5 ml DI water and drop-casted over the grid). The HRTEM images of NiO (**Figure 6.3l**) confirm the nano-grain microstructure, while the HRTEM images of Gr-NiO (**Figure 6.3m**) and GO-NiO (**Figure 6.3n**) reveal the flake-like microstructure.

Afterward, the presence of characteristic elements and the oxidation states in the as-prepared electrodes were investigated using XPS (**Figure 6.4**). The full survey spectrum reveals the presence of C 1s, O 1s, Ni $2p_{3/2}$ and Ni $2p_{1/2}$ NiO, Gr-NiO, GO-NiO electrodes (**Figure 6.4a**). The high-resolution Ni 2p spectrum (**Figure 6.4b**) displays two main peaks at 855 and 871 eV corresponding to the Ni $2p_{3/2}$ and $2p_{1/2}$ respectively due to the spin-orbit coupling[161]. The major peak at binding energy (BE) 855 eV was deconvoluted into two peaks at 853.8 and 856 eV, indicating that NiO exist in both Ni^{2+} and Ni^{3+} states. Another major peak at 873 eV was further deconvoluted into two peaks at 871.1 and 874 eV, suggesting the presence of identical Ni^{2+} and Ni^{3+} states in NiO[162]. The satellite peaks appear at 860.6 and 856 eV corresponds to Ni $2p_{3/2}$, and at 878.5 and 881.8 eV corresponds to Ni $2p_{1/2}$ state. The high-resolution spectrum of O 1s shows major peaks at BE values of 529, 531 and 532.6 eV attributed to

the Ni-O bond, $Ni(OH)_2$ and H_2O bonds in NiO electrode respectively[163].

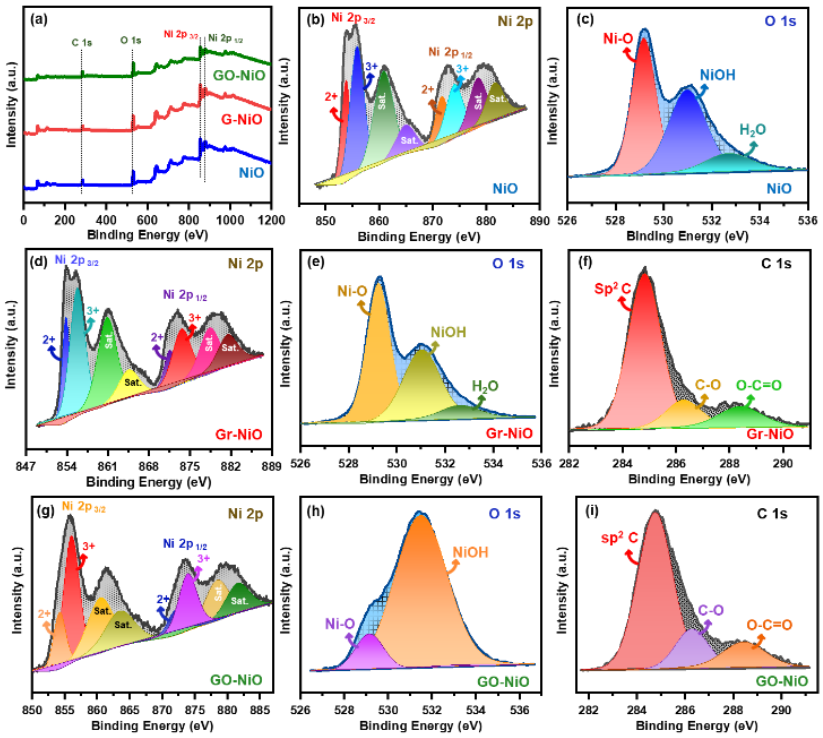

Figure 6.4: (a) XPS survey scan spectrum of NiO, Gr-NiO, GO-NiO electrodes confirming the characteristic elements, High resolution XPS spectra from (b, c) NiO, (d-f) Gr-NiO and (g-i) GO-NiO electrodes.

The high resolution XPS spectra were also recorded for the Gr-NiO (**Figures 6.4d-6.4f**) and GO-NiO (**Figures 6.4g-6.4i**) electrodes. The major peaks present at 854 eV (deconvoluted into peaks at 853.8 and 856 eV attributed to Ni^{2+} and Ni^{3+} state), and BE 855 eV (deconvoluted into Ni^{2+} and Ni^{3+} state-attributed peaks at 854.2 and 856.1 eV) in the Gr-NiO, and GO-NiO electrodes correspond to the Ni $2p_{3/2}$ (**Figures 6.4d & 6.4g**). Similarly, the peaks at 873 eV (again deconvoluted into peaks at 871.5 and 873.7 eV attributed to Ni^{2+} and Ni^{3+} state), and 873.6 eV (deconvoluted into Ni^{2+} and Ni^{3+} state-attributed peaks at 872 and 873.9 eV), in the Gr-NiO, and GO-NiO electrodes correspond to Ni $2p_{1/2}$. The

satellite peak for Ni $2p_{3/2}$ is positioned at 860.8 and 864.8 eV for Gr-NiO, and 860.6 and 863.6 eV for GO-NiO, while for Ni $2p_{1/2}$ they are positioned at BE 878.5 and 881.5 eV for Gr-NiO and GO-NiO electrodes. In the high-resolution spectra of O 1s (**Figures 6.4e** & **6.4h**), the peaks positioned at 529.2 and 531 eV for Gr-NiO and peak at 529 and 531.4 eV for GO-NiO corresponds to Ni-O, NiOH. One additional peak in GO-NiO at 532.6 eV corresponds to H_2O bonds. The high-resolution spectra of C 1s (**Figures 6.4f & 6.4i**), three characteristic peaks appeared at 284.8, 286.3, 288.4 eV for Gr-NiO, and 284.7, 286.2 and 288.4 eV which corresponds to the sp^2 C, epoxide and C═O bonds respectively[55].

6.4 Electrochemical Measurement of the Electrodes

The prepared electrodes of NiO, Gr-NiO, and GO-NiO were tested to check their electrochemical performances in the three-electrode electrochemical setup using 2M KOH as electrolyte (**Figure 6.5a**). The electroactive electrodes namely NiO, Gr-NiO and GO-NiO as working electrode (W.E.), Ag/AgCl as reference electrode (R.E.) and Platinum wire as counter electrode (C.E.). The cyclic voltammetry was performed in the potential range of -0.1 to 0.7 V at various scan rates of 5 to 50 mV/s. The comparative cyclic voltammetry (CV) curves of the NiO, Gr-NiO and GO-NiO electrodes (Figure 6.5b) were recorded at 10 mV/s scan rate. The presence of a redox couple and a large area in the CV curve of all three electrodes indicates pseudo-capacitive type charge storage property of the materials. The NiO and Gr-NiO electrodes show a notable redox couple at 0.4V and 0.28V, while the GO-NiO electrode shows more prominent peaks at 0.44V and 0.21V. The higher area under the CV curve for GO-NiO suggests its high charge storage capacity likely due to the presence of more electroactive surface area in GO, assisting more intercalation and deintercalation of electrolyte ions on the electrode surface, as also predicted from the theoretical MEP plots of Gr and GO.

The CV curves at various scan rates (5 to 50 mV/s) for the NiO, Gr-NiO, and GO-NiO (Figures 6.5c-6.5e) electrodes show an increase in area with increasing scan rate, as an indication of fast ion intercalation on the electrode surface at high scan rates. Additionally, the electrodes' shows a reversible color change to a dark state when completely oxidized (high potential) and return to its transparent form when completely reduced (low potential) which makes it eligible for application in color-indicating supercapacitor devices as has been discussed later.

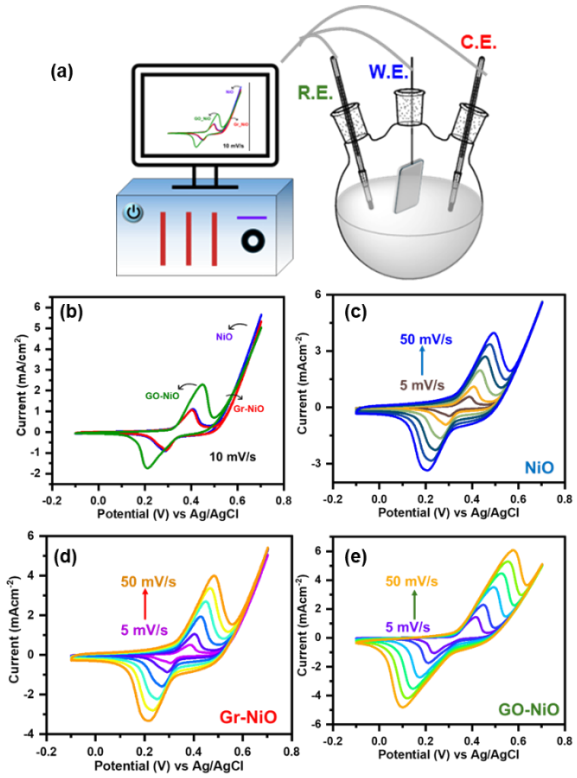

Figure 6.5: (a) Schematic of the electrochemical arrangement, (b) comparative CVs of all the electrodes, scan rate dependent CV curves of (c) NiO, (d) Gr-NiO and (e) GO-NiO electrodes.

To understand the charge storage mechanism in all the electrodes, the log (current density, J) vs log (scan rate, *v*) was plotted using Dunn's power law (Eq. 6.1) method.

$$i_p = av^b, \quad (6.1)$$

here, the i_p and v represents the peak value of current density and scan rate respectively, *a* and *b* are constants. The value of *b* indicates the dominance of charge storage mechanism (diffusion or surface controlled). The value of *b* has been obtained from the slope of *log(J)* v/s *log (v)* curve (**Figure 6.6a**). The computed values of *b* for the NiO and Gr-NiO electrodes were obtained to be 0.84 and 0.88, respectively, demonstrating surface-controlled behavior. A higher *b* value for Gr-NiO electrode is due to the doping of Gr which has an EDLC type nature. On the other hand, the calculated *b*-value for the GO-NiO electrode is 0.62, suggesting the dominance of an exceptional diffusion-controlled mechanism. To further analyze the relative contribution of diffusion and surface-controlled mechanisms toward total capacitance, Dunn's method was utilized, and Eq. 5.2 was applied.

$$i_p = k_1 v + k_2 v^{1/2}, \quad (5.2)$$

where $k_1 v$ and $k_2 v^{1/2}$ are the contribution to total capacitance indicating capacitive and diffusive controlled capacitance. It was observed that for the GO-NiO electrode the diffusion- and surface-controlled capacitance contributions were 81% and 19% at 10 mV/s, respectively (**Figure 6.6b**). The contribution of diffusion-/surface-controlled capacitance for NiO (**Figure 6.6c**) and Gr-NiO (**Figure 6.6d**) electrodes was estimated to be 59%/41% and 67%/33% respectively, at a 10 mV/s scan rate.

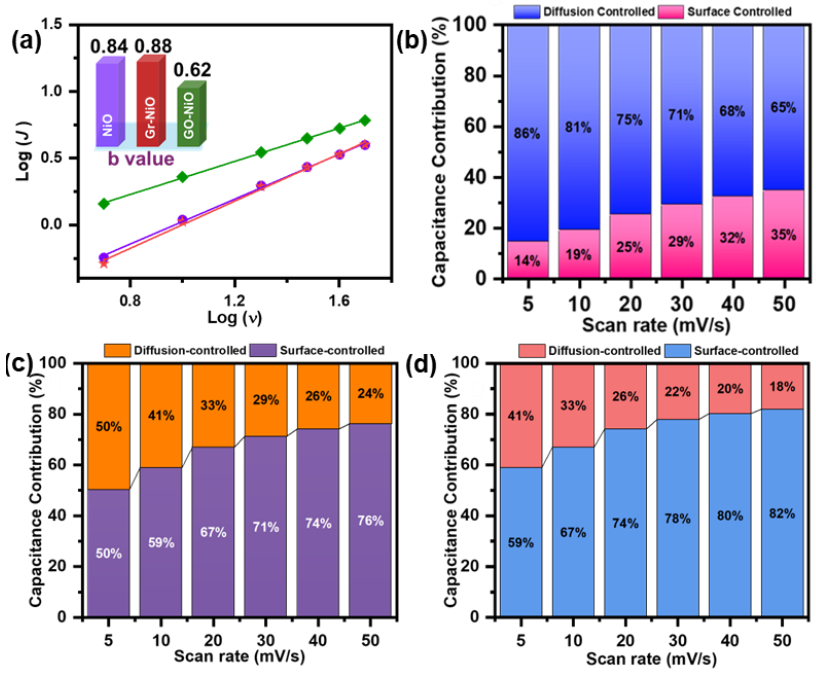

Figure 6.6:(a) logarithmic plot of the current density v/s scan rate for all the electrodes (b) capacitive contribution plot of GO-NiO electrode, (c) NiO and Gr-NiO (d)

The electrochemical impedance spectroscopy (EIS) was done to analyze the diffusion of electrolyte ions on the electrode/electrolyte interface (**Figure 6.7a**). The electrochemical impedance spectroscopy was carried out in the frequency range of 10kHz to 10mHz at 0.35V. Here, the Nyquist plot of GO-NiO electrode shows an impedance line that is more toward the real impedance axis than the NiO and Gr-NiO electrodes, indicating that dominance of diffusion-controlled type charge storage. While the Nyquist plot of NiO and Gr-NiO is more towards the imaginary impedance axis, reflecting more of a surface-controlled type charge storage mechanism, which is consistent with the above-discussed charge storage mechanism using Dunn's method. The value of solution resistance and charge transfer resistance in the higher frequency region have been evaluated (**Table 6.1**).

Table 6.1: Collective values of solution resistance (R_s) and charge transfer resistance (R_{ct}) for all three electrodes.

Electrodes	R_s (Ω)	R_{ct} (Ω)
NiO	**25**	**0.3**
Gr-NiO	**22.9**	**0.3**
GO-NiO	**45.8**	**2.1**

It is worth mentioning here that the charge transfer resistance (R_{ct}) is 0.3 Ω for NiO and Gr-NiO but its value is 2.1 Ω for GO-NiO. This difference might be due to the agglomeration of NiO over GO, resulting in less porosity.

The Galvanostatic charge-discharge (GCD) profiles of the NiO, Gr-NiO, and GO-NiO electrodes were also conducted at a current density of 0.2 mA/cm^2 (**Figure 6.7b**). On comparing, the GCD profile of the GO-NiO electrode shows the longest discharging time of 455 s with fast charging (∼196s). On the other hand, the NiO and Gr-NiO electrodes take 85.4s/49.2s and 87.1s/48.1s for discharging/charging, respectively. The GCD profile at various current densities follows the typical trend of decreasing charging/discharging time with increasing current density for all three electrodes (**Figure 6.7c-6.7e)**. In addition, the presence of a plateau in the GCD profile for all three electrodes confirms its pseudocapacitive nature. The value of specific capacitance with varying current densities, calculated using Eq. 1.3, shows a higher specific capacitance for GO-NiO electrode as compared to NiO and Gr-NiO (**Figure 6.7f)**. The maximum specific capacitance value of 38, 38.5, and 210.8 mF/cm^2 was evaluated for the NiO, Gr-NiO, and GO-NiO electrodes at 0.2 mA/cm^2, respectively. The high specific capacitance

value of the GO-NiO electrode is obtained due to the presence of more active region for the intercalation/deintercalation of ions.

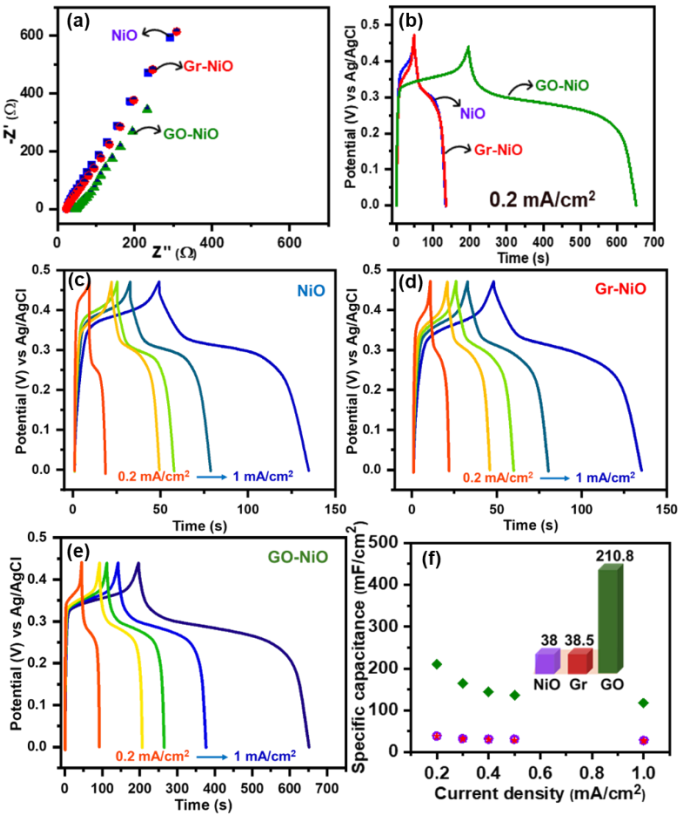

Figure 6.7: (a) EIS plot of all the electrodes, (b) comparative GCD plot of all the electrodes, GCD plot of (c) NiO, (d) Gr-NiO, (e) GO-NiO and (f) comparative specific capacitance vs current density plot of all the electrodes.

6.5 Theoretical Study of Gr-NiO and GO-NiO Interaction

To further confirm the enhanced performance of the GO-NiO electrode, a theoretical study was conducted using Gaussian software, as described in the experiment section, to understand the effect of attachment of NiO with the Gr and GO (Figure 6.8a & 6.8b). As mentioned above, in the MEP plots of Gr and GO (Figures 6.1c & 6.1d), the region for maximum attachment of NiO is at the bulk of the materials. The MEP plots of Gr-

NiO (Figure 6.8a) and GO-NiO (Figure 6.8b), show an increase in electroactive sites as compared to bare NiO (Figure 6.8c). The MEP plot of Gr-NiO and GO-NiO shows an increase in electroactive sites for GO-NiO, indicating more intercalation/deintercalation of OH- ions, resulting in high charge storage property of the GO-NiO. It is evident from the aforementioned discussion that the GO-NiO electrode is more capable of storing charge and shows slow discharging with fast charging and has a high specific capacitance.

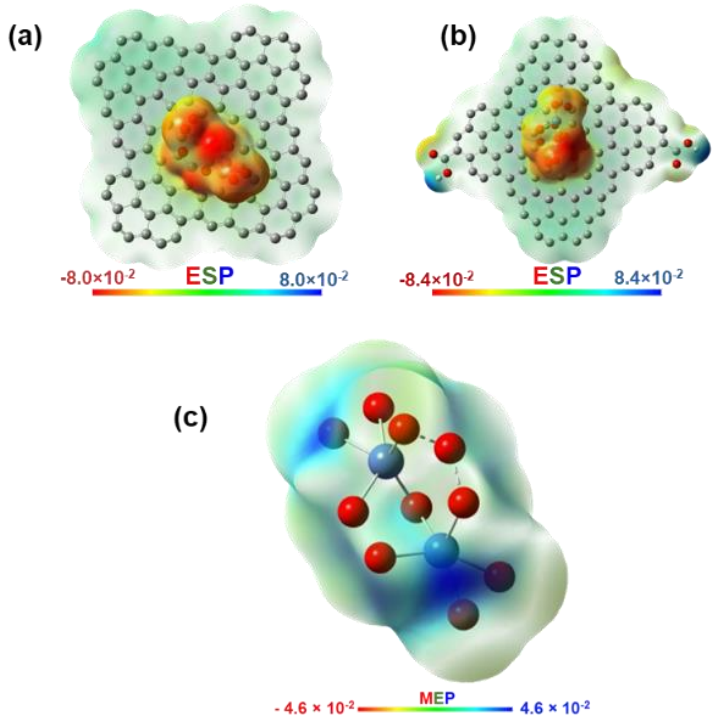

Figure 6.8: Computed ESP plots of (a) Gr- NiO, (b) GO- NiO and NiO (c).

6.6 The Fabrication of Asymmetric Supercapacitor Device.

To show the practicability in solid-state device form for real-life application, the electrodes GO-NiO and GrNiO electrodes were chosen to develop an asymmetric supercapacitor (prepared using the recipe described in section 2.5.2) in the configuration FTO/GO-NiO//AC/FTO

(GO-NiO-SCD) and FTO/Gr-NiO//AC/FTO (Gr-NiO-SCD) (**Figure 6.9**), using a solid-state separator soaked in 2M KOH.s

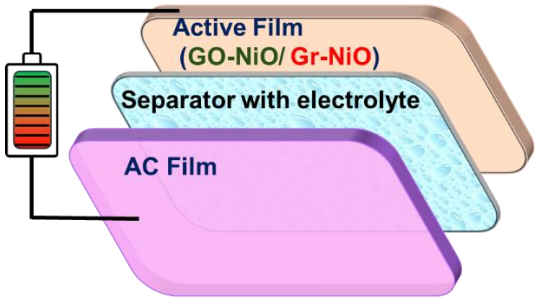

Figure 6.9: Schematic representation of asymmetric supercapacitor

6.7 Charge Storage Property of the GO-NiO-SCD and Gr-NiO-SCD

The wide and various potential windows of supercapacitor devices are a crucial factor of practical supercapacitor devices. To examine the active potential window for the fabricated asymmetric supercapacitor device of GO-NiO (say GO-NiO-SCD), the CV measurements at various potential windows (0.8 to 1.8 V) were carried out at 50 mV/s scan rate (**Figure 6.10a**). The retention of the CV curves at all potential windows shows the robust nature of the fabricated supercapacitor device. Specific capacitance values with varying potential range have been calculated (using Eq. 1.3), revealing the linear increase in specific capacitance with potential window, having a maximum specific capacitance value of 78.2 mF/cm^2 for the potential range of -0.5 to 1.8V (**Figure 6.10b**). The electrochemical performance of GO-NiO-SCD device has been evaluated with scan rate dependent CV (10 to 50 mV/s) in the active potential window of -0.5V to 1.8V (**Figure 6.10c**), The CV of the device shows the pseudocapacitive nature with a broad redox couple attributed to the change in valency of NiO because of intercalation/deintercalation of electrolyte ions into the electrode surface (**Figure 6.10c**).

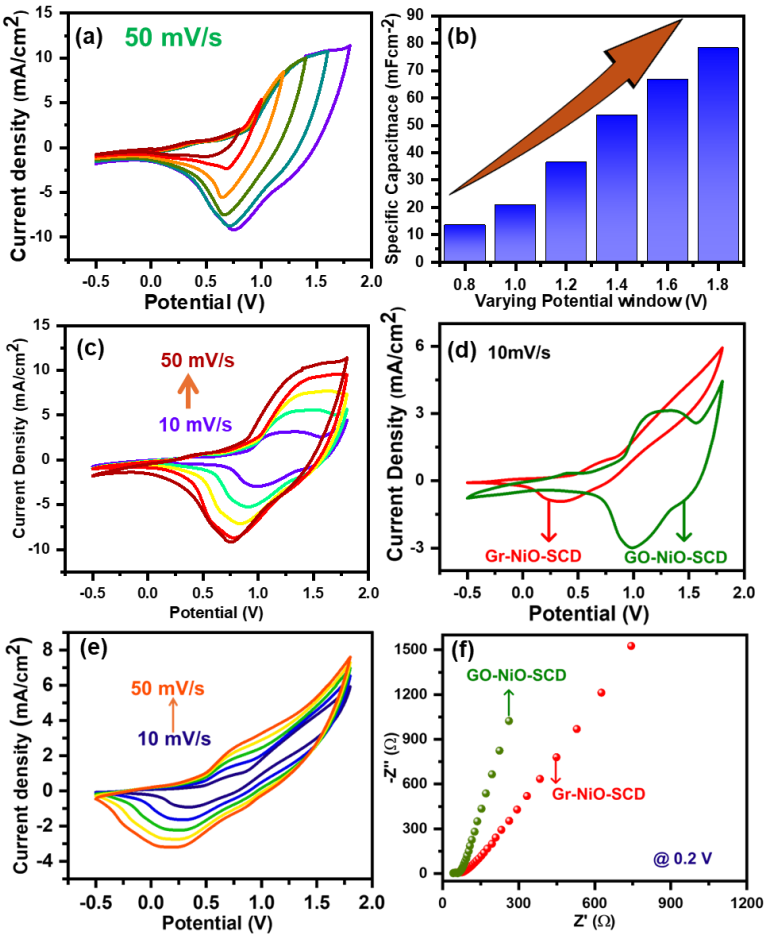

Figure 6.10: (a) CV curve of GO-NiO-SCD, (b) specific capacitance value of GO-NiO-SCD , (c) scan rate dependent CV curve of GO-NiO-SCD, (d) Comparative CV curve of Gr-NiO-SCD and GO-NiO-SCD, (e) The scan rate dependent CV curve of the Gr-NiO-SCD and (f) Comparative Nyquist plot of Gr-NiO-SCD and GO-NiO-SCD recorded at 0.2V.

As the scan rate ascends, the current density also increases, demonstrating more ion diffusion and good stability and reversibility of the GO-NiO-SCD (**Figure 6.10c**). The charge storing capacity of the GO-NiO-SCD was compared with the Gr-NiO-SCD (fabricated using the recipe mentioned in the experimental section), depicting a high area

under the CV curve, indicating significantly enhanced charge storage capacity of the GO-NiO-SCD (**Figure 6.10d**). The scan rate-dependent CV of the Gr-NiO-SCD device follows the typical trend of pseudocapacitive nature, increasing current density with increasing scan rate (**Figure 6.10e**). To further investigate the ion transport path, EIS was recorded (in frequency range of 10kHz to 10mHz at 0.2V) (**Figure 6.10f**). In the higher frequency region of the Nyquist plot, the R_s/R_{ct} values were obtained to be 42/17 Ω for GO-NiO-SCD, which is quite less than the Gr-NiO-SCD's values which were 46.5/26 Ω. In the lower frequency range, a higher slope of GO-NiO-SCD than Gr-NiO-SCD suggests fast electrolytic ions diffusion, resulting in significantly higher charge storage capacity.

To further quantify the charge storage capability, the GCD profile of the GO-NiO-SCD was studied at various current densities (3.5 mA/cm^2 to 8 mA/cm^2) in the potential range of -0.5 to 1.6 V (**Figure 6.11a**). The charging/discharging process was accompanied by a clear color change on the electrode. While charging, the color of the device changes from translucent to dark state, and on discharging, the dark state changes back to original state (inset**, Figure 6.11a**), indicating its potential application as a color indicating supercapacitor device. The comparative GCD profile of GO-NiO-SCD and Gr-NiO-SCD shows that Gr-NiO-SCD takes more time for charging and gets discharged easily (**Figure 6.11b**), implying low coulombic efficiency and specific capacitance. Whereas the GO-NiO-SCD displays high columbic efficiency with color modulating property suggests that it is highly suitable for real-world color indicating supercapacitor devices. The specific capacitance and coulombic efficiency for GO-NiO-SCD (**Figure 6.11c**) has been calculated using the Eq. 1.3 and 1.5, and a high value of 103.7 mF/cm^2 at 3.5 mA/cm^2 with almost 90 % efficiency was obtained which is much better than the other

already reported color modulating supercapacitor devices belonging to the same family (**Table 6.2**).

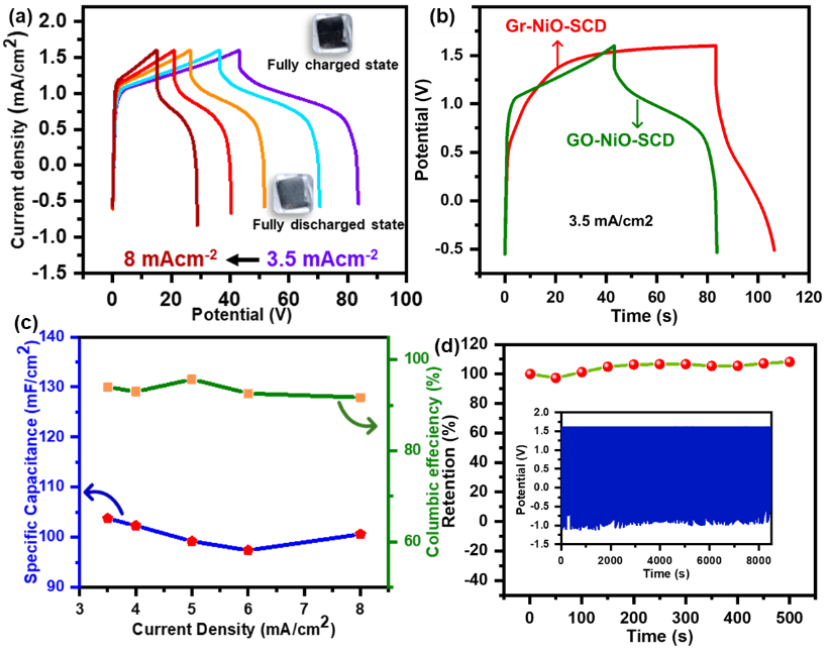

Figure 6.11: (a) GCD plot along with actual photograph of the device in corresponding charged state (inset), (b) Comparative GCD profile of Gr-NiO-SCD and GO-NiO-SCD recorded at 3.5 mA/cm^2, (c) Specific capacitance value with varying current density from GO-NiO-SCD and (d) Retention of the GO-NiO-SCD with stability up to 500 cycles (inset).

Table 6.2: Comparison table of NiO based supercapacitor devices.

S.No.	Device	Specific Capacitance (mF/cm^2)	Current density (mA/cm^2)	References.
1.	Co-doped NiO Device	10.8	0.4	Xue et al.[164]

2.	NiO/Ag NWs/Viologen	35.5	2.5	Mysoon et al.[165]
3.	Cu-doped NiO Device	14.9	0.1	Kim et al.[166]
4.	Fe_2O_3/ rGO-NiO	24.1	0.5	Xue et al.[167]
5.	**GO-NiO-SCD**	**103.7**	**3.5**	**This work.**

Furthermore, to check the capacitance retention of the GO-NiO-SCD, a continuous current density of 10 mA/cm^2 was applied and driven from the device. The GO-NiO-SCD exhibits an exceptionally high specific capacitance stability with almost 100% retention (**Figure 6.11d**) for 500 cycles (inset**, Figure 6.11d**). It is worth mentioning here that the capacitance of the device increased after a few hundred of cycles, which might be due to an increase in porosity in the GO-NiO electrode. The after-stability CV measurement of GO-NiO-SCD, retraces its curve as before stability measurements, validating its 100 % retention and robust nature of the device (**Figure 6.12a**).

To demonstrate the on-field application of GO-NiO-SCD, two large area devices (5×5 cm^2) were fabricated and connected in series to operate light emitting diode (LED). The connected devices were first charged by applying a potential of 3.8 V for a minute (**Figure 6.12b**). The device was able to illuminate red LED for a minute (**Figure 6.12c**). It is worth mentioning here that the supercapacitor modulates its color while charging and discharging (**Figure 6.12d**). It is evident from the above results that GO-NiO-SCD has huge potential for developing solid-state supercapacitor devices with color-modulating charged and discharged states.

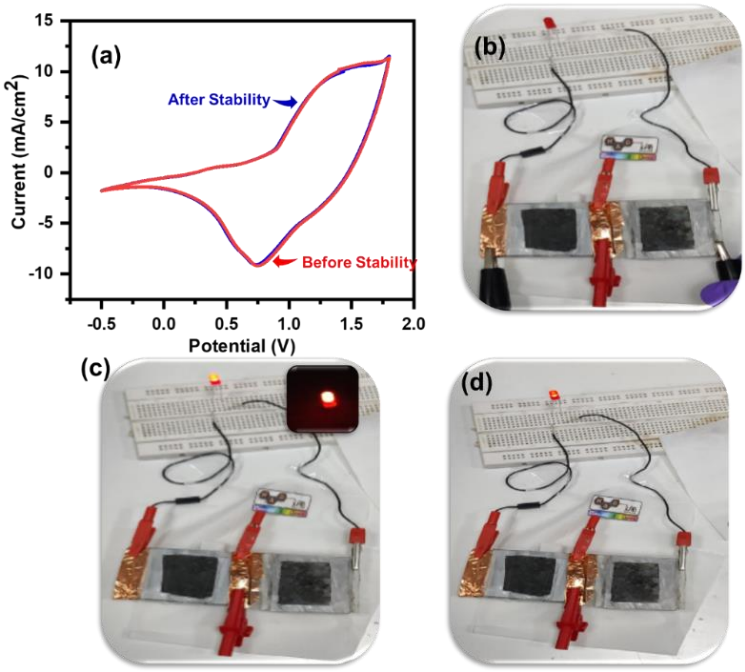

Figure 6.12: (a) The CV curve of the GO-NiO-SCD before and after stability measurements, (b) large area GO-SCD while charging, (c) while discharging through LED, (d) when 50% discharged through LED.

6.8 Optical Study of the Gr-NiO and GO-NiO Electrodes.

As seen from the MEP plots of Gr, GO, Gr-NiO, and GO-NiO, the Gr and Gr-NiO (**Figures 6.1 & 6.8**) show uniformly distributed electroactive sites all over the surface with less potential value, implying a faster intercalation and device-intercalation of electrolyte ions, which have application in electrochromism. As seen during the CV record of all the electrodes (NiO, Gr-NiO, and GO-NiO), they showed a color change between the transparent and dark state because of a change in the valence state of the NiO. To investigate it further, the optical study was conducted in three electrode setups as mentioned above, using the in-situ bias-dependent UV-Vis spectroscopy (**Figure 6.13a**).

Initially, the prepared electrode was in a transparent state due to neutral state NiO (**Figure 6.13a**), as the (positive) bias is applied to the electrodes (NiO, Gr-NiO and GO-NiO), the color of electrode turns dark

as NiO changes to NiOOH state, which is completely reversible when an opposite bias is applied (**Figure 6.13b,** inset).

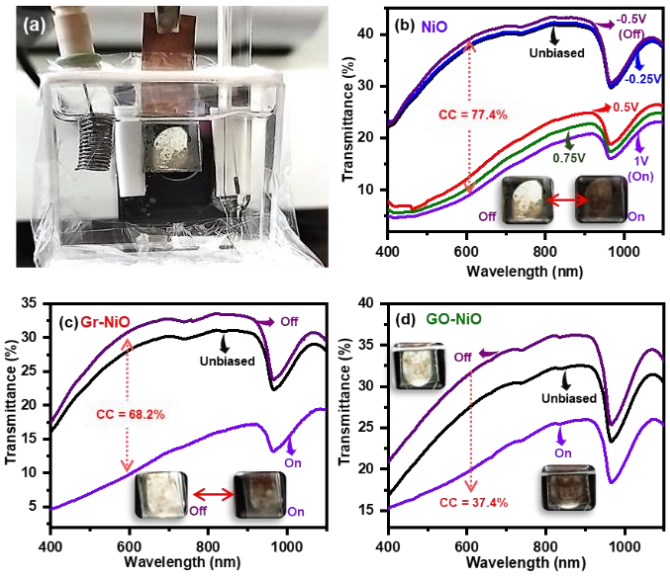

Figure 6.13: (a) Photograph of the optical measurement setup used to perform the in-situ bias dependent optical measurements of the electrodes, (b) transmittance spectra of the NiO electrode with varying applied bias, (c) transmittance spectra of Gr-NiO in unbiased, On and Off states and (d) transmittance spectra of GO-NiO in unbiased, On and Off state.

To confirm the bias-dependent color change, the applied bias was varied from -0.5V to 1V, and the corresponding transmittance was recorded. For the three electrodes, as the applied positive voltage increases gradually from 0.5 V to 1 V, the value of transmittance decreases, implying a darker state of the electrode (**Figures 6.13b-6.13d**). The maximum change in transmittance value was seen at 600 nm between the bias -0.5V ("Off" state) and 1V ("On" state), hence the crucial electrochromic parameters like color contrast (CC) was calculated at 600 nm using Eq. 1.1. The CC was found to be 77.4 %, 68.2 % and 37.4 % for NiO, Gr-NiO, and GO-NiO electrodes, respectively at 600 nm

wavelength. A lower CC value for Gr-NiO and GO-NiO, in comparison with NiO, is seen due to the doping of dark material (Gr and GO). Afterwards, another important factor, switching time, was investigated to calculate the color switching speed of the electrode between transparent and dark states (90% of total change in state), by applying a square pulse of 1V and -0.5V of 5s each. The very fast switching with a switching time of 0.8 s was observed in the Gr-NiO electrode for coloration (T_c: time required to switch from transparent to dark state, colored state) and 0.9s for bleaching (T_b: time required to switch from dark to transparent state, bleaching state) (**Figure 6.14a**). On the other hand, the NiO (**Figure 6.14b**) and GO-NiO (**Figure 6.14c**) electrodes took 1/ 2.9s and 1.6/5.1s for coloration/bleaching (T_c/ T_b), respectively, which is quite slow as compared to the Gr-NiO electrode.

The reason for fast switching of the Gr-NiO electrode is, the maximum electrons are only interacting at the surface of the electrode (high surface-controlled mechanism, b= 0.88, as discussed above in electrochemistry of electrode), as well as due to the low MEP potentials of Gr, and Gr-NiO as compared to GO and GO-NiO. But in the case of GO-NiO electrode, the switching time is quite low as the electrons need more time to go to the bulk of the electrode (diffusion-controlled mechanism b=0.62), while for NiO, the switching time is intermediate to that for Gr-NiO and GO-NiO electrode as the value of b is in between the two (b= 0.84 for NiO). The electrochromic switching stability of the electrode was also examined by continuously toggling the voltages between 1V and -0.5V (of 5 s each) for 100 cycles. All of the GO-NiO (**Figure 6.14d**), NiO (**Figure 6.14e**), and Gr-NiO (**Figure 6.14f**) electrodes exhibited good electrochromic stability, whereas the GO-NiO electrodes demonstrated comparatively higher stability by constantly retaining the transmittance value in both the On and Off states due to slow movement or proper diffusion of electrons.

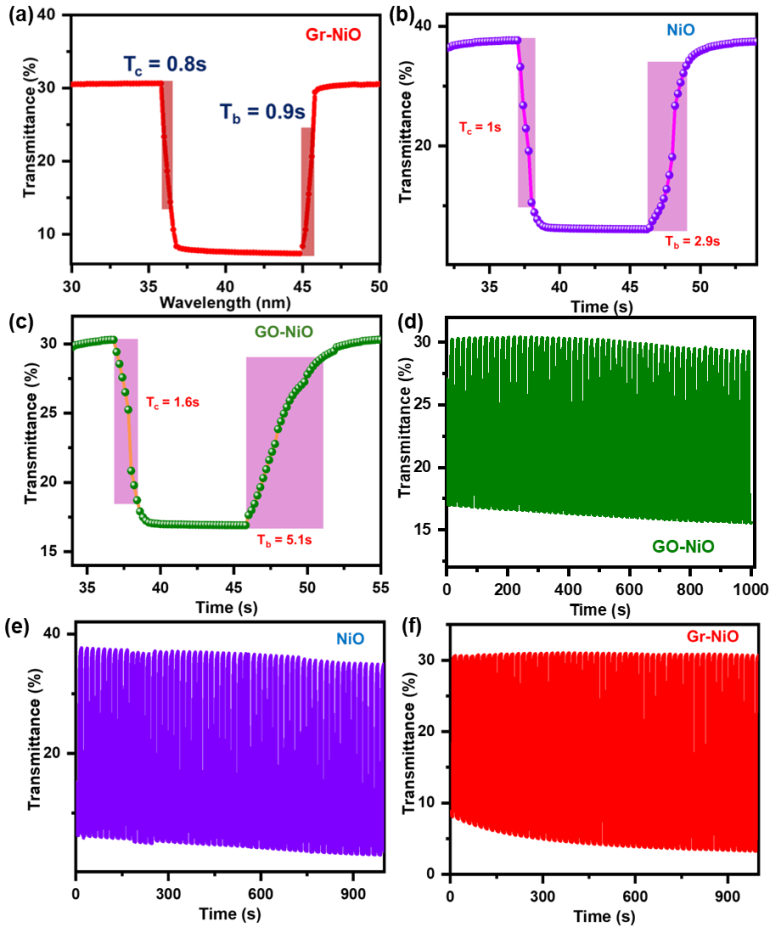

Figure 6.14: (a) Single switching cycle of the Gr-NiO electrode showing fast switching, the single switching cycle of the (b) NiO and GO-NiO electrodes (c), (d) electrochromic stability of the GO-NiO electrode, The switching stability of the (e) NiO and Gr-NiO electrodes (f).

It is evident from the above discussion that the Gr-NiO electrode demonstrates great potential for electrochromic application due to fast switching of color state (transparent to dark and vice-versa) and good stability which are accompanied by the surface-controlled mechanism. On the other hand, for supercapacitor application the GO-NiO electrode is more suitable as it has diffusion-controlled mechanism, and it is reflected in an excellent charge storage capacity of ∼211 mF/cm^2. Overall, the above discussion suggests how the effect of different carbonaceous

materials can be augmented to design a device for application in electrochromic smart windows and/or a supercapacitor with latter having a color indicative feature if designed appropriately. A multifunctional electrochromic supercapacitor can be designed by appropriately choosing a carbonaceous dopant vis-e-vis graphene or graphene oxide.

6.9 Summary and Conclusion

The Incorporation of carbon-based materials such as graphene (Gr) and graphene oxide (GO) into NiO nanograins provides an efficient strategy for developing multifunctional electrochromic supercapacitors with color-indicative behavior. DFT studies reveal that GO possesses more electroactive sites, enabling efficient ion intercalation and de-intercalation, making it ideal for energy storage applications. In contrast, Gr shows surface-controlled diffusion suitable for electrochromic performance. Experimentally, the GO–NiO electrode exhibits a diffusion-controlled mechanism with a high areal capacitance of 211 mF cm^{-2} at 0.2 mA cm^{-2} and excellent color modulation. The asymmetric solid-state supercapacitor fabricated using GO–NiO retains its capacitance with stable color switching and successfully illuminates a red LED when two large area devices are connected in series. Meanwhile, the Gr–NiO electrode shows superior electrochromic behavior with a high color contrast of 68%, sub-second switching time, and good cyclic stability. Overall, this study highlights that through appropriate material incorporation, NiO-based systems can be tailored for specific applications, either high-capacitance energy storage devices or fast-switching electrochromic windows.

Chapter 7

Conclusions and Future Scope

This chapter outlines the main conclusion drawn from the research work reported in the thesis. Additionally, the scope for future extension of the work has also been highlighted.

7.1 Conclusion & Summary

7.1.1 Highly Flexible Asymmetric All-Organic ECDs

- A solid state flexible electrochromic device (flex-ECD) device which not only is flexible but also can exhibit color switching with great efficiency after it is folded and twisted has been demonstrated here.
- The flex-ECD shows high stability with a few seconds of switching time and high coloration efficiency of 420 cm^2/C. The flex-ECD devices show color switching in multiple wavelength regions
- The device shows excellent stability even after bending and twisting moments making it a good design for future wearable electronics. The proposed design can be used to develop wearable smart sensors for future technology integration.
- The WS_2/WO_3 nanoflakes complex structure has been fabricated using a simple hydrothermal technique.
- The doping of WS_2/WO_3 in EV-P3HT based device has accelerated the redox reaction, which speeds up the switching dynamics of the device in NIR and visible region to achieve a switching time of 500 ms.
- The device shows an optical modulation of up to 60% and a high coloration efficiency of 192 cm^2/C.
- The device shows high cyclic stability at both the NIR and visible spectrum with no change in the ΔA value throughout the cycle

- The fully flexible- NIR cutting-electrochromic device (flex-NIR cutting-ECD) shows high NIR shielding by maintaining a temperature difference of upto 6° C and cuts more than 15% of the heat when in ON state.
- A prototype device has been fabricated goggle-like structure which demonstrates heat soothing effect to the eyes. When a 3V bias is applied, the goggle glass starts cutting heat.
- The flexible smart window with reduced energy usage and heat filtering properties can be designed which will reduce the need for air conditioning in smart buildings.

7.1.2 MXene-Based Asymmetric All-Organic Multifunctional Electrochromic Supercapacitor

- The 2-Dimensional MXene, synthesized using selective etching method, was doped in an electrochromic device fabricated using a junction of Ethyl Viologen (EV), an n-type layer, and poly-3-hexylthiophene (P3HT), a p-type layer.
- MXene nano sheets prepared using selective etching method was incorporated into EV/ P3HT n-p junction based electrochromic device enables it for multifunctional operation with not only enhancing electrochromic color modulation but also a color indicative supercapacitor.
- The electrochromic supercapacitor was designed by using MXene doped EV and P3HT (M-doped ESD) as the two complementary components shows reversibly in visible as well as NIR region making it suitable for smart window application.
- The prepared device gives high optical contrast (~85%) and coloration efficiency (~340cm^2/C) with ~1 s of switching time in the visible spectrum at 515 nm.

- The M-doped-ESD displays supercapacitor application as it shows fast charging and slow discharging with moderate specific capacitance value of 1.3mF/cm^2 and high Columbic efficiency.
- Overall, mixing 2-D MXene nano sheets in electrochromic devices shows excellent enhancement in electrochromic supercapacitive performance with heat filtering properties which can be utilized further in real life applications.
- Overall the above-mentioned study provides a path to design electrochromic supercapacitors for energy saving and energy storage smart windows.

7.1.3 Perovskite-Based Asymmetric Organic-Inorganic Electrochromic Supercapacitor Device

- A multifunctional device has been made using nano $CoTiO_3$ mixed conducting polymer and WO_3 to obtain good super capacitive nature along with excellent electrochromic properties.
- The device shows discharging time of 44.5 s and charging time of 8s at 0.2 mA/cm^2 giving high coulombic efficiency, with the maximum specific capacitance 6.4 mF/cm^2 at 0.2 mA/cm^2.
- The as-fabricated solid state asymmetric ESCD shows switching in three different wavelengths (515 nm, 700 nm & 850 nm) switching between magenta to dark blue under an external bias.
- Overall, mixing charge storage material in electrochromic devices shows excellent enhancement in electrochromic supercapacitive performance with heat filtering properties which can be utilized further in real life applications.
- Overall, the above-mentioned study provides a path to design electrochromic supercapacitors for energy saving and energy storage smart windows.

7.1.4 Carbon Materials Based Asymmetric Electrochromic Supercapacitor Devices

- The pre-optimized nano-flakes of Graphene (Gr) and Graphene Oxide (GO) using Gaussian Software 09, were used as dopant in the nanogranular NiO film to fabricate electrodes for color indicative EC supercapacitor and later a prototype device also has been fabricated.
- A very straightforward spin-coating technique with slight modifications in the preparation of precursor solutions was adopted for developing electrodes.
- Fully validated experimentally, the GO-NiO electrode shows a diffusion- controlled mechanism, with a high charge storage capacity of 211 mF/cm^2 at 0.2 mA/cm^2, and color-modulating properties due to more availability of surface sites confirmed using the DFT calculation.
- The energy storage capability remains intact even when an asymmetric solid-state supercapacitor is fabricated using GO-NiO electrode, exhibiting a high specific capacitance value of ∼105 mF/cm^2 with 100 % capacitance retention and coherent color-modulating properties.
- The large area prototype device of GO-NiO-SCD, when connected in series, was able to glow a red LED, thus demonstrating its on-field application.
- On the other hand, the Gr-NiO electrode demonstrated a surface-controlled mechanism, as also depicted from MEP plots of Gr and Gr-NiO, showing faster switching of less than a second to switch between colored and bleached states.
- This study provides a path for designing high-capacitance supercapacitor device and fast fast-switching EC window which can be achieved by a simple method, doping the appropriate material specific to a given application.

7.2 New Findings Reported in the Thesis

- A super flexible electrochromic device with bending and twisting capabilities has been demonstrated from a prototype device fabricated using metal oxide doped organic layers on a PET substrate.
- The doping of tungsten chalcogenide-oxide mixture (WS_2/WO_3) in EV and P3HT for heat filtering applications and to enhance the electrochromic performance of the device.
- Thermal imaging investigations show that the designed flex-NIR cutting-ECD can maintain a difference of 6°C on the two sides of the device giving a heat soothing effect if used as googles which also can be extended for such heat isolation applications.
- The addition of MXene nano sheets adds supercapacitive property to the p-n junction-based device that can get integrated with electrochromic device to yield an enhanced capacitive performance. A prototype device has been prepared to establish a more suitable real-life application.
- The addition of nano cobalt titanate adds pseudocapacitive nature to the device that can get integrated with electrochromic device to yield an enhanced capacitive performance. A prototype device has been prepared to establish a more suitable real-life application.
- The tailored carbon doping in NiO unveils distinct charge storage mechanisms, empowering multifunctional devices that seamlessly merge energy storage with real-world electrochromic applications thus giving a color indicative electrochromic supercapacitor for smart building applications.

7.3 Future Scope of the Work

The research work carried out in this thesis can be further extended in the following directions in the future.

- To design the appropriate metal-organic and covalent-organic frameworks for efficient EC displays.

- Exploring new materials and making composites or core shell for improved EC performance.
- Adding other 2-D materials / perovskite to understand the effect of morphology, electrical and electrochemical property to further improve performance of ECD.
- To perform the in-situ spectro-electrochemical performances to study the charge transfer kinetic and color switching mechanism in multifunctional EC displays.
- To gain deeper knowledge out the nano and micro structured materials for charge storage application with improved specific capacitance value.
- To study the other functionalities of EC in biosensors, batteries, Solar cells, and camouflage.
- To design super-flexible devices by exploring and incorporating different types of polymers with enhanced mechanical strength.
- To fabricate super-flexible devices possessing efficient charge storage capabilities by integrating different or exploring new materials that offer high mechanical stability, with superior electrochemical performance.
- Making multifunctional ECDs with multiwavelength switching by fabricating core shell or by making composite materials.
- To test the temperature and mechanical stability of large area EC displays for commercialization.

Appendix

Herbal amalgam as yellow LED glow.

"Herbal electronics" is an emerging field that explores the optical and electrical properties of herbal materials for electronic applications. In this study, turmeric and henna extracts were investigated using absorption and luminescence spectroscopy. The solutions exhibit red and green emissions under UV excitation, which combine to produce yellow light. Color coordinates were analyzed using the CIE diagram, and photoluminescence quantum yields were calculated. A simple setup using a 400 nm blue LED demonstrated yellow emission with a quantum yield of ~5%.

(Sahu. B. et al., ChemistrySelect 2023, 8, e202204265)

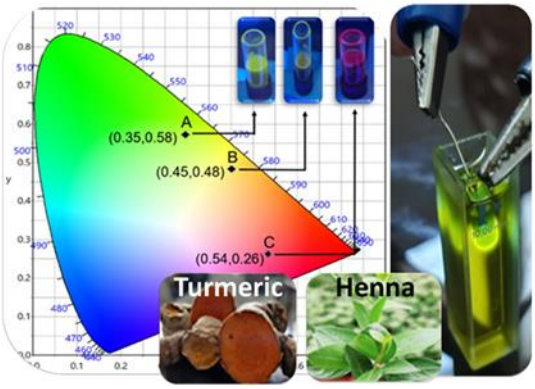

Figure A3: CIE coordinates showing the coordinates of henna extract (C), Turmeric extract (A) and the mixture of extracts in 1:1 (B) with Blue LED as a source glowing yellow in the mixture of extracts.

References

[1] R. Feynman, There's Plenty of Room at the Bottom, in: Feynman Comput., CRC Press, 2002.

[2] S. Srivastava, A. Bhargava, Green Nanotechnology: An Overview, in: S. Srivastava, A. Bhargava (Eds.), Green Nanoparticles Future Nanobiotechnology, Springer, Singapore, 2022: pp. 1–13. https://doi.org/10.1007/978-981-16-7106-7_1.

[3] C.G. Granqvist, Electrochromism and smart window design, Solid State Ion. 53–56 (1992) 479–489. https://doi.org/10.1016/0167-2738(92)90418-O.

[4] P.M.S. Monk, R.J. Mortimer, D.R. Rosseinsky, Electrochromism: Fundamentals and Applications, John Wiley & Sons, 2008.

[5] S.K. Deb, Opportunities and challenges in science and technology of WO3 for electrochromic and related applications, Sol. Energy Mater. Sol. Cells 92 (2008) 245–258. https://doi.org/10.1016/j.solmat.2007.01.026.

[6] P.M.S. Monk, R.J. Mortimer, D.R. Rosseinsky, Electrochromism: Fundamentals and Applications, John Wiley & Sons, 2008.

[7] C.G. Granqvist, Electrochromism And Electrochromic Devices, in: Handb. Solid State Electrochem., CRC Press, 1997.

[8] K.J. Patel, G.G. Bhatt, J.R. Ray, P. Suryavanshi, C.J. Panchal, All-inorganic solid-state electrochromic devices: a review, J. Solid State Electrochem. 21 (2017) 337–347. https://doi.org/10.1007/s10008-016-3408-z.

[9] T. A. Welsh, E. R. Draper, Water soluble organic electrochromic materials, RSC Adv. 11 (2021) 5245–5264. https://doi.org/10.1039/D0RA10346B.

[10] A. Piccolo, F. Simone, Performance requirements for electrochromic smart window, J. Build. Eng. 3 (2015) 94–103. https://doi.org/10.1016/j.jobe.2015.07.002.

[11] A. M. Österholm, L. Nhon, D. Eric Shen, A. M. Dejneka, A. L. Tomlinson, J. R. Reynolds, Conquering residual light absorption in the transmissive states of organic electrochromic materials, Mater. Horiz. 9 (2022) 252–260. https://doi.org/10.1039/D1MH01136G.

[12] A. Chaudhary, M. Poddar, D.K. Pathak, R. Misra, R. Kumar, Electron Donor Ferrocenyl Phenothiazine: Counter Ion for Improving All-Organic Electrochromism, ACS Appl. Electron. Mater. 2 (2020) 2994–3000. https://doi.org/10.1021/acsaelm.0c00606.

[13] R. Kumar, D.K. Pathak, A. Chaudhary, Current status of some electrochromic materials and devices: a brief review, J. Phys. Appl. Phys. 54 (2021) 503002. https://doi.org/10.1088/1361-6463/ac10d6.

[14] Q. Zhao, J. Yang, Q. Wang, Y.-W. Zhang, J. Wang, 2D Conjugated Metal-Organic Frameworks for New Generation Flexible Multicolor Electrochromic Devices, Adv. Mater. 37 (2025) 2413452. https://doi.org/10.1002/adma.202413452.

[15] G. Kumar Silori, S.-C. Chien, L.-C. Lin, K.-C. Ho, Four-State Electrochromism in Tris(4-aminophenyl)amine-terephthalaldehyde-based Covalent Organic Framework, Angew. Chem. 137 (2025) e202416046. https://doi.org/10.1002/ange.202416046.

[16] Q. Chen, Y. Zhang, C. Tian, S. Xiong, The influence of building block length on the electrochemical and electrochromic properties of triphenylamine based covalent organic framework, J. Mater. Sci. 60 (2025) 9208–9219. https://doi.org/10.1007/s10853-025-10998-0.

[17] T. Charbonnel, C.T. Prontera, M. Pugliese, S. Di Masi, A. Giuri, A. Cannavale, U. Ayr, A. Maggiore, F. Mariano, G. Gigli, L. De Marco, A. Rizzo, V. Maiorano, Multifunctional thermo-electrochromic devices based on 2D perovskite gel electrolyte, Nano Energy 142 (2025) 111271. https://doi.org/10.1016/j.nanoen.2025.111271.

[18] H. Zhou, H. Kang, H.J. Lee, S. Kwon, G.H. Kim, S. Oh, E.J. Kim, C.W. Byun, S. Jung, J.W. Jung, T.H. Park, Y. Kim, S.H. Kang, Porphyrin-based interface engineering for enhanced perovskite solar cells and application in powering electrochromic devices, Mater. Today Energy 53 (2025) 101980. https://doi.org/10.1016/j.mtener.2025.101980.

[19] B. Sahu, M.K. Singh, L. Bansal, D.K. Rath, D.K. Rai, R. Kumar, Ti3C2Tx-MXene-Based Color-Indicative All-Organic Electrochromic Supercapacitors, Adv. Eng. Mater. 26 (2024) 2401295. https://doi.org/10.1002/adem.202401295.

[20] J. Huang, S. Zhang, Q. Qin, Z. Wang, G. Cai, Designing V2O5/MXene van der Waals heterostructure for complementary electrochromic dual-ion capacitor, Chem. Eng. J. 476 (2023) 146626. https://doi.org/10.1016/j.cej.2023.146626.

[21] E. Roduner, Size matters: why nanomaterials are different, Chem. Soc. Rev. 35 (2006) 583–592. https://doi.org/10.1039/B502142C.

[22] S. Deng, Z. Tie, F. Yue, H. Cao, M. Yao, Z. Niu, Rational Design of $ZnMn_2O_4$ Quantum Dots in a Carbon Framework for Durable Aqueous Zinc-Ion Batteries, Angew. Chem. 134 (2022) e202115877. https://doi.org/10.1002/ange.202115877.

[23] Aashi, R. Rani, S. Alagar, J. Sharma, A. k, V. Bagchi, Laser-Induced Crafting of Modulated Structural Defects in MOF-Based Supercapacitor for Energy Storage Application, ACS Mater. Lett. (2024) 1769–1778. https://doi.org/10.1021/acsmaterialslett.4c00206.

[24] U. Rajaji, P.-S. Ganesh, S.-Y. Kim, M. Govindasamy, R.A. Alshgari, T.-Y. Liu, MoS2 Sphere/2D S-Ti3C2 MXene Nanocatalysts on Laser-

Induced Graphene Electrodes for Hazardous Aristolochic Acid and Roxarsone Electrochemical Detection, ACS Appl. Nano Mater. 5 (2022) 3252–3264. https://doi.org/10.1021/acsanm.1c03680.

[25] S.K. Saxena, V. Kumar, H.M. Rai, G. Sahu, R. Late, K. Saxena, A.K. Shukla, P.R. Sagdeo, R. Kumar, Study of Porous Silicon Prepared Using Metal-Induced Etching (MIE): a Comparison with Laser-Induced Etching (LIE), Silicon 9 (2017) 483–488. https://doi.org/10.1007/s12633-014-9242-y.

[26] J.-S. Lee, S.-I. Kim, J.-C. Yoon, J.-H. Jang, Chemical Vapor Deposition of Mesoporous Graphene Nanoballs for Supercapacitor, ACS Nano 7 (2013) 6047–6055. https://doi.org/10.1021/nn401850z.

[27] L. Merabet, K. Rida, N. Boukmouche, Sol-gel synthesis, characterization, and supercapacitor applications of MCo2O4 (M = Ni, Mn, Cu, Zn) cobaltite spinels, Ceram. Int. 44 (2018) 11265–11273. https://doi.org/10.1016/j.ceramint.2018.03.171.

[28] B. Pandit, E.S. Goda, M.H. Abu Elella, A. ur Rehman, S. Eun Hong, S.R. Rondiya, P. Barkataki, S.F. Shaikh, A.M. Al-Enizi, S.M. El-Bahy, K. Ro Yoon, One-pot hydrothermal preparation of hierarchical manganese oxide nanorods for high-performance symmetric supercapacitors, J. Energy Chem. 65 (2022) 116–126. https://doi.org/10.1016/j.jechem.2021.05.028.

[29] T. Ghosh, L. Bansal, S. Kandpal, C. Rani, M. Tanwar, R. Kumar, Ambipolar All-Organic Solid-State Electrochromic Device Using Electrodeposited Polyaniline: Improving Performance by Design, ACS Appl. Opt. Mater. 1 (2023) 473–480. https://doi.org/10.1021/acsaom.2c00115.

[30] B. Sahu, L. Bansal, N. Ahlawat, A. Ghanghass, D.K. Rath, S. Kaladi Chondath, S. Kandpal, R. Bhatia, I. Sameera, R. Kumar, Mixed Chalcogenides Nanoflakes' Infrared Cutting Effect: Utilization in Thermal Soothing Electrochromic Goggles, ACS Appl. Opt. Mater. 2 (2024) 2128–2136. https://doi.org/10.1021/acsaom.4c00325.

[31] B. Sahu, L. Bansal, N. Ahlawat, A. Ghanghass, D.K. Rath, S. Kaladi Chondath, S. Kandpal, R. Bhatia, I. Sameera, R. Kumar, Mixed Chalcogenides Nanoflakes' Infrared Cutting Effect: Utilization in Thermal Soothing Electrochromic Goggles, ACS Appl. Opt. Mater. (2024). https://doi.org/10.1021/acsaom.4c00325.

[32] H. Fan, W. Wei, C. Hou, Q. Zhang, Y. Li, K. Li, H. Wang, Wearable electrochromic materials and devices: from visible to infrared modulation, J. Mater. Chem. C 11 (2023) 7183–7210. https://doi.org/10.1039/D3TC01142A.

[33] S. Kandpal, L. Bansal, O.S. Game, R. Kumar, Self-Sufficient Electrochromic Solar Cells: Photovoltaic and Color Modulating Smart Windows, ACS Appl. Mater. Interfaces 17 (2025) 2703–2715. https://doi.org/10.1021/acsami.4c17552.

[34] D.K. Pathak, A. Chaudhary, M. Tanwar, U.K. Goutam, P. Mondal, R. Kumar, Nickel Cobalt Oxide Nanoneedles for Electrochromic Glucose Sensors, ACS Appl. Nano Mater. 4 (2021) 2143–2152. https://doi.org/10.1021/acsanm.0c03451.

[35] Y. Su, B. Yu, X. Zhao, Research status and development of infrared camouflage textile materials, Text. Res. J. 93 (2023) 5047–5082. https://doi.org/10.1177/00405175231170323.

[36] A. Chaudhary, Inorganic-Alone Solid-State Electrochromic Device for Application as Visible Near Infrared Region Electronic Curtain, Phys. Status Solidi A 219 (2022) 2200524. https://doi.org/10.1002/pssa.202200524.

[37] N.I. Jalal, R.I. Ibrahim, M.K. Oudah, A review on Supercapacitors: types and components, J. Phys. Conf. Ser. 1973 (2021) 012015. https://doi.org/10.1088/1742-6596/1973/1/012015.

[38] L. Bansal, B. Sahu, D.K. Rath, N. Ahlawat, T. Ghosh, S. Kandpal, R. Kumar, Stoichiometrically Optimized Electrochromic Complex [V2O2+ξ(OH)3-ξ] Based Electrode: Prototype Supercapacitor with Multicolor Indicator, Small 20 (2024) 2312215. https://doi.org/10.1002/smll.202312215.

[39] X. He, Q. Liu, J. Liu, R. Li, H. Zhang, R. Chen, J. Wang, High-performance all-solid-state asymmetrical supercapacitors based on petal-like NiCo2S4/Polyaniline nanosheets, Chem. Eng. J. 325 (2017) 134–143. https://doi.org/10.1016/j.cej.2017.05.043.

[40] L. Bansal, C. Rani, T. Ghosh, S. Kandpal, S. Chhoker, M. Tanwar, R. Kumar, Mescoporous Nickel Titanate–Titanium Oxide Complex Material for Enhanced Energy Storage Application, J. Phys. Chem. C 127 (2023) 8925–8936. https://doi.org/10.1021/acs.jpcc.3c00883.

[41] T. Thilagavathi, D. Venugopal, D. Thangaraju, R. Marnadu, B. Palanivel, M. Imran, M. Shkir, M. Ubaidullah, S. AlFaify, A facile co-precipitation synthesis of novel WO3/NiWO4 nanocomposite with improved photocatalytic activity, Mater. Sci. Semicond. Process. 133 (2021) 105970. https://doi.org/10.1016/j.mssp.2021.105970.

[42] R. Huirache-Acuña, F. Paraguay-Delgado, M.A. Albiter, J. Lara-Romero, R. Martínez-Sánchez, Synthesis and characterization of WO3 nanostructures prepared by an aged-hydrothermal method, Mater. Charact. 60 (2009) 932–937. https://doi.org/10.1016/j.matchar.2009.03.006.

[43] T. Ghosh, C. Rani, S. Kandpal, M. Tanwar, L. Bansal, R. Kumar, Chronoamperometric deposition of transparent WO3 film for application as power efficient electrochromic auxiliary electrode, J. Phys. Appl. Phys. 55 (2022) 365103. https://doi.org/10.1088/1361-6463/ac76f5.

[44] M. Downes, C.E. Shuck, B. McBride, J. Busa, Y. Gogotsi, Comprehensive synthesis of Ti3C2Tx from MAX phase to MXene,

Nat. Protoc. 19 (2024) 1807–1834. https://doi.org/10.1038/s41596-024-00969-1.
[45] N.I. Zaaba, K.L. Foo, U. Hashim, S.J. Tan, W.-W. Liu, C.H. Voon, Synthesis of Graphene Oxide using Modified Hummers Method: Solvent Influence, Procedia Eng. 184 (2017) 469–477. https://doi.org/10.1016/j.proeng.2017.04.118.
[46] M. Kaur, H. Kaur, D. Kukkar, Synthesis and characterization of graphene oxide using modified Hummer's method, AIP Conf. Proc. 1953 (2018) 030180. https://doi.org/10.1063/1.5032515.
[47] A. Chaudhary, D.K. Pathak, S. Mishra, P. Yogi, P.R. Sagdeo, R. Kumar, Polythiophene -viologen bilayer for electro-trichromic device, Sol. Energy Mater. Sol. Cells 188 (2018) 249–254. https://doi.org/10.1016/j.solmat.2018.08.029.
[48] C.I. Priyadharsini, G. Marimuthu, T. Pazhanivel, P.M. Anbarasan, V. Aroulmoji, V. Siva, L. Mohana, Sol–Gel synthesis of Co3O4 nanoparticles as an electrode material for supercapacitor applications, J. Sol-Gel Sci. Technol. 96 (2020) 416–422. https://doi.org/10.1007/s10971-020-05393-x.
[49] M. Jamali, F. Shariatmadar Tehrani, Effect of synthesis route on the structural and morphological properties of WO3 nanostructures, Mater. Sci. Semicond. Process. 107 (2020) 104829. https://doi.org/10.1016/j.mssp.2019.104829.
[50] Q. Liu, X. Li, Z. Xiao, Y. Zhou, H. Chen, A. Khalil, T. Xiang, J. Xu, W. Chu, X. Wu, J. Yang, C. Wang, Y. Xiong, C. Jin, P.M. Ajayan, L. Song, Stable Metallic 1T-WS2 Nanoribbons Intercalated with Ammonia Ions: The Correlation between Structure and Electrical/Optical Properties, Adv. Mater. 27 (2015) 4837–4844. https://doi.org/10.1002/adma.201502134.
[51] L. Wang, K. Wang, R. Huang, Z. Qin, Y. Su, S. Tong, Hierarchically flower-like WS2 microcrystals for capture and recovery of Au (III), Ag (I) and Pd (II), Chemosphere 252 (2020) 126578. https://doi.org/10.1016/j.chemosphere.2020.126578.
[52] M.R. Pallavolu, N. Gaddam, A.N. Banerjee, R.R. Nallapureddy, Y.A. Kumar, S.W. Joo, Facile construction and controllable design of CoTiO3@Co3O4/N CNO hybrid heterojunction nanocomposite electrode for high-performance supercapacitors, Electrochimica Acta 407 (2022) 139868. https://doi.org/10.1016/j.electacta.2022.139868.
[53] M.K. Singh, S. Krishnan, D.K. Rai, Rational design of Ti3C2Tx MXene coupled with hierarchical CoS for a flexible supercapattery, Electrochimica Acta 441 (2023) 141825. https://doi.org/10.1016/j.electacta.2023.141825.
[54] M. Alhabeb, K. Maleski, B. Anasori, P. Lelyukh, L. Clark, S. Sin, Y. Gogotsi, Guidelines for Synthesis and Processing of Two-Dimensional Titanium Carbide (Ti3C2Tx MXene), Chem. Mater. 29

(2017) 7633–7644. https://doi.org/10.1021/acs.chemmater.7b02847.

[55] F.T. Johra, J.-W. Lee, W.-G. Jung, Facile and safe graphene preparation on solution based platform, J. Ind. Eng. Chem. 20 (2014) 2883–2887. https://doi.org/10.1016/j.jiec.2013.11.022.

[56] T. Ghosh, C. Rani, S. Kandpal, M. Tanwar, L. Bansal, R. Kumar, Chronoamperometric deposition of transparent WO3 film for application as power efficient electrochromic auxiliary electrode, J. Phys. Appl. Phys. 55 (2022) 365103. https://doi.org/10.1088/1361-6463/ac76f5.

[57] G. Cai, X. Wang, M. Cui, P. Darmawan, J. Wang, A.L.-S. Eh, P.S. Lee, Electrochromo-supercapacitor based on direct growth of NiO nanoparticles, Nano Energy 12 (2015) 258–267. https://doi.org/10.1016/j.nanoen.2014.12.031.

[58] A.M. Soleimanpour, A.H. Jayatissa, G. Sumanasekera, Surface and gas sensing properties of nanocrystalline nickel oxide thin films, Appl. Surf. Sci. 276 (2013) 291–297. https://doi.org/10.1016/j.apsusc.2013.03.085.

[59] K.D. Vernon-Parry, Scanning electron microscopy: an introduction, III-Vs Rev. 13 (2000) 40–44. https://doi.org/10.1016/S0961-1290(00)80006-X.

[60] C.Y. Tang, Z. Yang, Chapter 8 - Transmission Electron Microscopy (TEM), in: N. Hilal, A.F. Ismail, T. Matsuura, D. Oatley-Radcliffe (Eds.), Membr. Charact., Elsevier, 2017: pp. 145–159. https://doi.org/10.1016/B978-0-444-63776-5.00008-5.

[61] J. Epp, 4 - X-ray diffraction (XRD) techniques for materials characterization, in: G. Hübschen, I. Altpeter, R. Tschuncky, H.-G. Herrmann (Eds.), Mater. Charact. Using Nondestruct. Eval. NDE Methods, Woodhead Publishing, 2016: pp. 81–124. https://doi.org/10.1016/B978-0-08-100040-3.00004-3.

[62] H. Khan, A.S. Yerramilli, A. D'Oliveira, T.L. Alford, D.C. Boffito, G.S. Patience, Experimental methods in chemical engineering: X-ray diffraction spectroscopy—XRD, Can. J. Chem. Eng. 98 (2020) 1255–1266. https://doi.org/10.1002/cjce.23747.

[63] S.P. Mulvaney, C.D. Keating, Raman Spectroscopy, Anal. Chem. 72 (2000) 145–158. https://doi.org/10.1021/a10000155.

[64] Z. Chen, T.G. Deutsch, H.N. Dinh, K. Domen, K. Emery, A.J. Forman, N. Gaillard, R. Garland, C. Heske, T.F. Jaramillo, A. Kleiman-Shwarsctein, E. Miller, K. Takanabe, J. Turner, UV-Vis Spectroscopy, in: Z. Chen, H.N. Dinh, E. Miller (Eds.), Photoelectrochem. Water Split. Stand. Exp. Methods Protoc., Springer, New York, NY, 2013: pp. 49–62. https://doi.org/10.1007/978-1-4614-8298-7_5.

[65] M.P. Seah, The quantitative analysis of surfaces by XPS: A review, Surf. Interface Anal. 2 (1980) 222–239. https://doi.org/10.1002/sia.740020607.

[66] N. Elgrishi, K.J. Rountree, B.D. McCarthy, E.S. Rountree, T.T. Eisenhart, J.L. Dempsey, A Practical Beginner's Guide to Cyclic Voltammetry, J. Chem. Educ. 95 (2018) 197–206. https://doi.org/10.1021/acs.jchemed.7b00361.

[67] L. Zeng, T. Wu, T. Ye, T. Mo, R. Qiao, G. Feng, Modeling galvanostatic charge–discharge of nanoporous supercapacitors, Nat. Comput. Sci. 1 (2021) 725–731. https://doi.org/10.1038/s43588-021-00153-5.

[68] H.S. Magar, R.Y.A. Hassan, A. Mulchandani, Electrochemical Impedance Spectroscopy (EIS): Principles, Construction, and Biosensing Applications, Sensors 21 (2021) 6578. https://doi.org/10.3390/s21196578.

[69] N. Sharma, H. Ojha, A. Bharadwaj, D. Pal Pathak, R. Kumar Sharma, Preparation and catalytic applications of nanomaterials: a review, RSC Adv. 5 (2015) 53381–53403. https://doi.org/10.1039/C5RA06778B.

[70] J. Chen, J.X. Zhao, Upconversion Nanomaterials: Synthesis, Mechanism, and Applications in Sensing, Sensors 12 (2012) 2414–2435. https://doi.org/10.3390/s120302414.

[71] E. Pomerantseva, F. Bonaccorso, X. Feng, Y. Cui, Y. Gogotsi, Energy storage: The future enabled by nanomaterials, Science 366 (2019) eaan8285. https://doi.org/10.1126/science.aan8285.

[72] Z. Chen, B. Cotterell, W. Wang, E. Guenther, S.-J. Chua, A mechanical assessment of flexible optoelectronic devices, Thin Solid Films 394 (2001) 201–205. https://doi.org/10.1016/S0040-6090(01)01138-5.

[73] B. Sahu, T. Ghosh, S. Kandpal, L. Bansal, C. Rani, H.C. Jha, R. Kumar, Green and Red Luminescent Curcuma and Lawsone Herbal Amalgam as Yellow Emission Source, ChemistrySelect 8 (2023) e202204265. https://doi.org/10.1002/slct.202204265.

[74] C.G. Granqvist, Electrochromic devices, J. Eur. Ceram. Soc. 25 (2005) 2907–2912. https://doi.org/10.1016/j.jeurceramsoc.2005.03.162.

[75] M.-A. De Paoli, G. Casalbore-Miceli, E.M. Girotto, W.A. Gazotti, All polymeric solid state electrochromic devices, Electrochimica Acta 44 (1999) 2983–2991. https://doi.org/10.1016/S0013-4686(99)00013-4.

[76] N. Ahlawat, B. Sahu, L. Bansal, D.K. Rath, S.K. Chondath, R. Kumar, Performance specific recipe for nano-Co3O4 based electrochromic electrodes: Optimizing color modulation parameters, Optik 321 (2025) 172174. https://doi.org/10.1016/j.ijleo.2024.172174.

[77] A. Chaudhary, D.K. Pathak, S. Kandpal, T. Ghosh, M. Tanwar, R. Kumar, Raw hibiscus extract as redox active biomaterial for novel herbal electrochromic device, Sol. Energy Mater. Sol. Cells 215 (2020) 110588. https://doi.org/10.1016/j.solmat.2020.110588.

[78] A. Chaudhary, D. K. Pathak, M. Tanwar, J. Koch, H. Pfnür, R. Kumar, Polythiophene-nanoWO 3 bilayer as an electrochromic infrared filter: a transparent heat shield, J. Mater. Chem. C 8 (2020) 1773–1780. https://doi.org/10.1039/C9TC05523A.

[79] A. Chaudhary, D.K. Pathak, S. Mishra, P. Yogi, P.R. Sagdeo, R. Kumar, Enhancing Viologen's Electrochromism by Incorporating Thiophene: A Step Toward All-Organic Flexible Device, Phys. Status Solidi A 216 (2019) 1800680. https://doi.org/10.1002/pssa.201800680.

[80] B. Sahu, L. Bansal, D.K. Rath, S. Kandpal, T. Ghosh, N. Ahlawat, C. Rani, M.Y. Maximov, R. Kumar, Bendable & twistable oxide-polymer based hybrid electrochromic device: Flexible and multi-wavelength color modulation, Mater. Today Electron. 7 (2024) 100082. https://doi.org/10.1016/j.mtelec.2023.100082.

[81] T.T. Tung, M. Moussa, K.M. Tripathi, T. Kim, M.J. Nine, A.K. Nanjundan, D. Dubal, D. Losic, Coupling graphene microribbons with carbon nanofibers: New carbon hybrids for high-performing lithium and potassium-ion batteries, Sustain. Mater. Technol. 32 (2022) e00393. https://doi.org/10.1016/j.susmat.2022.e00393.

[82] L. Bansal, S. Kandpal, T. Ghosh, C. Rani, B. Sahu, D. Kumar Rath, R. Kumar, Supercapacitive All-Inorganic Nano Metal-Oxides' Complex: A 180o Super-Bendable Asymmetric Energy Storage Device, J. Mater. Chem. C (2023). https://doi.org/10.1039/D3TC02677A.

[83] A. Novinrooz, M. Sharbatdaran, H. Noorkojouri, Structural and optical properties of WO3 electrochromic layers prepared by the sol-gel method, Cent. Eur. J. Phys. 3 (2005) 456–466. https://doi.org/10.2478/BF02475650.

[84] D.D.M. Prabaharan, K. Sadaiyandi, M. Mahendran, S. Sagadevan, Precipitation method and characterization of cobalt oxide nanoparticles, Appl. Phys. A 123 (2017) 264. https://doi.org/10.1007/s00339-017-0786-8.

[85] S. Chen, Y. Xiao, W. Xie, Y. Wang, Z. Hu, W. Zhang, H. Zhao, Facile Strategy for Synthesizing Non-Stoichiometric Monoclinic Structured Tungsten Trioxide (WO3−x) with Plasma Resonance Absorption and Enhanced Photocatalytic Activity, Nanomaterials 8 (2018) 553. https://doi.org/10.3390/nano8070553.

[86] S.K. Tripathy, M. Christy, N.-H. Park, E.-K. Suh, S. Anand, Y.-T. Yu, Hydrothermal synthesis of single-crystalline nanocubes of Co3O4, Mater. Lett. 62 (2008) 1006–1009. https://doi.org/10.1016/j.matlet.2007.07.037.

[87] A. Chaudhary, D.K. Pathak, M. Tanwar, R. Kumar, Tracking Dynamic Doping in a Solid-State Electrochromic Device: Raman Microscopy Validates the Switching Mechanism, Anal. Chem. 92 (2020) 6088–6093. https://doi.org/10.1021/acs.analchem.0c00513.

[88] R. Kumar, R.G. Pillai, N. Pekas, Y. Wu, R.L. McCreery, Spatially Resolved Raman Spectroelectrochemistry of Solid-State Polythiophene/Viologen Memory Devices, J. Am. Chem. Soc. 134 (2012) 14869–14876. https://doi.org/10.1021/ja304458s.

[89] P.J. Morankar, R.U. Amate, A.M. Teli, G.T. Chavan, S.A. Beknalkar, D.S. Dalavi, N.A. Ahir, C.-W. Jeon, Surfactant integrated nanoarchitectonics for controlled morphology and enhanced functionality of tungsten oxide thin films in electrochromic supercapacitors, J. Energy Storage 73 (2023) 109095. https://doi.org/10.1016/j.est.2023.109095.

[90] Z. Bi, X. Li, Y. Chen, X. Xu, S. Zhang, Q. Zhu, Bi-functional flexible electrodes based on tungsten trioxide/zinc oxide nanocomposites for electrochromic and energy storage applications, Electrochimica Acta 227 (2017) 61–68. https://doi.org/10.1016/j.electacta.2017.01.003.

[91] T. Ghosh, S. Kandpal, C. Rani, L. Bansal, M. Tanwar, R. Kumar, Multiwavelength Color Switching from Polyaniline-Viologen Bilayer: Inching toward Versatile All-Organic Flexible Electrochromic Device, Adv. Electron. Mater. 9 (2023) 2201042. https://doi.org/10.1002/aelm.202201042.

[92] Y.-S. Lin, P.-W. Chen, D.-J. Lin, P.-Y. Chuang, T.-H. Tsai, Y.-C. Shiah, Y.-C. Yu, Electrochromic performance of reactive plasma-sputtered NiOx thin films on flexible PET/ITO substrates for flexible electrochromic devices, Surf. Coat. Technol. 205 (2010) S216–S221. https://doi.org/10.1016/j.surfcoat.2010.07.088.

[93] Y.-S. Lin, C.-W. Tsai, P.-W. Chen, Electrochromic properties of V2O5−z thin films sputtered onto flexible PET/ITO substrates, Solid State Ion. 179 (2008) 290–297. https://doi.org/10.1016/j.ssi.2008.01.054.

[94] S.D. Rezaei, S. Shannigrahi, S. Ramakrishna, A review of conventional, advanced, and smart glazing technologies and materials for improving indoor environment, Sol. Energy Mater. Sol. Cells 159 (2017) 26–51. https://doi.org/10.1016/j.solmat.2016.08.026.

[95] L. Dong, C. Xu, Y. Li, Z. Pan, G. Liang, E. Zhou, F. Kang, Q.-H. Yang, Breathable and Wearable Energy Storage Based on Highly Flexible Paper Electrodes, Adv. Mater. 28 (2016) 9313–9319. https://doi.org/10.1002/adma.201602541.

[96] S. Kandpal, T. Ghosh, C. Rani, A. Chaudhary, J. Park, P.S. Lee, R. Kumar, Multifunctional Electrochromic Devices for Energy Applications, ACS Energy Lett. (2023) 1870–1886. https://doi.org/10.1021/acsenergylett.3c00159.

[97] H.-J. Choi, S.-M. Jung, J.-M. Seo, D.W. Chang, L. Dai, J.-B. Baek, Graphene for energy conversion and storage in fuel cells and

supercapacitors, Nano Energy 1 (2012) 534–551. https://doi.org/10.1016/j.nanoen.2012.05.001.

[98] L. Bansal, N. Ahlawat, B. Sahu, D.K. Rath, S.K. Chondath, T. Ghosh, R. Kumar, Nano-Nest Type Porous NiCo2S4@polyindole Core–Shell Array: Efficient Energy Storage Supercapacitor Device, ACS Mater. Lett. (2024) 3736–3744. https://doi.org/10.1021/acsmaterialslett.4c00866.

[99] C. Li, Z. Zhu, Y. Wang, Q. Guo, C. Wang, P. Zhong, Z. Tan, R. Yang, Lead acetate produced from lead-acid battery for efficient perovskite solar cells, Nano Energy 69 (2020) 104380. https://doi.org/10.1016/j.nanoen.2019.104380.

[100] Z. Wu, Z. Lian, S. Yan, J. Li, J. Xu, S. Chen, Z. Tang, S.-P. Wang, K.W. Ng, Extraordinarily Stable Aqueous Electrochromic Battery Based on Li4Ti5O12 and Hybrid Al3+/Zn2+ Electrolyte, ACS Nano 16 (2022) 13199–13210. https://doi.org/10.1021/acsnano.2c06479.

[101] P. Mottier, LED for Lighting Applications, John Wiley & Sons, 2010.

[102] Y. Kim, S.A. Choulis, J. Nelson, D.D.C. Bradley, S. Cook, J.R. Durrant, Device annealing effect in organic solar cells with blends of regioregular poly(3-hexylthiophene) and soluble fullerene, Appl. Phys. Lett. 86 (2005) 063502. https://doi.org/10.1063/1.1861123.

[103] Y. Meng, Y. Zhao, C. Hu, H. Cheng, Y. Hu, Z. Zhang, G. Shi, L. Qu, All-Graphene Core-Sheath Microfibers for All-Solid-State, Stretchable Fibriform Supercapacitors and Wearable Electronic Textiles, Adv. Mater. 25 (2013) 2326–2331. https://doi.org/10.1002/adma.201300132.

[104] A. Chaudhary, D.K. Pathak, S. Mishra, P. Yogi, P.R. Sagdeo, R. Kumar, Enhancing Viologen's Electrochromism by Incorporating Thiophene: A Step Toward All-Organic Flexible Device, Phys. Status Solidi A 216 (2019) 1800680. https://doi.org/10.1002/pssa.201800680.

[105] A.L.-S. Eh, A.W.M. Tan, X. Cheng, S. Magdassi, P.S. Lee, Recent Advances in Flexible Electrochromic Devices: Prerequisites, Challenges, and Prospects, Energy Technol. 6 (2018) 33–45. https://doi.org/10.1002/ente.201700705.

[106] B. Wang, W. Zhang, F. Zhao, W.W. Yu, A.Y. Elezzabi, L. Liu, H. Li, An overview of recent progress in the development of flexible electrochromic devices, Nano Mater. Sci. 5 (2023) 369–391. https://doi.org/10.1016/j.nanoms.2022.08.002.

[107] G. Fu, H. Gong, T. Bai, Q. Zhang, H. Wang, Progress and challenges in wearable electrochromic devices: a review, J. Mater. Sci. Mater. Electron. 34 (2023) 1316. https://doi.org/10.1007/s10854-023-10698-y.

[108] G. Cai, J. Wang, P.S. Lee, Next-Generation Multifunctional Electrochromic Devices, Acc. Chem. Res. 49 (2016) 1469–1476. https://doi.org/10.1021/acs.accounts.6b00183.

[109] D. Dong, S.S. Dhanabalan, P.F.M. Elango, M. Yang, S. Walia, S. Sriram, M. Bhaskaran, Emerging applications of metal-oxide thin films for flexible and stretchable electronic devices, Appl. Phys. Rev. 10 (2023) 031314. https://doi.org/10.1063/5.0151297.

[110] A.S. Agnihotri, A. Varghese, N. M, Transition metal oxides in electrochemical and bio sensing: A state-of-art review, Appl. Surf. Sci. Adv. 4 (2021) 100072. https://doi.org/10.1016/j.apsadv.2021.100072.

[111] S. Kandpal, L. Bansal, A. Ghanghass, T. Ghosh, C. Rani, B. Sahu, D. Kumar Rath, R. Bhatia, I. Sameera, R. Kumar, Bifunctional solid state electrochromic device using WO 3 /WS 2 nanoflakes for charge storage and dual-band color modulation, J. Mater. Chem. C 11 (2023) 12590–12598. https://doi.org/10.1039/D3TC01880F.

[112] S.V.P. Vattikuti, C. Byon, V. Chitturi, Selective hydrothermally synthesis of hexagonal WS2 platelets and their photocatalytic performance under visible light irradiation, Superlattices Microstruct. 94 (2016) 39–50. https://doi.org/10.1016/j.spmi.2016.03.042.

[113] I. Sharma, M.M. Ghangrekar, R.C. Biswal, K. Biswas, Bioelectrogenesis Detection of Inoculums Using Electrochromic Tungsten Oxide and Performance Evaluation in Microbial Fuel Cells, J. Electrochem. Soc. 163 (2015) F183. https://doi.org/10.1149/2.0381603jes.

[114] Y. Li, Z. Tang, J. Zhang, Z. Zhang, Fabrication of vertical orthorhombic/hexagonal tungsten oxide phase junction with high photocatalytic performance, Appl. Catal. B Environ. 207 (2017) 207–217. https://doi.org/10.1016/j.apcatb.2017.02.026.

[115] L. Liang, J. Zhang, Y. Zhou, J. Xie, X. Zhang, M. Guan, B. Pan, Y. Xie, High-performance flexible electrochromic device based on facile semiconductor-to-metal transition realized by WO3·2H2O ultrathin nanosheets, Sci. Rep. 3 (2013) 1936. https://doi.org/10.1038/srep01936.

[116] A.H. Almarri, Enhanced electrochromic properties of anatase TiO2 for flexible electrochromic device, Ionics 28 (2022) 4435–4444. https://doi.org/10.1007/s11581-022-04646-9.

[117] Y. Gogotsi, B. Anasori, The Rise of MXenes, ACS Nano 13 (2019) 8491–8494. https://doi.org/10.1021/acsnano.9b06394.

[118] B. Aïssa, A. Ali, K. Mahmoud, T. Haddad, M. Nedil, Transport properties of a highly conductive 2D Ti3C2Tx MXene/graphene composite, Appl. Phys. Lett. 109 (2016) 43109–32006. https://doi.org/10.1063/1.4960155.

[119] L. Bansal, B. Sahu, D.K. Rath, N. Ahlawat, T. Ghosh, S. Kandpal, R. Kumar, Stoichiometrically Optimized Electrochromic Complex [V2O2+ξ(OH)3-ξ] Based Electrode: Prototype Supercapacitor with

Multicolor Indicator, Small n/a (n.d.) 2312215. https://doi.org/10.1002/smll.202312215.

[120] T.G. Yun, X. Chen, J.Y. Cheong, Research in Electrochromic Supercapacitor – A Focused Review, Batter. Supercaps 6 (2023) e202200454. https://doi.org/10.1002/batt.202200454.

[121] S. Kandpal, T. Ghosh, C. Rani, A. Chaudhary, J. Park, P.S. Lee, R. Kumar, Multifunctional Electrochromic Devices for Energy Applications, ACS Energy Lett. 8 (2023) 1870–1886. https://doi.org/10.1021/acsenergylett.3c00159.

[122] R.U. Amate, P.J. Morankar, G.T. Chavan, A.M. Teli, R.S. Desai, D.S. Dalavi, C.-W. Jeon, Bi-functional electrochromic supercapacitor based on hydrothermal-grown 3D Nb2O5 nanospheres, Electrochimica Acta 459 (2023) 142522. https://doi.org/10.1016/j.electacta.2023.142522.

[123] S.H. Sutar, B.M. Babar, K.B. Pisal, A.I. Inamdar, S.H. Mujawar, Feasibility of nickel oxide as a smart electrochromic supercapacitor device: A review, J. Energy Storage 73 (2023) 109035. https://doi.org/10.1016/j.est.2023.109035.

[124] J. Li, A. Levitt, N. Kurra, K. Juan, N. Noriega, X. Xiao, X. Wang, H. Wang, H.N. Alshareef, Y. Gogotsi, MXene-conducting polymer electrochromic microsupercapacitors, Energy Storage Mater. 20 (2019) 455–461. https://doi.org/10.1016/j.ensm.2019.04.028.

[125] C. Zhao, Q. Wang, H. Zhang, S. Passerini, X. Qian, Two-Dimensional Titanium Carbide/RGO Composite for High-Performance Supercapacitors, ACS Appl. Mater. Interfaces 8 (2016) 15661–15667. https://doi.org/10.1021/acsami.6b04767.

[126] S. Mishra, P. Yogi, A. Chaudhary, D.K. Pathak, S.K. Saxena, A.S. Krylov, P.R. Sagdeo, R. Kumar, Understanding perceived color through gradual spectroscopic variations in electrochromism, Indian J. Phys. 93 (2019) 927–933. https://doi.org/10.1007/s12648-018-1353-7.

[127] X.-Y. Li, Y.-H. Pang, G.-Y. Shi, J.-R. Zhu Jun-Ru, F. Wang, L.-T. Jin, Synthesis and Electrochromic Properties of Poly(3-hexyl-thiophene) in a Room Temperature Ionic Liquid and Its Application to an Electrochromic Device, Chin. J. Chem. 26 (2008) 677–680. https://doi.org/10.1002/cjoc.200890128.

[128] Y. Alesanco, J. Palenzuela, A. Viñuales, G. Cabañero, H.J. Grande, I. Odriozola, Polyvinyl Alcohol–Borax Slime as Promising Polyelectrolyte for High-Performance, Easy-to-Make Electrochromic Devices, ChemElectroChem 2 (2015) 218–223. https://doi.org/10.1002/celc.201402265.

[129] T.-H. Kim, S.-H. Park, D.-H. Kim, Y.-C. Nah, H.-K. Kim, Roll-to-roll sputtered ITO/Ag/ITO multilayers for highly transparent and flexible electrochromic applications, Sol. Energy Mater. Sol. Cells 160 (2017) 203–210. https://doi.org/10.1016/j.solmat.2016.10.033.

[130] B. Sahu, L. Bansal, T. Ghosh, S. Kandpal, D.K. Rath, C. Rani, C. Wesemann, N.C. Bigall, R. Kumar, Metal-Oxide Mixed Polymer Based Hybrid Electrochromic Supercapacitor: Improved Efficiency and Dual Band Switching, J. Phys. Appl. Phys. (2024). https://doi.org/10.1088/1361-6463/ad2dba.
[131] Y. Yang, Y. Song, Y. Qi, B. Fu, F. Li, H. Shi, X. Yu, S. Liu, X. Qu, High-performance electrochromic WO3/POM–MXene energy storage device with color-based energy indication, Surf. Interfaces 49 (2024) 104397. https://doi.org/10.1016/j.surfin.2024.104397.
[132] X. Qu, Z. Liu, L. Zhou, D. Chu, J. Wang, Y. Yang, Porous polyoxotungstate/MXene hybrid films allowing for visualization of the energy storage status in high-performance electrochromic supercapacitors, Dalton Trans. 52 (2023) 5870–5881. https://doi.org/10.1039/D2DT03937K.
[133] Z. Jia, C. Cheng, X. Chen, L. Liu, R. Ding, J. Ye, J. Wang, L. Fu, Y. Cheng, Y. Wu, Applications of all-inorganic perovskites for energy storage, Mater. Adv. 4 (2023) 79–104. https://doi.org/10.1039/D2MA00779G.
[134] M.A. Peña, J.L.G. Fierro, Chemical Structures and Performance of Perovskite Oxides, Chem. Rev. 101 (2001) 1981–2018. https://doi.org/10.1021/cr980129f.
[135] T. Krishnamoorthy, H. Ding, C. Yan, W. Lin Leong, T. Baikie, Z. Zhang, M. Sherburne, S. Li, M. Asta, N. Mathews, S. G. Mhaisalkar, Lead-free germanium iodide perovskite materials for photovoltaic applications, J. Mater. Chem. A 3 (2015) 23829–23832. https://doi.org/10.1039/C5TA05741H.
[136] K. Zhang, N. Zhu, M. Zhang, L. Wang, J. Xing, Opportunities and challenges in perovskite LED commercialization, J. Mater. Chem. C 9 (2021) 3795–3799. https://doi.org/10.1039/D1TC00232E.
[137] M. Shellaiah, K.W. Sun, Review on Sensing Applications of Perovskite Nanomaterials, Chemosensors 8 (2020) 55. https://doi.org/10.3390/chemosensors8030055.
[138] N. Labhasetwar, G. Saravanan, S. Kumar Megarajan, N. Manwar, R. Khobragade, P. Doggali, F. Grasset, Perovskite-type catalytic materials for environmental applications, Sci. Technol. Adv. Mater. 16 (2015) 036002. https://doi.org/10.1088/1468-6996/16/3/036002.
[139] M. Ali Ehsan, R. Naeem, H. Khaledi, M. Sohail, A.H. Saeed, M. Mazhar, Fabrication of CoTiO 3 –TiO 2 composite films from a heterobimetallic single source precursor for electrochemical sensing of dopamine, Dalton Trans. 45 (2016) 10222–10232. https://doi.org/10.1039/C6DT01016D.
[140] D. Cui, Y. Li, Y. Chen, Y. Li, Z. Hai, H. Xu, C. Xue, Synthesis of CoTiO3 nanoparticles with enhanced photocatalytic degradation, Micro Nano Lett. 14 (2019) 840–844. https://doi.org/10.1049/mnl.2018.5025.

[141] R. Balzer, V. Drago, W.H. Schreiner, L.F.D. Probst, Synthesis and structure-activity relationship of a WO3 catalyst for the total oxidation of BTX, J. Braz. Chem. Soc. 25 (2014) 2026–2031. https://doi.org/10.5935/0103-5053.20140187.

[142] X. He, X. Li, Z. Bi, Y. Chen, X. Xu, X. Gao, Dual-functional electrochromic and energy-storage electrodes based on tungsten trioxide nanostructures, J. Solid State Electrochem. 22 (2018) 2579–2586. https://doi.org/10.1007/s10008-018-3959-2.

[143] A. Chaudhary, D.K. Pathak, M. Tanwar, R. Dash, B. Joshi, T. Keerthivasan, S. Kandpal, T. Ghosh, C. Rani, R. Kumar, Hydrothermally grown nano-WO3 electrochromic film: structural and Raman spectroscopic study, Adv. Mater. Process. Technol. 8 (2022) 970–976. https://doi.org/10.1080/2374068X.2020.1835019.

[144] N.C.S. Vieira, E.G.R. Fernandes, A.A.A. de Queiroz, F.E.G. Guimarães, V. Zucolotto, Indium tin oxide synthesized by a low cost route as SEGFET pH sensor, Mater. Res. 16 (2013) 1156–1160. https://doi.org/10.1590/S1516-14392013005000101.

[145] M. Thirumoorthi, J. Thomas Joseph Prakash, Structure, optical and electrical properties of indium tin oxide ultra thin films prepared by jet nebulizer spray pyrolysis technique, J. Asian Ceram. Soc. 4 (2016) 124–132. https://doi.org/10.1016/j.jascer.2016.01.001.

[146] S. Kandpal, T. Ghosh, M. Sharma, D.K. Pathak, M. Tanwar, C. Rani, R. Bhatia, I. Sameera, A. Chaudhary, R. Kumar, Multi-walled carbon nanotubes doping for fast and efficient hybrid solid state electrochromic device, Appl. Phys. Lett. 118 (2021) 153301. https://doi.org/10.1063/5.0046669.

[147] V.K. Kasana, Y. Kumar, P. Singh, S. Dixit, Experimental Studies on Poly(3-Hexylthiophene) Electrode Based Supercapacitors: A Comparison of Electrolytic Species, 4 (2016).

[148] D. Momodu, A. Bello, J. Dangbegnon, F. Barzeger, M. Fabiane, N. Manyala, P3HT:PCBM/nickel-aluminum layered double hydroxide-graphene foam composites for supercapacitor electrodes, J. Solid State Electrochem. 19 (2015) 445–452. https://doi.org/10.1007/s10008-014-2602-0.

[149] J.-L. Xu, Y.-H. Liu, X. Gao, Y. Sun, S. Shen, X. Cai, L. Chen, S.-D. Wang, Embedded Ag Grid Electrodes as Current Collector for Ultraflexible Transparent Solid-State Supercapacitor, ACS Appl. Mater. Interfaces 9 (2017) 27649–27656. https://doi.org/10.1021/acsami.7b06184.

[150] M. Zhu, Y. Huang, Y. Huang, W. Meng, Q. Gong, G. Li, C. Zhi, An electrochromic supercapacitor and its hybrid derivatives: quantifiably determining their electrical energy storage by an optical measurement, J. Mater. Chem. A 3 (2015) 21321–21327. https://doi.org/10.1039/C5TA06237C.

[151] R.T. Ginting, M.M. Ovhal, J.-W. Kang, A novel design of hybrid transparent electrodes for high performance and ultra-flexible bifunctional electrochromic-supercapacitors, Nano Energy 53 (2018) 650–657. https://doi.org/10.1016/j.nanoen.2018.09.016.
[152] H. Moon, H. Lee, J. Kwon, Y.D. Suh, D.K. Kim, I. Ha, J. Yeo, S. Hong, S.H. Ko, Ag/Au/Polypyrrole Core-shell Nanowire Network for Transparent, Stretchable and Flexible Supercapacitor in Wearable Energy Devices, Sci. Rep. 7 (2017) 41981. https://doi.org/10.1038/srep41981.
[153] N. Li, X. Huang, H. Zhang, Z. Shi, C. Wang, Graphene-hollow-cubes with network-faces assembled a 3D micro-structured transparent and free-standing film for high performance supercapacitors, J. Mater. Chem. A 5 (2017) 16803–16811. https://doi.org/10.1039/C7TA03935B.
[154] S. Kiruthika, C. Sow, G.U. Kulkarni, Transparent and Flexible Supercapacitors with Networked Electrodes, Small 13 (2017) 1701906. https://doi.org/10.1002/smll.201701906.
[155] Z. Guo, L. Gao, Z. Xu, S. Teo, C. Zhang, Y. Kamata, S. Hayase, T. Ma, High Electrical Conductivity 2D MXene Serves as Additive of Perovskite for Efficient Solar Cells, Small 14 (2018) 1802738. https://doi.org/10.1002/smll.201802738.
[156] K.-Q. Lu, Y.-H. Li, Z.-R. Tang, Y.-J. Xu, Roles of Graphene Oxide in Heterogeneous Photocatalysis, ACS Mater. Au 1 (2021) 37–54. https://doi.org/10.1021/acsmaterialsau.1c00022.
[157] S. Kandpal, T. Ghosh, C. Rani, M. Tanwar, M. Sharma, S. Rani, D.K. Pathak, R. Bhatia, I. Sameera, J. Jayabalan, R. Kumar, Bifunctional Application of Viologen-MoS2-CNT/Polythiophene Device as Electrochromic Diode and Half-Wave Rectifier, ACS Mater. Au 2 (2022) 293–300. https://doi.org/10.1021/acsmaterialsau.1c00064.
[158] L. Li, D. Zhang, J. Deng, Y. Gou, J. Fang, H. Cui, Y. Zhao, M. Cao, Carbon-based materials for fast charging lithium-ion batteries, Carbon 183 (2021) 721–734. https://doi.org/10.1016/j.carbon.2021.07.053.
[159] S. Panda, K. Deshmukh, S.K. Khadheer Pasha, J. Theerthagiri, S. Manickam, M.Y. Choi, MXene based emerging materials for supercapacitor applications: Recent advances, challenges, and future perspectives, Coord. Chem. Rev. 462 (2022) 214518. https://doi.org/10.1016/j.ccr.2022.214518.
[160] D. Caso, A. Serrano, M. Jaafar, P. Prieto, A. Kamra, C. González-Ruano, F.G. Aliev, Microwave Field-Induced Changes in Raman Modes and Magnetic Force Images of Antiferromagnetic NiO Films, Condens. Matter 9 (2024) 7. https://doi.org/10.3390/condmat9010007.
[161] H.N. Tran, H. Lee, C.B. Park, N.V. Krishna, F.T.A. Wibowo, S.-Y. Jang, J.Y. Kim, S. Cho, Solution-Processable Nickel Oxide Hole

Transport Layer for a Polymer Donor with a Deep HOMO Level, Adv. Mater. Interfaces 9 (2022) 2201274. https://doi.org/10.1002/admi.202201274.

[162] Y. Koshtyal, D. Nazarov, I. Ezhov, I. Mitrofanov, A. Kim, A. Rymyantsev, O. Lyutakov, A. Popovich, M. Maximov, Atomic Layer Deposition of NiO to Produce Active Material for Thin-Film Lithium-Ion Batteries, Coatings 9 (2019) 301. https://doi.org/10.3390/coatings9050301.

[163] S. Kaladi Chondath, L. Bansal, D. Kumar Rath, N. Ahlawat, B. Sahu, S. Tiwari, A. Chaudhary, R. Kumar, Dopant-induced enhanced ion diffusion in flower-shaped hollandite-MnO 2 : a wearable supercapacitor with improved energy storage, Sustain. Energy Fuels 9 (2025) 3304–3314. https://doi.org/10.1039/D5SE00133A.

[164] J. Xue, W. Li, Y. Song, Y. Li, J. Zhao, Visualization electrochromic-supercapacitor device based on porous Co doped NiO films, J. Alloys Compd. 857 (2021) 158087. https://doi.org/10.1016/j.jallcom.2020.158087.

[165] R. Mysoon, M. Ojha, D. Maity, M. Pal, M. Deepa, Switchable electrochromic supercapacitor with vivid colors using a phenolic-viologen paired with an Ag nanowires/NiO film, J. Energy Storage 114 (2025) 115747. https://doi.org/10.1016/j.est.2025.115747.

[166] S.Y. Kim, T.Y. Yun, K.S. Yu, H.C. Moon, Reliable, High-Performance Electrochromic Supercapacitors Based on Metal-Doped Nickel Oxide, ACS Appl. Mater. Interfaces 12 (2020) 51978–51986. https://doi.org/10.1021/acsami.0c15424.

[167] J. Xue, H. Xu, S. Wang, T. Hao, Y. Yang, X. Zhang, Y. Song, Y. Li, J. Zhao, Design and synthesis of 2D rGO/NiO heterostructure composites for high-performance electrochromic energy storage, Appl. Surf. Sci. 565 (2021) 150512. https://doi.org/10.1016/j.apsusc.2021.150512.

Annexures: Copyrights permission

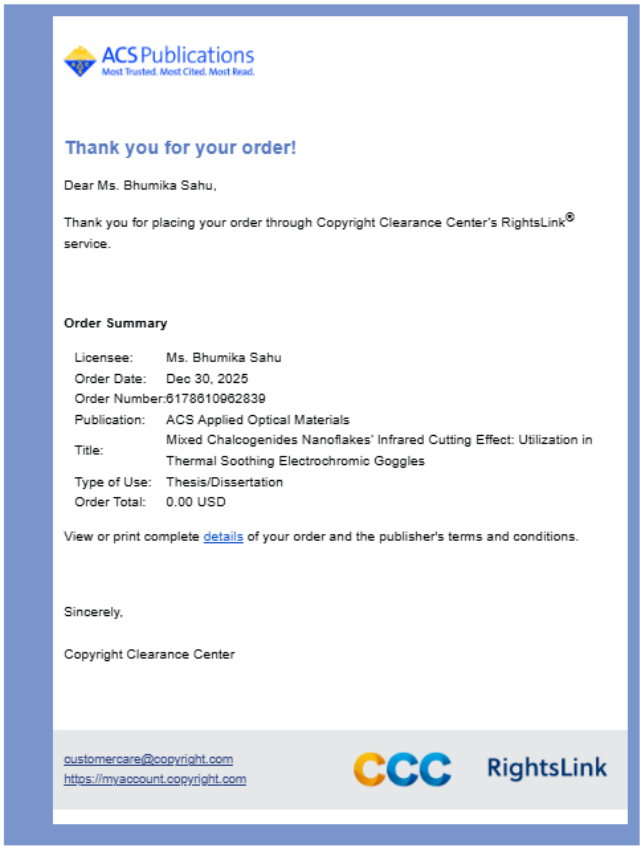

ACS Publications
Most Trusted. Most Cited. Most Read.

Thank you for your order!

Dear Ms. Bhumika Sahu,

Thank you for placing your order through Copyright Clearance Center's RightsLink® service.

Order Summary

Licensee:	Ms. Bhumika Sahu
Order Date:	Dec 30, 2025
Order Number:	6178610962839
Publication:	ACS Applied Optical Materials
Title:	Mixed Chalcogenides Nanoflakes' Infrared Cutting Effect: Utilization in Thermal Soothing Electrochromic Goggles
Type of Use:	Thesis/Dissertation
Order Total:	0.00 USD

View or print complete details of your order and the publisher's terms and conditions.

Sincerely,

Copyright Clearance Center

customercare@copyright.com
https://myaccount.copyright.com

CCC RightsLink